EXPERIMENTAL AND THEORETICAL INVESTIGATION OF CO_2 TRANSCRITICAL POWER CYCLES AND R245fa ORGANIC RANKINE CYCLES FOR LOW GRADE HEAT TO POWER ENERGY CONVERSION

A thesis submitted for the degree of
Doctor of Philosophy

By

Liang Li, M.Sc.

Department of Mechanical, Aerospace and Civil Engineering
College of Engineering, Design and Physical Sciences
Brunel University London

March 2017

ABSTRACT

Globally, there are vast amounts of low-grade heat sources from industrial waste and renewables that can be converted into electricity through advanced thermodynamic power cycles and appropriate working fluids. In this thesis, experimental research was conducted to investigate the performance of a small-scale Organic Rankine Cycle (ORC) system under different operating conditions. The experimental setup consisted of typical ORC system components, such as a turboexpander with a high speed generator, a scroll expander, a finned-tube condenser, an ORC pump, a plate evaporator and a shell and tube evaporator. R245fa was selected as the working fluid, on account of its appropriate thermophysical properties for the ORC system and its low ozone depletion potential (ODP). The test rig was fully instrumented and extensive experiments carried out to examine the influences of several important parameters, including heat source temperature, ORC pump speed, heat sink flow velocity, different evaporators and with or without a recuperator on overall R245fa ORC performances. In addition, in terms of the working fluid's environmental impact, temperature match of the cycle heat processes and system compactness, CO_2 transcritical power cycles (T-CO_2) were deemed more applicable for converting low-grade heat to power. However, the system thermal efficiency of T-CO_2 requires further improvement. Subsequently, a test rig of a small-scale power generation system with T-CO_2 power cycles was developed with essential components connected; these included a plate CO_2 supercritical heater, a CO_2 transcritical turbine, a plate recuperator, an air-cooled finned-tube CO_2 condenser and a CO_2 liquid pump. Various preliminary test results from the system measurements are demonstrated in this thesis. At the end, a theoretical study was conducted to investigate and compare the performance of T-CO_2 and R245fa ORCs using low-grade thermal energy to produce useful shaft or electrical power. The thermodynamic models of both cycles were developed and applied to calculate and compare the cycle thermal and exergy efficiencies at different operating conditions and control strategies.

In this thesis, the main results showed that the thermal efficiency of the tested ORC system could be improved with an increased heat source temperature in the system with or without recuperator. When the heat source temperature increased from 145 ^{o}C to 155 ^{o}C for the system without recuperator, the percentage increase rates of turbine power output and system thermal efficiency were 13.6% and 14% respectively while when the temperature increased from 154 ^{o}C to 166 ^{o}C for the system with recuperator, the percentage increase rates were 31.2% and 61.97% respectively. In addition, the ORC with recuperator required a relative higher heat source temperature, which is comparable to a system without recuperator. On the other hand, at constant heat source temperatures, the working fluid pump speed could be optimised to maximise system thermal efficiency for ORC both with and without recuperator. The pressure ratio is a key factor impacting the efficiencies and power generation of the turbine and scroll expander. Maximum electrical power outputs of 1556.24W and 750W of the scroll expander and turbine were observed at pressure ratio points of 3.3 and 2.57 respectively. For the T-CO_2 system, the main results showing that the CO_2 mass flow rate could be directly controlled by varying the CO_2 liquid pump speeds. The CO_2 pressures at the turbine inlet and outlet and turbine power generation all increased with higher CO_2 mass flow rates. When CO_2 mass flow rate increased from 0.2 kg/s to 0.26kg/s, the maximum percentage increase rates of measured turbine power generation was 116.9%. However, the heat source flow rate was found to have almost negligible impact on system performance. When the thermal oil flow rate increased from 0.364kg/s to 0.463kg/s, the maximum percentage increase rate of measured turbine power generation was only 14.8%. For the thermodynamic analysis, with the same operating conditions and heat transfer assumptions, the thermal and exergy efficiencies of R245fa ORCs are both slightly higher than those of T-CO_2. However, the efficiencies of both cycles can be enhanced by installing a recuperator at under specific operating conditions. The experiment and simulation results can thus inform further design and operation optimisations of both the systems and their components.

PUBLICATIONS

Published Journal Papers

Li, L., Ge, Y. T., Luo, X. and Tassou, S. A. (2016) "Thermodynamic analysis and comparison between CO_2 transcritical power cycles and R245fa organic Rankine cycles for low grade heat to power energy conversion", *Applied Thermal Engineering*, 106, pp. 1290-1299.

Li, L., Ge, Y. T., Luo, X. and Tassou, S. A. (2017) "Experimental investigations into power generation with low grade waste heat and R245fa Organic Rankine cycles (ORCs)", *Applied Thermal Engineering*, 115, pp. 815-824.

Li, L., Ge, Y. T., and Tassou, S. A. (2017) "Experimental study on a 5kW organic Rankine cycle system with R245fa as working fluid for low-grade thermal energy recovery", *Energy Procedia*.

Ge, Y. T., **Li, L.**, Luo, X. and Tassou, S.A. (2017) "Modelling of plate heat exchangers and their associated CO_2 transcritical power generation system". *Energy Procedia*.

Ge, Y. T., **Li, L.**, Luo, X. and Tassou, S.A. (2017) "Evaluation of a Low-grade Power Generation System with CO_2 Transcritical Power Cycles" (Submitted on Applied Energy – under review)

Published Conference Papers

Li, L., Ge, Y. T., Luo, X. and Tassou, S. A. (2015) "Thermodynamic analysis and comparison between CO_2 transcritical power cycles and R245fa organic Rankine cycles for low grade heat to power energy conversion". *Sustainable Thermal Energy Management International Conference (SusTEM2015)*, Newcastle upon Tyne, UK, page 52 – 59.

Li, L., Ge, Y. T., Luo, X. and Tassou, S. A. (2016) "Experimental investigation on power generation with low grade waste heat and R245fa organic Rankine cycles (ORCs)". *International symposium of heat transfer and heat powered cycle*, Nottingham, UK. Paper ID 1264.

Ge, Y. T., **Li, L.**, Luo, X. and Tassou, S.A. (2016) "Performance investigation of a power generation system with CO_2 transcritical Rankine cycles". *Gustav Lorentzen Natural Working Fluids Conference*, Edinburgh, UK.

Li, L., Ge, Y. T. and Tassou, S. A. (2016) "Experimental study on a 5kW organic Rankine cycle system with R245fa as working fluid for low-grade thermal energy recovery". *International Conference on Applied Energy*, Beijing, China. Paper ID 562.

Ge, Y. T., **Li, L.**, Luo, X. and Tassou, S.A. (2016) "Modelling of plate heat exchangers and their associated CO_2 transcritical power generation system". *International Conference on Applied Energy*, Beijing, China. Paper ID 561.

Li, L., Ge, Y. T., Luo, X. and Tassou, S. A. (2017) "Experimental Investigation on Power Generation with Low Grade Waste Heat and CO_2 Transcritical Power Cycle". *1st International Conference on Sustainable Energy and Resource Use in Food Chains, ICSEF 2017*, Berkshire, UK.

Li, L., Ge, Y. T., Luo, X. and Tassou, S. A. (2017) "An experimental investigation on a recuperative Organic Rankine Cycle (ORC) system for electric power generation with low-grade thermal energy". *International Conference on Applied Energy*, Cardiff, UK. (under review)

Li, L., Ge, Y. T., Luo, X. and Tassou, S. A. (2017) "Experimental investigation of organic Rankine cycle (ORC) system with different components". *IV International Seminar on ORC Power Systems, ORC 2017*, Milano, Italy. (under review)

Li, L., Ge, Y. T., Luo, X. and Tassou, S. A. (2017) "Experimental Analysis and Comparison between CO_2 Transcritical Power Cycles and R245fa Organic Rankine Cycles for Low-grade Heat Power Generations". *The 4th Sustainable Thermal Energy Management International Conference, SusTEM2017*, Alkmaar, Netherlands. (under review)

ACKNOWLEDGEMENTS

"Experimental and theoretical investigation of CO_2 transcritical power cycles and R245fa organic Rankine cycles (ORC) for low grade heat to power energy conversion" was a research project carried out in the "RCUK Centre for Sustainable Energy use in Food Chains (CSEF)" under the department of "Institute of Energy Future" at Brunel University London. The project was jointly managed by Dr. Yunting Ge and Prof. Savvas Tassou. This thesis is based on the research work and results of the project.

Firstly, I would like to express my sincere appreciation to my principle supervisor Dr. Yunting Ge for his continuous encouragement and valuable advices which helped me complete this research project successfully. I would also like to express my sincere gratitude to Prof. Savvas Tassou for providing me continuous support since the days of my masters. I would also like to thank Dr. Xiang Luo for his excellent guidance and invaluable assistance in setting up the experimental system.

I am thankful to my colleagues in CSEF, Dr. Baboo Lesh Gowreesunker, Konstantinos Tsamos, Dr. Jining Sun and Dr. IDewa Santosa, Miss Ashika Rai, and the technicians, Mr. Costas Xanthos and Mr. John Fosbery, for their valuable assistance throughout my Ph.D. career. In addition, I would also like to thank Mr. Lawrence Pagett, a lecturer at Wolverhampton University, for his support in helping me learn all aspects of British life since the beginning of my stay in the UK.

Finally, I would like to express a very special gratitude to my Father, Mother, Shuo Liu for their fortitude and patience during the most arduous period of my life. I would like to dedicate my thesis to them.

TABLE OF CONTENTS

LIST OF FIGURES

LIST OF TABLES

NOMENCLATURES

C_p	Specific heat capacity (kJ/kg K)
E	Exergy rate (W)
h	Enthalpy (J/kg)
I	Exergy destruction rate (W)
$\dot{m}$	Mass flow rate (kg/s)
n	Rotation speed (RPM)
P	Pressure (Pa or bar)
PR	Pressure ratio
$\dot{Q}$	Heat transfer rate (W)
q	Specific heat transfer rate (J/kg)
R	Rotation speed (RPM)
S,s	Entropy (J/kg K)
T	Temperature (^{o}C or K)
$\bar{T}$	Average temperature (K)
V	Velocity (m/s); volume (l)
$\dot{V}$	Volume-flow rate (l/s)
$\dot{W}$	Work input/ output (W)

Greek Symbols

η	Efficiency (-)
ρ	Density (kg/m^3)
κ	Thermal conductivity (W/m K)
μ	Kinematic viscosity (mm^2/s); temperature transfer efficiency (-)
Δ	Difference
ϕ	Filling factor (-)
υ	Specific volume (m^3/kg)
φ	Build-in volume ratio (-)
ε	Heat transfer effectiveness (-)

Subscripts

a	air
all	overall
b	Boiling point
c	Critical point
cd	condenser
CO_2	Carbon dioxide
e	electrical
el	electrical
ex	expander
exp	expander
eva	evaporator
evp	evaporator
f	fluid
gg	Gas generator
id	idea
in	inlet
is	Isentropic
m	mechanical
max	Maximum
min	minimum
net	net
oil	Thermal oil
out	outlet
P	Pump
pmp	pump
pinch	Pinch point
rec	recuperator
s	System; heat source
source	Heat source
sh	superheat

sink	Heat sink
su	supply
swept	swept
T	Turbine
th	thermal
tot	total
wf	Working fluid
0	Dead state
1,2,3…	System location points

ABBREVIATIONS AND GLOSSARY

ASHRAE	American society of heating refrigerating and air-conditioning engineers
CHP	Combined heat and power
CO_2	Carbon dioxide
CP grade	Chemically pure
CSEF	Centre for Sustainability Energy use in Food chains - Brunel University London
EES	Engineering equation solver
GHGs	Green-house gases
GWP	Global Warming Potential
HFC	Hydro-fluoro-carbon
HX	Heat exchanger
IR	Infrared
LEL	Lower explosive limit
MTG	Microturbine power generator
NI	National Instruments
ODP	Ozone depletion potential
OEL	Occupational exposure limit
ORC	Organic Rankine cycle
RCUK	Research Council United Kingdom
RPM	Revolutions per minute
S-CO_2	Supercritical Brayton cycle
T-CO_2	CO_2 transcritical power cycles

Chapter 1 – INTRODUCTION

The extensive usage of fossil fuels in power generation worldwide has further escalated the global warming effects and concerns on imminent energy crisis. One of the challenges of the 21st century is to tackle the risks arising from excessive CO_2 emissions by replacing fossil fuels with recovered waste heat and renewable energy. Waste heat sources can be divided into three main categories according to their temperature range: high temperature (>650 ^{o}C), medium temperature (230 ^{o}C~650 ^{o}C) and low temperature (<230 ^{o}C) (Tchanche et al., 2011). Statistics have shown that more than 50% of industrial waste heat and renewables are within the low-grade range (Hung et al., 1997), including heat from manufacturing and process industries, solar energy, geothermal energy and internal combustion engine exhausts and coolants in commercial, institutional or automotive applications. Recovering the abundant amount of low-grade waste heat using advanced thermodynamic power cycles and appropriate working fluids for power generation could help resolve a part of the energy crisis and reduce any further environmental impacts (Lecompte et al., 2015; Yamamoto et al., 2001).

1.1 Heat Recovery Opportunities in UK

The industrial sector was responsible for 16.2% of the UK's final energy consumption in 2015, as shown in Fig. 1.1. Among the energy sources, petroleum accounted for 47.5% and electricity accounted for 18% (both from direct and indirect use) (Decc, 2016). The increasing consumption of fossil fuels has escalated the amount of harmful greenhouse gases (GHGs) in the atmosphere. The growing environmental concern as a result has led the government to set a new target of reducing the GHGs emission level by at least 80% from 1990 levels by 2050 (HM Government, 2008). The UK Government's Department for Business, Energy and Industrial Strategy has estimated that the food, beverages and tobacco industries accounted for approximately 12% of the energy consumption by the industrial sector (Decc, 2016), as shown in Fig. 1.2.

Heat is one of the important energy sources for these industries. There is an abundant amount of waste heat energy at the end of all heating processes. Several new

technologies have been developed with an aim to recover and utilize these waste heat energy again. Some examples of these technologies include: absorption chillers, used for providing cooling using waste heat as the energy source, heat pump system, used for increasing the heat energy to a higher temperature, Rankine cycles, used for converting the waste heat energy to electrical energy, and many more technologies currently undergoing further research. Among the new technologies which can recover waste heat energy in form of electrical energy at a low temperature range, Rankine cycle has recently appeared as the most promising one (Hammond et al, 2014).

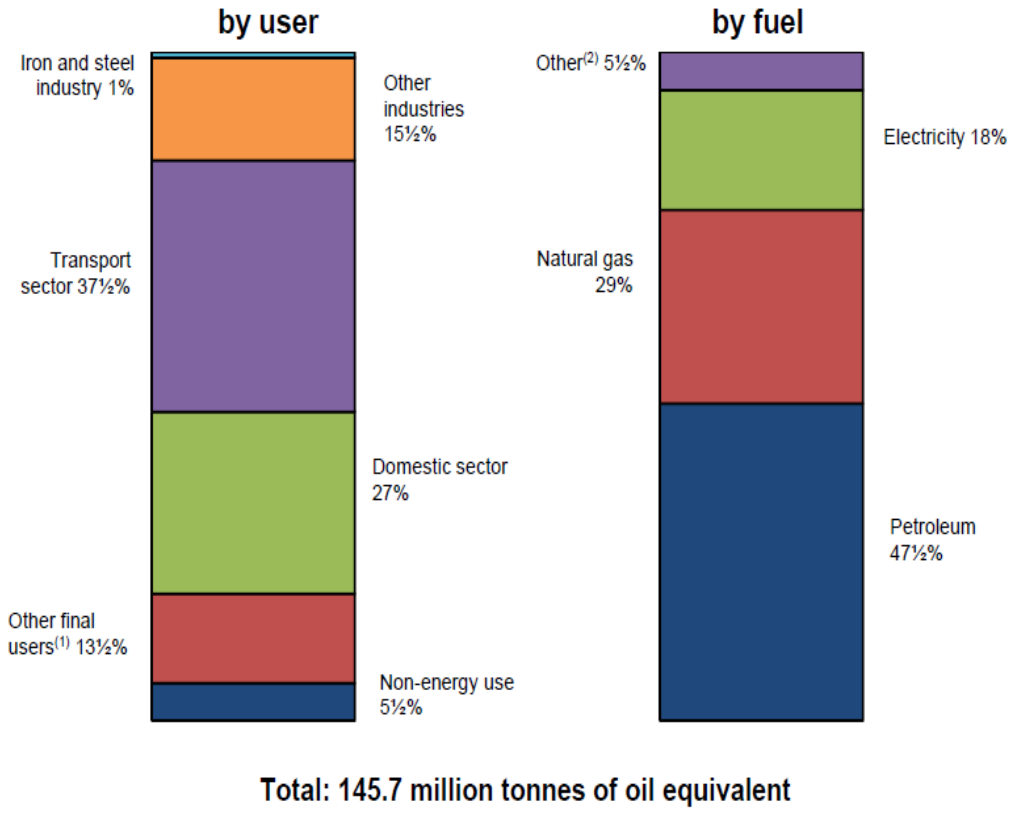

Figure 1.1 Final fuel consumption in UK 2015 (Decc, 2016)

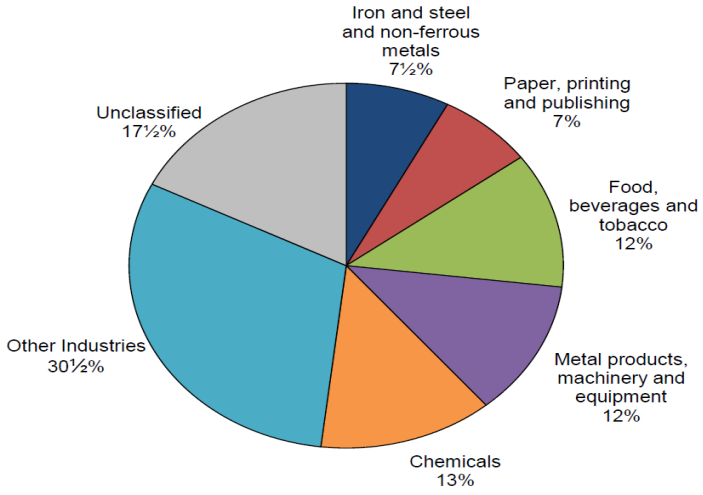

Figure 1.2 Energy consumption by main industrial groups 2015 (Decc, 2016)

1.2 Organic Rankine Cycle Systems

For a low-grade heat energy conversion system, the conventional steam Rankine cycle cannot achieve both high thermal efficiency and compact system size; thus, it is not an appropriate economic option (Badr et al., 1985; Yamamoto et al., 2001; Chen et al., 2006). This is because a low-grade heat source cannot produce enough steam at high temperatures and pressures required by the steam turbine.

In contrast to the conventional system, an Organic Rankine Cycle (ORC) is a more feasible option for the application of low-grade heat sources in terms of operating parameters, system size and thermal and exergy efficiencies. The working principle of the ORC is similar to Clausius-Rankine steam power plant. However, the system uses an organic working fluid such as R245fa instead, which is able to condense at a lower pressure and evaporate at a higher pressure.

The most challenging aspects of a low-grade energy conversation system design are to select an appropriate working fluid and a highly efficient organic Rankine cycle. Study by Saleh at al. (Saleh et al., 2007) analysed both subcritical and supercritical ORCs with thirty-one different pure working fluids at a fixed working fluid temperature range. The thermal efficiencies ranged between 0.36% and 13%, indicating the importance of thermodynamic cycles and working fluid selections. It was also found that supercritical working fluids can receive a greater heat transfer from sensible heat sources such as

waste heat compared to those of subcritical ones when considering matchable cold and hot side temperature glides in the heat exchanger. Consequently, at the same operating conditions, the working fluid temperature at the turbine inlet will be relatively higher for the supercritical heat addition process and thus will result in higher cycle thermal efficiency.

A recuperator can be integrated into an ORC system, but may or may not enhance the system thermal efficiency, depending on the working fluid, the applicable fluid state at the expander outlet and the application. An ORC working fluid can be classified as dry, wet or isentropic, based on the slope of its saturated vapour curve (Chen, 2010). For a dry working fluid such as R245fa, the fluid at the ORC turbine outlet is superheated and its temperature is high enough to heat up the liquid fluid from the ORC pump, thereby boosting system performance when the recuperator is installed.

Such circumstances may change when the ORC is used in different heat recovery systems. In an application of solar ORC using R245fa as a working fluid, an experimental rig was developed in which a solar collector acted as the ORC evaporator (Wang et al., 2012). The introduction of a recuperator into the system increased the temperature at the collector inlet and thus led to a reduced collector performance and system thermal efficiency.

In addition, an ORC thermal efficiency can be affected by the performance of system components, particularly the expander. Kang (Kang, 2012) estimated an R245fa ORC system to have nominal power generation of 30kW using a radio turbine as an expander. The maximum average turbine and overall thermal efficiencies were found to be 78.7% and 5.22% respectively when the expander pressure ratio was fixed. The overall thermal efficiency could be further improved with enhanced turbine efficiency.

1.3 CO_2 Transcritical Power Cycle Systems

Currently, R245fa is widely used as the working fluid in ORCs due to its thermophysical properties and its zero Ozone Depletion Potential (ODP). However, R245fa is still classified as HFC with relatively high Global Warming Potential (GWP),

which will undoubtedly affect its future application in ORCs. This has led the industry to look at new alternatives of working fluids with low GWP.

On the other hand, as a natural working fluid, CO_2 has been widely accepted as an alternative working fluid in refrigeration systems (Ge et al., 2011) and heat pump systems (Jiang et al., 2013) due to its zero ODP and almost negligible GWP. The thermophysical properties of the fluid also make it suitable for use in these systems with an exception of its high critical pressure and low critical temperature.

The high operating pressures of a CO_2 energy system requires special designs for system components and controls, while the low critical temperature will turn a CO_2 low-grade power generation system into a transcritical Rankine (T-CO_2) or supercritical Brayton cycle (S-CO_2). To prevent high operating pressures, instead of using a pure CO_2 working fluid, a zeotropic mixture of CO_2 and another fluid such as R1234yf or R1234ze could be used in the low-grade power generation although further efficiency improvement would be needed (Dai, et al, 2014). Kim et al. (Kim et al., 2012) conducted a comparison between T-CO_2 and S-CO_2 cycles in terms of energy and exergy analyses. They found that the T-CO_2 is better equipped for low-grade heat sources due to the thermal match in heat transfer process of high pressure side. Furthermore, Vélez et al. (Vélez et al., 2012) conducted a theoretical analysis of low-grade power generation with T-CO_2. Simulation results showed that exergy and energy efficiencies could increase up to 25% and 300% respectively when the turbine inlet temperature increased from 60 to 150 ^{o}C at different expander inlet pressures. Similar T-CO_2 low temperature power cycles for different applications have also been carried out by various researchers (Chen et al., 2011; Zhang et al., 2007).

It is recognized that CO_2 is a promising working fluid to be applied into a low-grade power generation system with T-CO_2 cycles. However, the experimental and theoretical analysis, and performance comparison between the T-CO_2 and conventional R245fa ORC systems at their applicable operating conditions need to be further investigated, which has not been thoroughly implemented so far.

1.4 Research Aim and Objectives

The present PhD research is an integral part of a bigger externally funded research project which an aim to provide experimental and theoretical investigation of a small-scale CO_2 transcritical power cycles (T-CO_2) and organic Rankine cycles (ORC) for low grade heat to power energy conversion. The specific objectives of the overall project are:

- Conduct literature review on the designs and performances of T-CO_2 and ORC systems and their components for low grade heat recovery.
- To design, construct and evaluate the R245fa ORC system with different components and expansion machines.
- To design, construct and evaluate the first-of-its-kind, the T-CO_2 system with turboexpander.
- To thermodynamically model the proposed the R245fa ORC system and the T-CO_2 system.

The specific tasks of the present PhD research are:

- To experimentally evaluate the performances of the R245fa ORC system and different system components at different conditions.
- To experimentally evaluate the performances of the T-CO_2 system at different conditions.
- To thermodynamically model the performances differences between R245fa ORC system and T-CO_2 system at the different conditions.

1.5 Structure of the Thesis

The thesis consists of nine chapters in total. The following highlights a brief description of the contents in each chapter;

Chapter 1 provides an overview of the research work, the main aim and objectives, and the general structure of the thesis.

Chapter 2 presents an overview of organic Rankine cycle (ORC) and transcritical power cycle systems. The chapter also provides an overview of different components used into both the systems.

Chapter 3 overviews the heat source system used in R245fa ORC system and T-CO_2 system. The chapter also explores and provides a detailed discussion on the design and construction of ORC test rig which incorporates various mechanical, electrical, control and monitoring systems.

Chapter 4 presents the test results from experiments conducted on the R245fa ORC system with turboexpander and plate-type evaporator. In addition, the effects of recuperator installation, heat source temperatures and R245fa liquid pump speeds and condenser fan speeds on the turboexpander efficiency and system performance have been evaluated in this chapter.

Chapter 5 presents the test results from experiments conducted on the R245fa ORC system with scroll expander and different kind evaporators. The performances of scroll expander and evaporators haven been thoroughly analysed.

Chapter 6 provides the details of the laboratory testing facilities of the T-CO_2 system and its main components with control and data logging systems.

Chapter 7 presents the experimental results from the T-CO_2 system with CO_2 turboexpander and plate-type gas generator. The chapter mainly discusses the effect of heat source flow rate and CO_2 liquid pump speeds on the performances of system and components.

Chapter 8 presents the details of thermodynamic modelling of the proposed R245fa ORC system and T-CO_2 system. The modelling results for both systems have been discussed.

Chapter 9 provides the final conclusion of this study and identifies areas for further investigation and recommendations.

Chapter 2 – LITERATURE REVIEW

As discussed in the Chapter 1, the current global power generation is predominantly from the combustion of fossil fuels, which is responsible for a number of environmental impacts such as air pollution, excess CO_2 emissions, and energy resource depletion. This has led the industry to explore several new alternatives of power sources. Among the alternatives, power generation using low-grade heat sources such as solar thermal (Manolakos et al., 2007), biomass (Uris et al., 2014; Qiu et al., 2012), geothermal (Heberle et al., 2010) and industrial waste heat (Hajabdollahi et al., 2013) have appeared as promising options.

2.1 Organic Rankine Cycle

The working principle of an ORC is similar to a Clausius-Rankine steam power plant. However, an ORC system uses an organic working fluid such as R245fa, which is able to condense at a lower pressure and evaporate at a higher pressure. The design of small capacity power systems is capable of recovering a large temperature range of heat sources. Study by Badr et al. states that for low-grade heat sources, an ORC has higher power generation efficiency and is economically viable than that a steam Rankine cycle (Badr et al., 1985). Fig. 2.1 (a) illustrates a schematic layout of an ORC system while Fig. 2.1 (b) presents the T-s diagram of the system. The main components of an ORC system comprises of an expander machine, a condenser, a liquid pump and an evaporator.

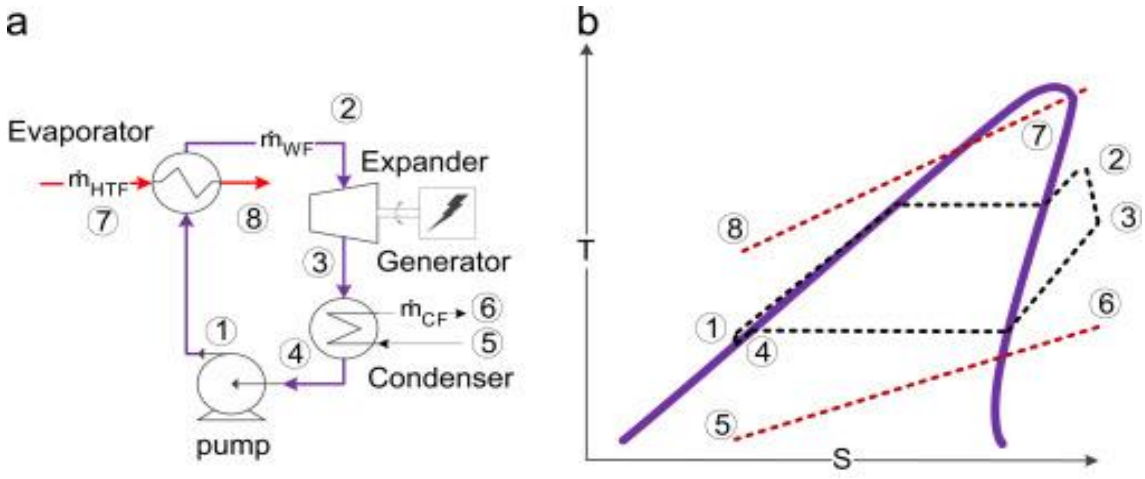

Figure 2.1 (a) Schematic layout of an ORC system. (b) ORC T-s diagram (Lecompte et al., 2015)

2.1.1 Working fluids for ORC system

Many studies have explored the use of different working fluids in an ORC system based on their thermophysical properties, environmental impact, cost considerations and safety issues etc (Bao et al., 2013; Badr et al., 1985; Saleh et al., 2007; Chen et al., 2010).

Nevertheless, there is no working fluid that can meet all the above requirements. Therefore, various named methods such as the bucket effect and spinal point were used to balance the impact and optimise selection (Qiu, 2012). Subsequently, eight organic working fluids including HFE7000, HFE7100, PF5050, R123, n-pentane, R245fa, R134a and isobutene, which have been mostly applied and investigated in the past decade, were chosen to evaluate, compare and finally be ranked. Moreover, the author acknowledged that the selection of an accurate ORC working fluid must be driven by a specific heat source (Wang et al., 2012). For instance, R134a was believed to be the most suitable working fluid for small-scale solar ORC applications (Tchanche et al., 2009). In applications of geothermal electricity with ORC systems, R123 or n-pentane might be the best choice for the working fluid (Madhawa et al., 2007). In addition, for application of waste heat recovery of low to medium temperature heat in industry, R245fa was found to be most appropriate one (Quoilin, 2013).

Saleh et al. compared theoretically the system performance of ORCs with thirty-one pure working fluids. The thermal efficiencies of the ORCs were calculated with range

between 0.36% and 13%, while R245fa ORC could present approximately 12.52% efficiency (Saleh et al., 2007). Other than the system's thermal efficiency, several other characteristics should also be considered when selecting an appropriate organic working fluid for use in thermodynamic power cycle. This includes, the fluid's global warming potential (GWP), ozone depletion potential (ODP), safety issues such as flammability and toxicity etc.

An ORC working fluid can be classified as dry, isentropic or wet depending on the entropy change with temperature along its saturated vapor line on a T-s diagram (dT/ds) (Liu et al., 2004): the dry working fluid with a positive slopes, the isentropic working fluid with almost vertical slopes and the wet working fluid with a negative slopes. The examples of dry fluid for pentane, isentropic fluid for R11 and wet fluid for water are shown in Fig.2.2. In many commercial ORC systems, dry working fluids are preferred since the working fluid state after expansion will be mostly at superheat, and the expansion process of the turbine occurs fully in the superheated vapor region. There is near vertical vapor saturation curve for the isentropic working fluid. However, for the wet working fluid, a super heater is needed to superheat to wet working fluid to the vapor (Bal et al., 2013).

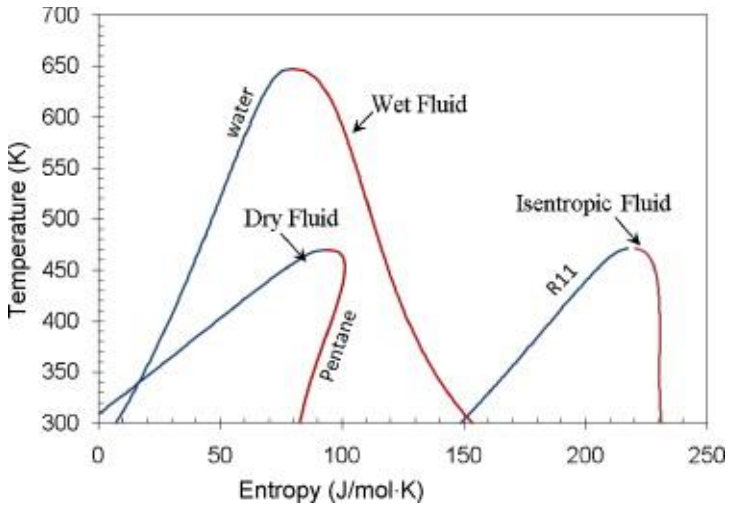

Figure 2.2 Three types of working fluids: dry, isentropic, and wet (Chen et al., 2010)

On the other hand, since these ORC working fluids are all pure substances and operate under subcritical cycles, the mismatch in temperatures between the hot and cold side fluids in the high-pressure side heat exchanger will increase the irreversible loss and

affect system's efficiency. In such circumstances, using zeotropic mixtures such as R245fa/ R152a as ORC working fluids could be more feasible options (Le et al., 2014; Li et al., 2014).

2.1.2 Expansion machines

In an ORC system, the expander is an important component and its performance can determine overall system thermal efficiency. Similar to compressors in refrigeration systems, the ORC expanders can also be classified into two types: positive displacement such as scroll, vane and screw, and speed ones that includes a turboexpander or turbine. In the application of a micro-CHP system with integrated biomass boiler and HFE 7000 ORC, a vane type of expander was employed for experimental investigation (Qiu, et al., 2012). In this system, the biomass boiler heated pressurised water flow to around 125 ^{o}C and then indirectly evaporated and superheated the ORC fluid. However, the system power generation and thermal efficiency were 0.861kW$_e$ and 1.41% respectively, both relatively low but can be potentially improved by better expander and ORC evaporator design etc. For a given heat source temperature of 105 ^{o}C, experiments and simulation on an R245fa ORC with scroll expanders of different displacements were carried out with a maximum system thermal efficiency of 3.2% (Gao et al., 2015).

The effect of displacement values on the expander and system efficiencies may be different. A R123 ORC test rig with a screw expander was set up to investigate the effect of various inlet vapour dryness on the expander efficiency (Xia et al., 2015). The test results demonstrated that the increased inlet vapour dryness could enhance the expander power output but would reduce both the expander volumetric and overall efficiencies. Compared to the scroll and screw expanders in an ORC system, a turboexpander or turbine has a number of advantages in terms of manufacturability, unit weight, stability and efficiency (Pu et al., 2016). It was reported that when a turboexpander or turbine was used as an expander in an R123 ORC system, the expander isentropic and system thermal efficiencies could be improved compared to its scroll or screw counterparts (Pei et al., 2011). The turboexpander was deemed suitable for a small-scale ORC system application.

2.1.3 Condensers

A significance of the low recovery efficiency of thermal energy into electric power is that most of the heat, which is added to the ORC systems, has to be dumped into the

ambient. The condenser is therefore very important in ORC system powered by low grade heat sources. The whole capital investment of a heat exchanger accounts for 40% - 90% of the total investment cost of ORC system. Among the heat exchangers, the condenser holds the largest percentage of investment cost in low grade heat source-driven ORC system (Papadopoulos et al., 2010; Quoilin et al., 2011).

Both air-cooled (Gabbrielli, 2012; Ghasemi, 2013) and water-cooled (Karellas et al., 2012; Pierobon et al., 2013) condensers are commonly utilised in ORC systems to release heat from the systems to heat sinks. The comparison between air-cooled and water-cooled condensers has already been studied in the previous researches. A model of a cogeneration power plant powered by burning waste, while the condenser consists of both air-cooled and waster cooled, has been developed by Barigozzi (Barigozzi et al., 2011). The research results show that when the ambient temperature is less than 15 ^{o}C, it is best to choose the air-cooled condenser. When the ambient temperature is higher than 15 ^{o}C, both the air-cooled and water-cooled condensers are used. The air-cooled condenser is used to cool down the steam at the beginning and the water-cooled condenser is used to cool the steam further down after. The research results are mainly valid for high temperature heat sources, which will lead the inlet temperature of the turbine to be around 450 ^{o}C. The water-cooled condenser is relatively compact and highly efficient but usually needs to have an extra cooling mechanism to cool down the warm water. In addition, other disadvantages of using a water-cooled condenser include the need of water for daily consumption and its availability in places where water is scarce (Walraven et al., 2015).

The air-cooled condenser is normally a finned-tube with enhanced flexibility but in a large size, and therefore needs to be designed optimally for both hydraulic and heat transfer behaviours (Ge et al., 2009). In addition, vapor quality and mass flux are two important parameters that influence the tube condensation heat transfer and pressure drop in the condensation process (Luo et al., 2016). The effect of vapor quality on the condensation heat transfer of R134a in a smooth cooper tube has been investigated by Berrada (Berrada et al., 1996). The research results show that the condensation heat transfer coefficients of a vapor quality of 0.8 are almost double than those of a vapor quality of 0.3. In addition, the pressure drop increases with a higher vapor quality and mass flux, and the condensation heat transfer coefficients of R134a increase linearly

with vapor quality (Wongwises, et al., 2006; Laohalertdecha et al., 2010). Therefore, most of researches only focus on the pressure drop and heat balance behaviours of the air-cooled condenser. A higher heat exchanger coefficient causes a smaller size of the condenser. In addition, a lower pressure drop of the condenser causes a lower power generation of the expander and higher ORC pump power consumption. Improvement in the design and optimisation of air-cooled condenser could further increase the efficiency rate and decrease the construction cost of the ORC systems.

2.1.4 Recuperator

A recuperator is normally installed in an ORC system to save thermal energy from the heat source and thus increasing the thermal efficiency of the cycle (Colonna et al., 2015), as schematically shown in Fig 2.3.

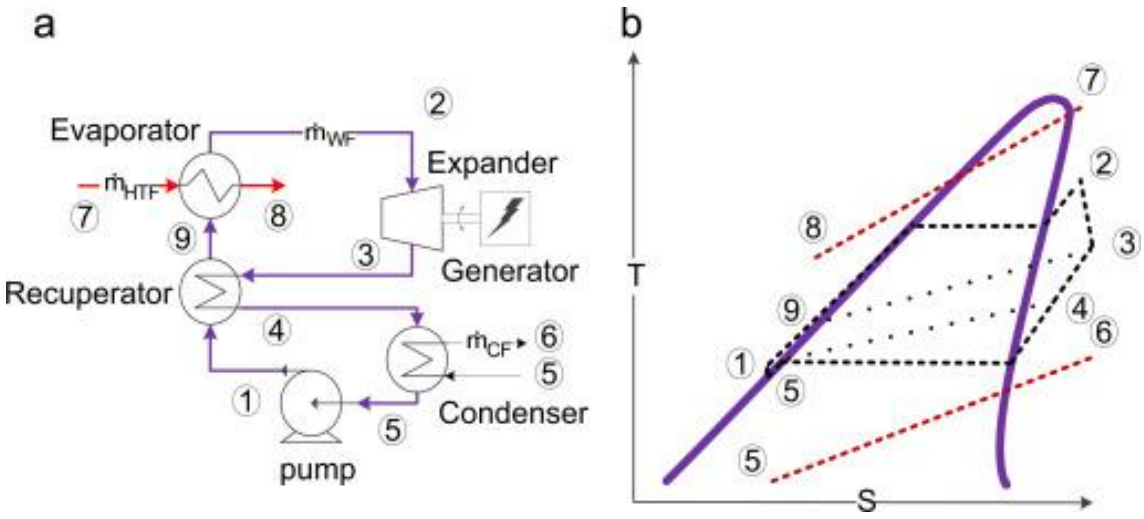

Figure 2.3 (a) ORC with recuperator cycle layout. (b) ORC with recuperator T-s diagram (Lecompte et al., 2015)

However, when a low-grade heat source is applied, the feasibility of recuperator integration in an ORC system is dependent on a number of issues including types of working fluids, applications and operating conditions. The applicable ORC working fluids can be classified as wet, isentropic or dry based on respective shapes of saturated vapour (Saleh et al., 2007). For these ORC working fluids, different degrees of superheating are required if a recuperator is integrated in each ORC system. This will ensure some significant degrees of superheating at expander outlet so as to preheat liquid working fluid from pump outlet. These can be demonstrated by some previous research outcomes. When the superheats at evaporator were properly maintained and

dry working fluids were applied, the ORC system thermal efficiencies could be greatly improved (Meinel et al., 2014; Mago et al., 2008). Otherwise, even the use of dry ORC working fluid such as R236ea, the installation of a recuperator in the system could not improve the system performance under a given waste heat source condition (Dai et al., 2009).

On the other hand, as a different application, an experimental investigation was carried out on a low-temperature solar recuperative Rankine cycle system using working fluid R245fa and a flat plate collector was used as an evaporator to gather solar thermal energy (Wang et al., 2012). The test results demonstrated that using a recuperator in the ORC system could not increase the system thermal efficiency. This was because the preheating by the expander exhaust through the recuperator lowered the solar collector efficiency and thus the overall system thermal efficiency. Another disadvantage of recuperator integration in an ORC system is the pressure increase at the expander outlet due to fluid pressure drop through the heat exchanger, which would affect the expander efficiency negatively. The pressure drop through the recuperator however is subject to the working fluid flow rate and therefore ORC pump speed and system operating states which need to be further investigated experimentally.

2.2 Transcritical Power cycle

As mentioned previously, Organic Rankine Cycles (ORC) are a known feasible option for the application of low-grade heat sources in terms of operating parameters, system sizes, thermal and exergy efficiencies. However, one important limitation of an ORC is its constant evaporation temperature, which increases irreversibly during the heat addition process when using sensible heat sources such as waste heat (Chen et al., 2010). In addition, HFC working fluids is conventionally employed in an ORC, which has zero Ozone Depletion Potential (ODP) but a relatively high Global Warming Potential (GWP). This will affect the future application of ORCs in low-grade waste heat recovery.

On the other hand, as a natural working fluid, CO_2 has been widely applied in refrigeration (Ge et al., 2011) and heat pump (Jiang et al., 2013) systems due to its zero ODP, negligible GWP and superb thermophysical properties, despite its high critical

pressure and low critical temperature. The high operating pressures of a CO_2 energy system require special designs for system components and controls, while the low critical temperature will turn a CO_2 low-grade power generation system into a transcritical Rankine cycle (T-CO_2) or even a supercritical CO_2 Brayton cycle. The example of a transcritical power cycle system is shown in Fig. 2.4. The cycle layout of transcritical power system (Fig. 2.4 (a)) is same as the basic ORC system, as shown in Fig. 2.1. The T-s diagram of transcritical power system is shown in Fig. 2.4 (b).

Of these CO_2 power cycles, the T-CO_2 is most effective in harvesting low-grade heat sources when a low temperature heat sink is accessible (Chen et al., 2006; Kim et al., 2012). The supercritical heat-addition process of a T-CO_2 can produce high-efficiency temperature matching between the sensible heat source and the working fluid, leading to no pinch limitations. In addition, the superb thermophysical properties of CO_2 can create a more compact T-CO_2 system than those of ORCs. Therefore, the T-CO_2 has considerable potential for low-grade power generation. Nevertheless, the performance of such a system requires thorough investigation to understand system operational mechanisms for optimising system efficiency.

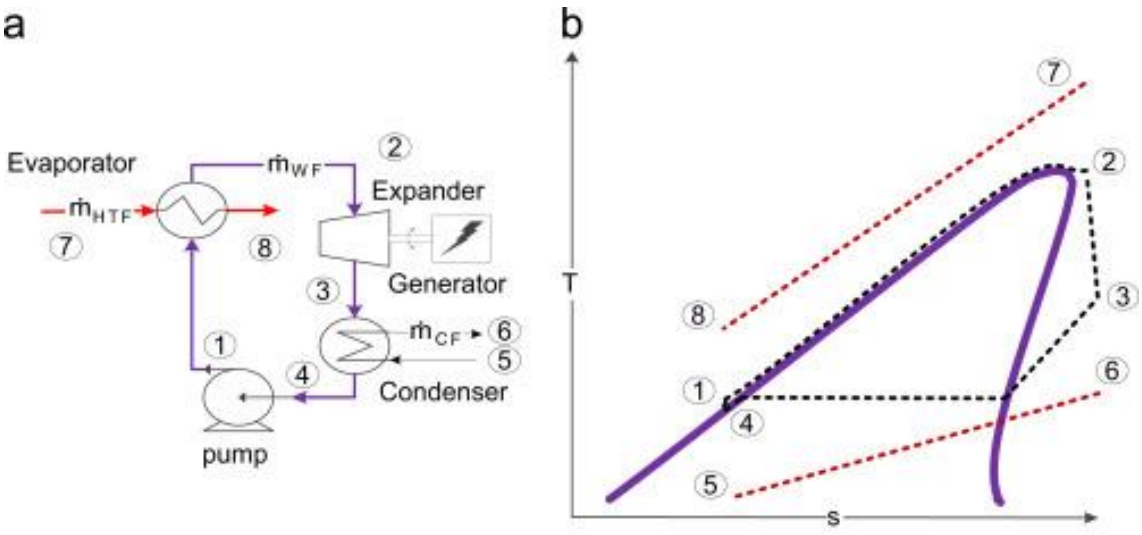

Figure 2.4 (a) Transcritical power cycle layout. (b) Transcritical power cycle T-s diagram (Lecompte et al., 2015)

2.2.1 Components for transcritical power cycle

Due to the high critical pressures of CO_2, the pressure of heating processes in CO_2 transcritical power cycles could also be high (typically above 90bar), such that

conventional heat exchangers, gas turbines or expanders and power cycles cannot be directly applied. Consequently, until now, investigations on low temperature heat source energy conversion systems with CO_2 transcritical power cycles have been limited to small-scale laboratory work and theoretical analyses.

A solar powered test rig with a CO_2 transcritical power cycle was set up to examine system performance at designated operating states (Zhang et al., 2007). This test rig used a throttling valve to simulate the expansion device such that power generation could not be measured directly. A highly promising solution to the CO_2 turbine market problem is to use a CO_2 scroll expander for the test rig or practical installation. The expander works as the corresponding compressor in reverse, which is a positive displacement machine. CO_2 scroll expanders and compressors have already been implemented in refrigeration and air conditioning (Ge et al., 2011); however, its application in transcritical power cycles needs to be explored as it plays an important role in the power system. A steady-state thermodynamic model for the above solar-CO_2 power system showed that the power and heat outputs and efficiencies varied remarkably in different seasons of the year, due to the periodical change of solar radiation (Zhang et al., 2006). Therefore, a transient mathematical model would be more suitable in simulating the real performance of the solar system. In the application of waste heat with a maximum heat source temperature of 150 ^{o}C, the performance of a CO_2 transcritical power cycle with optimised supercritical pressure was compared thermodynamically to a R123 ORC subcritical cycle (Chen et al., 2006). The total system efficiency of the CO_2 transcritical cycle was proven to be higher than that of a R123 subcritical cycle due to better matching of the CO_2 flow temperature variation to its heat source temperature glide.

In addition, the CO_2 power system is more compact and the cycle also shows no pinch limitation in the heat exchanger. This result is encouraging since the R123 subcritical cycle was formerly recognised to harbour a higher system performance (Madhawa et al., 2007). Significantly, this research demonstrates the importance of the design and selection of the high side supercritical CO_2 gas heater and optimal supercritical pressure control in order to determine overall system efficiency (Cayer et al., 2009). However, comprehensive experimental and theoretical analyses for a low-grade T-CO_2 system are

necessary for full understanding of system operations and achieve optimal system designs and controls.

2.3 Summary

It is know from the literature that the heat source temperature is an important parameter in determining the appropriate selection of working fluids in an ORC system. However, the detailed effects of the heat source temperature on the expander efficiency and system performance need to be further investigated. In addition, the operation of an ORC system is more complicated than that of a conventional refrigeration system. An ORC liquid pump can take an important role in the system operations and controls but this also needs further investigation. However, a review of the previous literature reveals that large information can be found on theoretical research of comparisons between basic ORC systems, which need to be further investigated.

Accordingly, this thesis introduces a small-scale R245fa ORC system test rig in which a turboexpander, scroll expander and air cooled finned-tube condenser were utilised. The effects of heat source temperatures and R245fa liquid pump speeds, heat sink flow velocity and the effects of recuperator installation on the efficiency of different expanders, the impact factors of different evaporators and system performances have been measured and analysed. The research outcomes can significantly help in ORC fluid selection, system component design and system controls.

In addition, a test rig of a low temperature power generation system with the T-CO_2 power cycle was overviewed and measured to see the effects of CO_2 mass flow rates and heat source flow rates on the performances of system and gas generator. The research outcomes can help understand the operation of T-CO_2 system and evaluate the optimisation of system design and controls.

Also, for the thermodynamic analysis, the thermal and exergy efficiencies at different heat source and sink temperatures were calculated and analysed for the T-CO_2 and R245fa ORC systems with and without an integrated recuperator. The predictions and analyses can contribute towards justifying the feasibility of applying T-CO_2 into low-grade power generation and further development in this area.

Chapter 3 will present a thorough overview on the construction of the heat source system and a detailed outline on the design and construction of R245fa ORC test rig which include mechanical, electrical, control and monitoring systems.

Chapter 3 – EXPERIMENTAL SET-UP FOR THE INVESTIGATION OF THE PROPOSED R245fa ORGANIC RANKINE CYCLES

3.1 Introduction

A small-scale R245fa ORC system test rig utilising low grade heat sources to generate electric power was designed and constructed in a laboratory at Brunel University London. The R245fa ORC system was integrated with the existing combined heat and power (CHP) unit and thermal oil rig to form an overall test facility. To measure the performance of the system and its main components, monitoring systems and instruments were also fitted into the system. This chapter presents an overview on the construction of the heat source system and the ORC test facility which incorporates mechanical, electrical, control and monitoring systems.

3.2 Heat Source System Design and Component Selection

The heat source system was designed for investigating the performances of R245fa ORC systems and T-CO_2 systems through waste heat from a combined heat and power (CHP) unit. Fig. 3.1 shows a schematic diagram of the arrangement of the heat source system and both the power generation systems. The exhaust gas from the CHP unit was recovered to heat a heat transfer medium, thermal oil, using an exhaust gas-thermal oil boiler. The hot thermal oil was then circulated via a thermal oil circulation pump to the evaporator or gas generator of power generation system, which then circulated back to the oil boiler to be heated again. Therefore, the heat source system consisted of two main operational loops, CHP unit and thermal oil transporting loop.

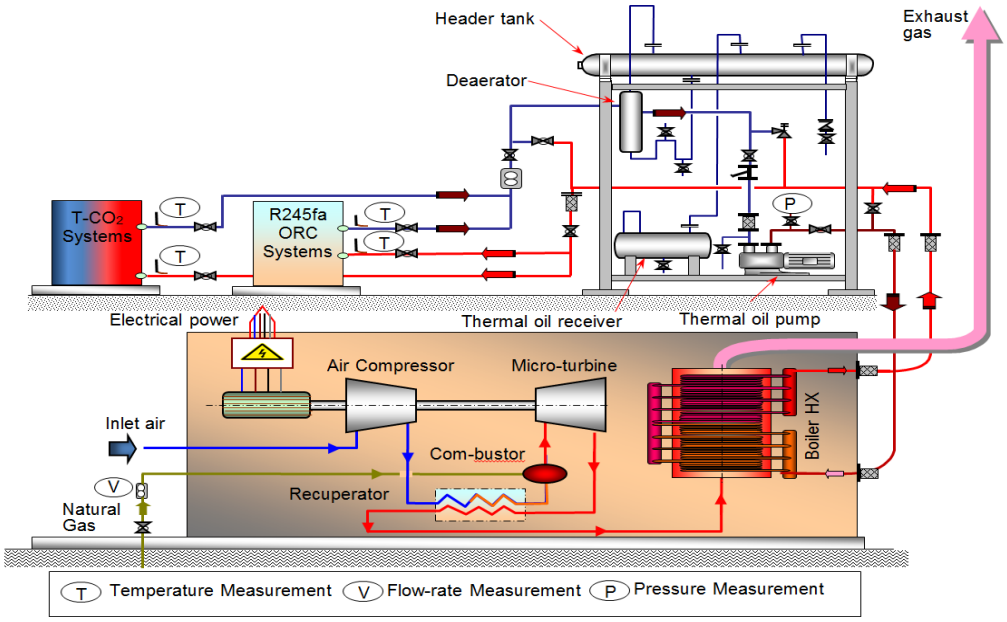

Figure 3.1 Integration arrangement of the heat source system and both power generation systems

3.2.1 Combined heat and power unit

The combined heat and power unit is basically an 80kW$_e$ recuperated micro-turbine generation system with built-in exhaust gas-thermal oil heat exchanger installed after the recuperator. The unit consisted of three main compartments, control and power output bay, the engine and recuperation bay, and finally the exhaust gas recovery bay. Fig. 3.2 illustrates the experimental setup of the CHP unit and the connection pipe from the exhaust gas recovery bay to the oil rig.

Figure 3.2 Combined heat and power unit

The engine of the CHP unit contained a prime rotation unit which consists of a single stage radial compressor, a single radial turbine within a combustor, and a high speed and permanent magnet alternator. All the components were on the same rotor shaft, as shown in Fig. 3.1. The electrical power output from the alternator was fed to a power conditioner and switchgear circuits in the control and power out bay and connected to the electric grid in the campus. The electrical power output from the CHP unit could be adjusted from 4.5kW to 80kW. Therefore, the thermal oil (heat source for power generation systems) temperature could be modulated by means of the CHP power output controls (Ge, et al., 2009)

In order to increase the system efficiency, an exhaust gas to air heat exchanger (recuperator) was attached to the microturbine. It extracted heat from the exhaust gases after the microturbine pre-heat the compressed air before it flowed into the combustor. This process reduced the fuel required to heat the compressed air which helped increase the efficiency of CHP unit.

In addition, the percentage of exhaust gas flow from the outlet of microturbine to the recuperator can be adjusted via an actuator driven a bypass valve. This would also change the exhaust gas temperature available for secondary heat recovery given to the thermal oil, without having to change the electrical power outlet.

Maximum recuperation will lead to maximum electric power output and minimum thermal output. No recuperation, on the other hand, will lead to minimum electric power output and maximum thermal output. Recovering the waste thermal energy from the exhaust gas, the CHP unit is complete with an exhaust gas recovery bay. The bay consists of components that provide secondary heat transfer facility. An exhaust gas-thermal oil heat exchanger was installed in this bay to recover waste thermal energy from the flue gas.

Natural gas was used as the primary fuel source for the CHP unit. The natural gas was supplied externally using a gas boost compressor and gas train. The gas was initially supplied at pressure of 21 mbar which was then pressurised at 5.5 bars by the boost compressor before entering the gas turbine.

3.2.2 Thermal oil and its transport loop

The thermal oil, manufactured by Global Oil Company (Europe) Ltd was used as a high temperature heat transfer fluid in the oil rig system. It's working temperature ranges from 0 ^{o}C to 340 ^{o}C. Any variation with the temperature of the thermal oil could directly affect its thermophysical properties, including its density, specific heat capacity, thermal conductivity and kinematic viscosity. Based on the manufacturer's data, the variations in the properties of the thermal oil with temperature are presented in Appendix-B.

To facilitate the heat transfer and energy balance analysis of the evaporator/ gas generator, the thermal oil properties were correlated from the manufacturer's data for the thermal oil temperature ranging from 0 ^{o}C to 340 ^{o}C:

For density (kg/m^3),

$$\rho = -0.65035606T + 875.94428 \tag{3.1}$$

For specific heat capacity (kJ/kg.K),

$$C_p = 0.0036446769T + 1.8087169 \tag{3.2}$$

For thermal conductivity (W/m.K),

$$\kappa = -7.2360691 \times 10^{-5} T + 0.13570055 \quad (3.3)$$

For kinematic viscosity (mm^2/s),

$$\mu = 27604.397 T^{-1.879364} \quad (3.4)$$

The thermal oil rig, as shown in Fig. 3.3, was designed to accommodate the volume expansion of the oil and to prevent any vapour release in the atmosphere during the oil circulation phase. At the same time, the system also provided adequate flow to transfer heat to the evaporator/ gas generator.

The primary components of the oil rig included an oil regenerative turbine pump, flow control valves, a safety valve, a deaerator, a heater and receiver tank, and connecting pipes. For the measurement purpose, several pressure gauges, thermocouples and an analogue thermometer were installed in the oil rig. The oil was circulated by the regenerative turbine pump specified for high working temperature. It had maximum heat of 80m and volume flowrate of 100 litres per minute. The thermal oil pump was driven by an electrical motor with power rating of 2.8 kW at 2800 rpm. The speed of the thermal oil pump was controlled by a frequency drive inverter by modulating the flow rate of thermal oil through the evaporator/ gas generator of the power generation systems. This ensured a comprehensive range of possible heat source (thermal oil) conditions and thus a comprehensive range of possible operation parameters of the heating loop that could be investigated.

A tank of 31 litres was positioned on the top of the oil rig. This particular size of the tank was selected to ensure an adequate space for the expansion of oil when at high temperature. The total charge of the oil rig for the system was 71 litres. The oil would expand about 10% in volume when its temperature increased from 20 ^{o}C to 200 ^{o}C.

In order to examine the performances of R245fa ORC system and T-CO_2 system, four two-way valves were installed between the power generation systems and the oil rig. And thus, the test rig can be used to examine and compare the differences between

R245fa ORC system and T-CO_2 system by turning the two-way valves on or off. The detailed positions of the valves are illustrated in Fig. 3.1.

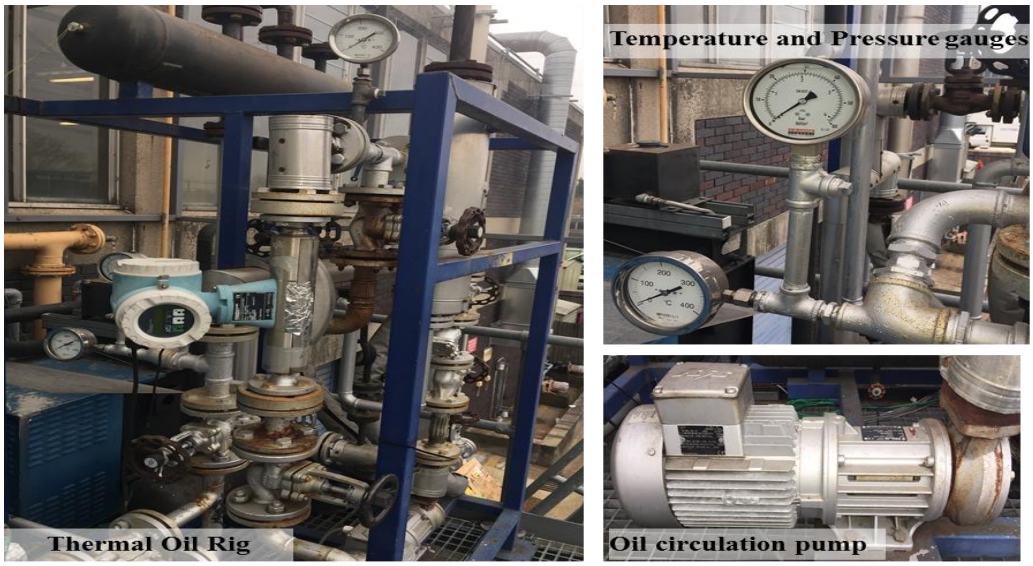

Figure 3.3 Oilrig completed with circulation pump, temperature and pressure gauges

3.3 R245fa ORC System Design and Component Selection

The experimental setup of the proposed R245fa ORC systems for this project is overviewed in this section. Fig. 3.4 shows a detailed schematic diagram of the R245fa ORC test rig design and Fig. 3.5 illustrates the R245fa ORC test rig with heat source system installed in Brunel University London.

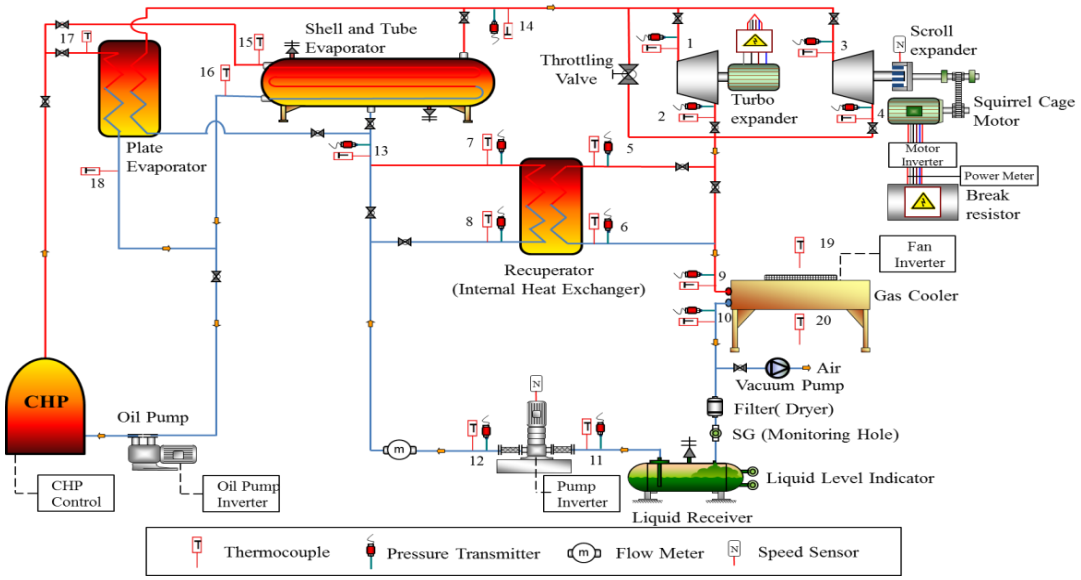

Figure 3.4 Schematic diagram of R245fa ORC test rig with heat source system

Figure 3.5 R245fa ORC test rig with heat source system in Brunel University London.

The R245fa ORC system consisted of a number essential components: an oil heated plate-type evaporator and an oil heated shell and tube type evaporator, R245fa turboexpander/ turbine and R245fa scroll expander and squirrel cage motor, plate-type recuperator, finned-tube air cooled condenser, liquid receiver, liquid pump and other ancillary equipments. During the experimental setup and testing period, a number of replacements were conducted with some components in order to get better system working hours and improved performance.

The details of the main mechanical components of ORC system will be described in following sections of 3.3.1 – 3.3.8.

3.3.1 R245fa evaporator

The selection of heat exchangers for the ORC system takes into consideration the specific operating conditions of each heat exchanger. The evaporator selected for the experiment was a shell and tube heat exchanger. The ORC fluid was on the shell side while the thermal oil was on the tube side. The main parameters of shell and tube evaporator are shown in Table 3.1.

In addition, a plate-type evaporator was installed in parallel to the shell and tube evaporator to absorb heat from the heat source (thermal oil), where the sub-cooled or

preheated liquid working fluid was heated to superheated vapor. The ORC fluid was on the left side flowing from bottom to top while the thermal oil was on the right side passing from top to bottom. The evaporator had total heat transfer area of 2.39 m^2 and 40 plates, while, the thermal oil flowed through 20 channels and the R245fa flowed through 19 channels. The main characteristics of plate-type evaporator are summarised in Table 3.2. The photographs of shell and tube evaporator and plate-type evaporator are shown in Fig.3.6. At the same designed heating capacity, the size of shell and tube evaporator is larger than that of plate one.

Table 3.1 Main parameters of shell and tube evaporator

	Parameters	
Shell	Gross volume/ L	40
	Working fluid	R245fa
	Shell inside diameter/mm	206.3
	Max. working fluid pressure/ bar	16
	Max. working fluid temperature/ ^oC	250
	Baffle spacing/mm	134
Tube	Gross volume/ L	14
	Working fluid	Thermal oil
	Tube inside diameter/ mm	12.6
	Max. working fluid pressure/ bar	10
	Max. working fluid temperature/ ^oC	250
	Wall thickness of tube/ mm	1.6
	No. of tube per row	8
	Single pass tube length/ m	1.4

Table 3.2 Main parameters of the plate-type evaporator

Parameters	Side 1	Side 2
Flow type	Counter-Current	
Total heat transfer area/ m^2	2.39	
Number of plates	40	
Vertical distance between centres of ports/ mm	479	
Horizontal distance between of ports/ mm	72	
Ports diameter/ mm	24	
Max. working fluid pressure/ bar	31	
Max. working fluid temperature/ ^oC	225	
Working fluid	Thermal oil	R245fa
Number of channels	19	20

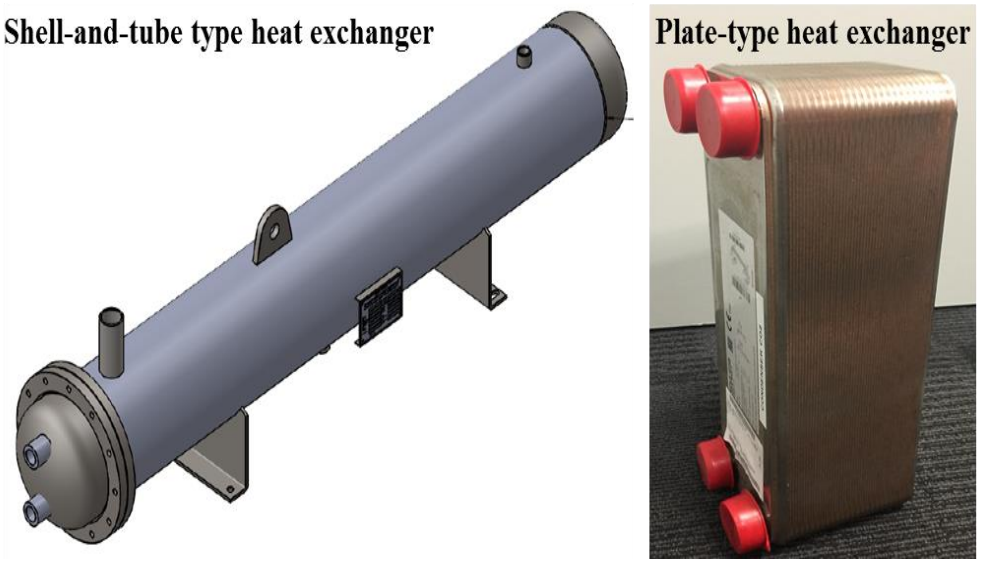

Figure 3.6 Photographs of shell and tube type and plate-type heat exchangers

In order to examine the integration effects of shell and tube type and plate-type evaporators in ORC systems, three two-way valves were installed on both heat source and ORC sides of evaporators. And thus, the test rig could be used to examine and compare the differences between the ORC systems running with shell and tube evaporator or plate-type evaporator by turning the two-way valves on or off. The detailed valve positions are shown in Fig. 3.4.

3.3.2 R245fa expander and generator

The R245fa ORC test rig consisted of two expanders, namely turboexpander and scroll expander. The extremely compact turboexpander, which is shown in Fig. 3.7 (a), was integrated with a high speed and permanent magnet synchronous generator. The maximum working fluid temperature and pressure through the turboexpander were 120 ^{o}C and 14 bar respectively. The power generator was driven by an ABB inverter and connected to the electric grid in the campus. The turbine inverter is shown in Fig. 3.7 (b).

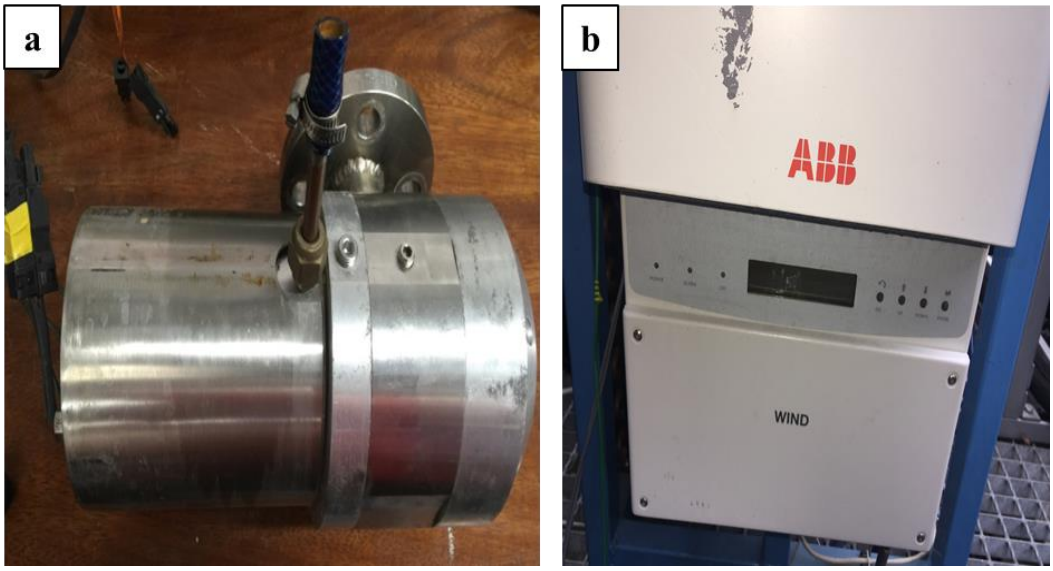

Figure 3.7 Photographs of the system components. (a) R245fa Turboexpander, (b) R245fa turboexpander inverter

In addition, after one of the evaporators, the superheated vapor also flowed through a scroll expander and thus drove a generator to generate electricity power. The generator was connected to a break resistor so as to investigate the expander performance at variable electric loads. Fig. 3.8 (a) illustrates the scroll expander part.

The scroll expander was a positive displacement with lubricant oil free and established by two identical spiral-shaped scrolls fixed on a back plate. The stationary scroll had ports in the back plate while the orbiting scroll moved in a circular path. The superheated working fluid entered the central chamber through the fixed back plate centre inlet port and exited from the chamber exhaust through the outlet port of the back plate. Therefore, the scroll expander can be classified as kinematically constrained.

The torque output from the scrolls was collected at three crank arms installed between the peripheries of the stationary orbiting scrolls at 120^{o} intervals. Thus, the crank arms could be used as anti-rotation devices for the orbiting scroll, supported by individual roller bearings at both sides. And these power transmitting shafts were in turn engaged with the inner shaft bearing, which is at the centre of orbiting scroll plate. The final power output of scroll expander was delivered through the inner shaft connected to centre of the inner shaft bearing.

However, the major disadvantage of an open-drive scroll expander was the internal and external gas leakages. The internal leakage was due to small quantity of working fluid leaking between the gaps of scroll wraps during the flow from high-pressure chambers to low-pressure ones, while the external leakage was due to the absence of tightness.

In this study, the scrolls were installed inside a rigid steel container and the inner shaft did not go through the orbiting scroll plate. The power was then transferred from the inner shaft to an outer shaft by means of a magnetic coupling, which was made by permanent magnets. A detailed drawing of the scroll expander part is shown in Fig. 3.8 (b). At such a circumstance, the scroll expander did not require any auxiliary power supply. Working fluid leaked from both internal and external was collected inside of the steel container which flowed together with the main working fluid stream. The picture of leaking container of the scroll expander is shown in Fig. 3.8 (c).

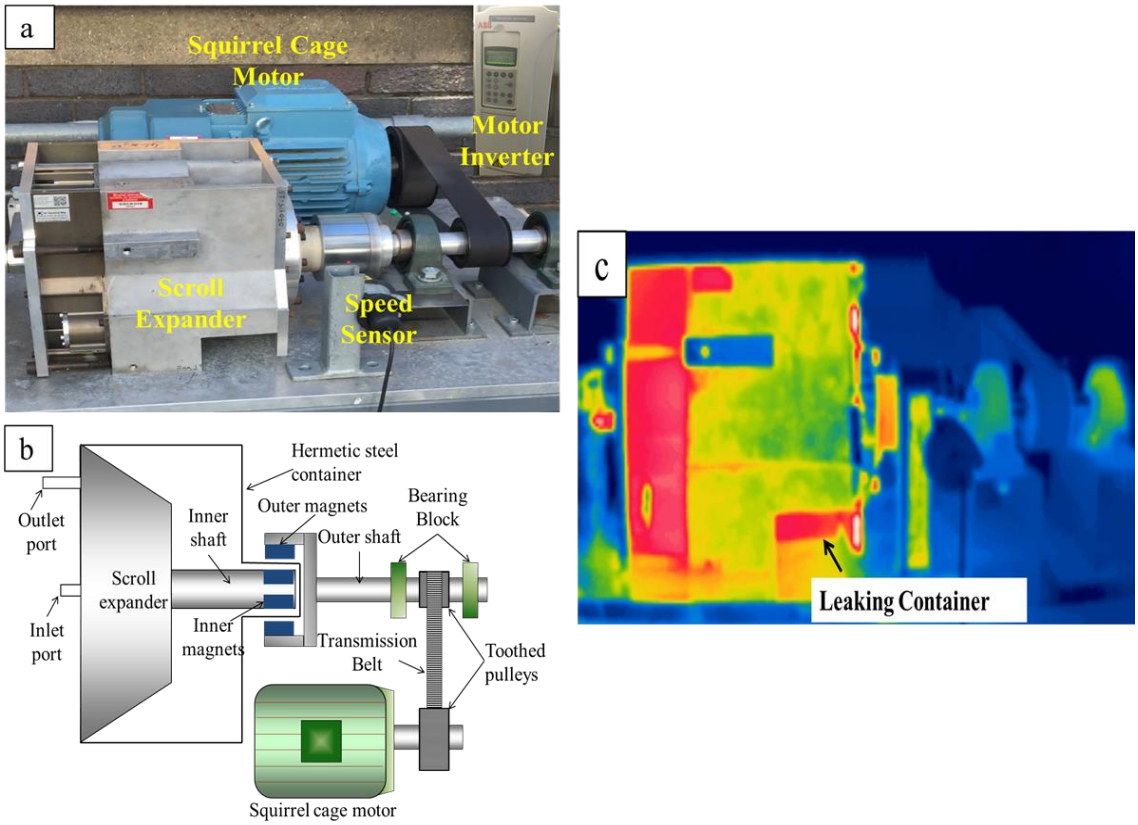

Figure 3.8 Photographs of the scroll expander with squirrel cage motor and details

Connected to the outer shaft, an asynchronous machine was driven by the scroll expander through a belt-and-pulley coupling. Using the asynchronous machine was a

suitable way to impose the rotational speed of the scroll expander, which could be adjusted by means of an ABB 4-quadrant inverter. Therefore the asynchronous machine could be able to run both motor and electric generator modes. Some basic parameters of the scroll expander are listed in Table 3.3.

Table 3.3 Main parameters of the scroll expander

Parameters	
Volume ratio	3.5
Displacement/ cm^3/ Rev.	73
Max. speed/ RPM	2600
Max. inlet pressure/ bar	13.8
Max. inlet temperature/ ^oC	175
Lubrication	Oil-free

In order to examine the integration effects of turboexpander and scroll expander in the ORC systems, four two-way valves were installed on both inlet side and outlet side of expanders. Therefore, the test rig can be used to examine and compare the differences between the ORC system running with turboexpander or scroll expander by turning the two-way valves on or off. The detailed valve positions are shown in Fig. 3.4.

3.3.3 R245fa recuperator

In order to examine the integration effect of recuperator in the ORC system, four two-way valves were installed respectively on both hot and cold side of the recuperator, which was designed as plate-type heat exchanger, as shown in Fig. 3.4. And thus, the test rig can be used to examine and compare the differences between the ORC system running with or without recuperator by turning the two-way valves on or off. The plate-type recuperator had total heat transfer area of 2.18 m^2 and 80 plates, while, the liquid R245fa flowed through 39 channels and the vapour R245fa flowed through 40 channels. The main characteristics of plate-type recuperator are summarised in Table 3.4.

Table 3.4 Main parameters of plate-type recuperator

Parameters	Side 1	Side 2
Flow type	Counter-Current	
Total heat transfer area/ m^2	2.18	
Number of plates	80	
Vertical distance between centres of ports/ mm	234	
Horizontal distance between of ports/ mm	63	
Ports diameter/ mm	33	
Max. working fluid pressure/ bar	31	
Max. working fluid temperature/ ^oC	225	
Working fluid	R245fa (liquid)	R245fa (vapour)
Number of channels	39	40

3.3.4 R245fa condenser

From the recuperator hot side outlet/ expander outlet, the low pressure R245fa flowed directly into the finned-tube air cooled condenser and was condensed into subcooled liquid before being collected in the liquid receiver. As shown in Fig. 3.9, the condenser was suspended tightly between two upright metal frames of the purpose-build test facility. A propeller air fan with variable speed control was installed above the heat exchanger to maintain a passage of fixed air flow. Above this were a number of smaller air fans installed in both the opposite directions along the pipe length, which would be switched on if the controlled air on temperature was higher than ambient. A part of the hot exhaust air would flow back through the return air tunnels, the return air grills and finally mix with the lower temperature ambient air flow. If the mixed air flow temperature was still lower than the designed air temperature, an electric air heater installed just below the heat exchanger would be operated in order to maintain the air on temperature. The main parameters of finned-tube air cooled condenser are summarised in Table 3.5.

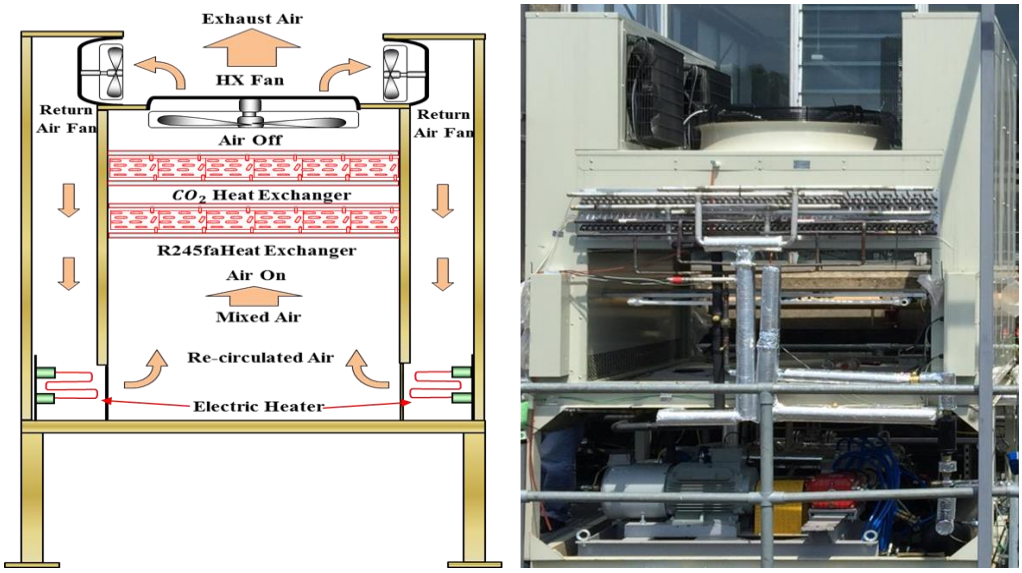

Figure 3.9 Photographs of R245fa and CO_2 Condensers

Table 3.5 Main parameters of air cooled R245fa finned-tube condenser

Parameters	
Surface area/ m^2	2.646
Maximum air speed through condenser ($ms^{-1)}$	1.53
Total working fluid pipes (inlet/ outlet)	60
Number of main fan	1
Number of re-circular fans	4
Number of re-circular air heaters	12
Main fan control	Variable speed
Re-circular fans control	On/ off

3.3.5 R245fa liquid pump

After the R245fa was desuperheated, condensed and sub-cooled in the air cooled condenser. The term 'desuperheated' represents reduced temperature of superheated R245fa at the expander outlet to a temperature close to its saturation temperature by the condenser. The sub-cooled liquid R245fa was fed into the liquid receiver. From the liquid receiver, the working fluid was then pumped back to the evaporator/ recuperator cold side to continue another operation cycle. The working fluid pump adopted in the system was a seal-less diaphragm type pump and direct coupled to a 1.1 kW asynchronous motor. Similar to the condenser fan, the liquid pump speed could also be

controlled by a frequency drive inverter which could modulate the working fluid flow rate and operating pressures in the ORC cycle.

Cavitation can be quite a threat during the operations of working fluid pump as it can lead to severe damage of the pump and flow rate reduction if not prevented in time. Cavitation happens when the working fluid at the inlet of the pump get close to saturation. Cavitation is considered to be more serious with organic working fluids since compared with water; they have lower latent heat of vaporization and evaporation temperature (Yang et al., 2015). In addition, for liquid pump in ORC system, cavitation results in a decrease of volumetric flow, an increase in pump vibrations and energy input losses in the pump. Thus, it will further reduce the ORC system efficiencies (Landelle et al., 2017). To avoid this phenomenon in the test rig, a deep tube receiver was installed before the pump and the quality of the R245fa liquid was visually monitored via the sight glass to ensure only liquid entered the working fluid pump. The photograph of R245fa ORC working fluid pump is shown in Fig. 3.10.

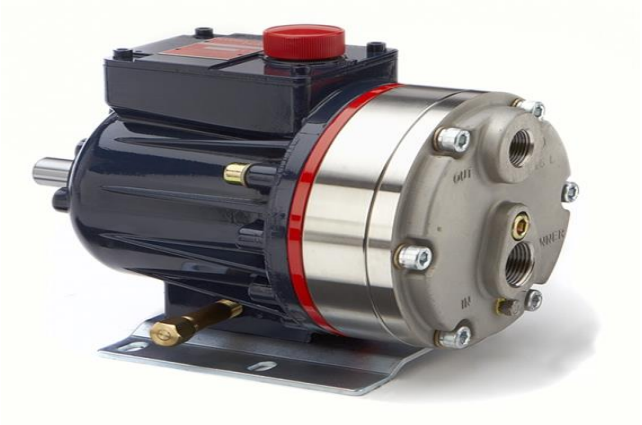

Figure 3.10 Photograph of R245fa liquid pump

3.3.6 Working fluid flow control devices

Three types of working fluid flow control devices were used in the R245fa ORC system as shown in Fig. 3.11. The ball valves (Fig. 3.11 (a)) are manually operated and used for isolating the system components such as: evaporators, expanders, recuperator, condenser and working fluid pump in the system, and also for servicing and safety (ASHRAE Standard 15, 2007). The system is protected from two high pressure relief

valves and two low pressure relief valves (Fig. 3.11 (b)). High and low pressure relief valves were set at 17.5bar and 6 bar respectively.

In addition, the bypass subsystem, where a needle valve (Fig. 3.11 (c)) was installed in parallel to the turboexpander and scroll expander, was used in this system to bypass a fraction of R245fa vapour to prevent it entering the turboexpander /scroll expander during the starting and closing processes. R245fa is usually operated at two phase condition at the evaporator outlet and can end up damaging the blades of turboexpander, and mechanical vibrations for the scroll expander.

(a)Ball valve (b)Pressure relief valves (c) Needle valve

Figure 3.11 Working fluid flow control devices

3.3.7 Auxiliary components

Some of the auxiliary components associated with the main ORC have been overviewed in the sections above. Other auxiliary components, as shown in Fig. 3.12, include a filter drier, sight glass on receiver, sight glass before receiver and schrader valve.

A filter drier (Fig. 3.12 (a)) was installed in the air-cooled condenser to liquid receiver pipeline to ensure no solid debris can flow into the working fluid pump. Another purpose was to reduce the humidity of the pipeline before charging the pure R245fa.

Two sight glasses are equipped in the ORC system. One (Fig. 3.12 (b)) was installed on side face of the liquid receiver to monitor the liquid level of working fluid in the receiver. The purpose was to ensure enough liquid flow into the working fluid pump. Another sight glass (Fig. 3.12 (c)) was fitted before filter drier to monitor the presence of condensed working fluid flow into the receiver.

After the fabrication of the ORC system, the system was pressurized with nitrogen gas in order to check any openings that could result in leakage. When the tight sealing of nitrogen gas was ensured in the system, vacuum pump was then connected in the piping loop using a schrader valve (Fig. 3.12 (d)). Several of these valves have been installed along the pipeline of the ORC system in order to each the vacuum process of each component during servicing period. Once the system was fully vacuumed, the working fluid in R245fa cylinder (Fig. 3.12 (e)) was charged into the working fluid receiver of the test rig by the recovery unit. The amount of R245fa charge is 50 kg when the system is running with plate-type evaporator and 75kg when the system is running with shell and tube evaporator.

(a) Filter drier (b) Sight glass on receiver (c) Sight glass (d) Schrader valve (e) R245fa

Figure 3.12 The auxiliary components

3.4 Control System

The control system was categorised in three parts. The first part was heat source controllers, which include the heat source temperature control and heat source mass flow rate control. The heat source temperature was controlled by the control panel attached on the CHP unit, as described in Section 3.2.1. The heat source mass flow rate can be controlled manually by the variable frequency drive attached on the oil pump.

Secondly, the ORC or T-CO_2 system controllers, which regulates the working fluid mass flow rate and evaporating pressure controls. Both parameters can be controlled manually by different frequency of the inverter attached on the ORC or T-CO_2 pump. In

addition, the inverter working with ORC or T-CO_2 pump can be selected manually according to the system running. Finally, the heat sink control system, which includes the heat sink temperature and flow rate, as described in Section 3.3.4.

The control system also included an electrical control system and electronic control system. The main function of the electrical control system was to connect or to disconnect electrical power supply to each electrical component and the electronical control system. The electronic controller consisted of a main controller system (RDM PR0650-TDB) with several communication modules and a displayed touch screen.

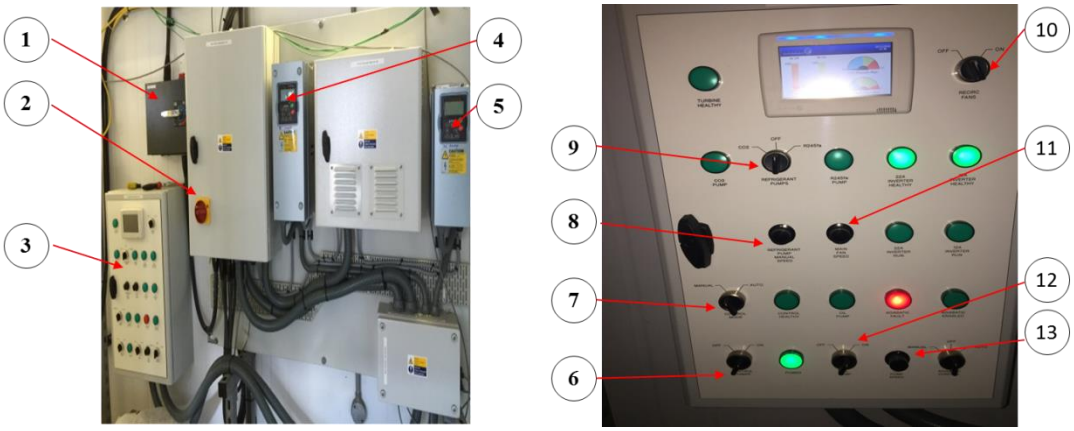

Legend:
1= main power switch
2= Electrical control system
3= main control panel
4= R245fa/CO_2 working fluid pump inverter
5= oil pump inverter
6= main control panel power switch
7= control mode (manual/ auto)
8= working fluid pump manual speed (Hz)
9=working fluid pump selection (CO_2/ off/ R245fa)
10=recircal fan (on/ off)
11=main fan speed (%)
12=oil pump (on/ off)
13=oil pump speed (Hz)

Figure 3.13 Electrical control panel of R245fa ORC and T-CO_2 systems.

The electrical and electronic control systems were installed in an electrical control panel which was placed in the CHP chamber. A front view of the control panel showing electrical control system, main control system, main switch and inverters for each pump are illustrated in Fig. 3.13. The figure also illustrates switches, indicator lights, adjusters and displayed touch screen of the main control panel.

3.5 Instrumentation and Data Logging System

The instrumentation was used for both control and performance monitoring. For control, the instrumentation was mainly used to provide signal inputs to the control panels for the safety issues. For performance monitoring, the instrumentation was used to display the state and flow conditions of the working fluid such as temperature, pressure and flow rate at different location of the systems. In addition, the instrumentation is also used to monitor the power generation of the system, ambient air flow rate and speeds of pump and scroll expander. To enable the data to be read and recorded for the system analyses and evaluation, the instrumentation was connected to a data logging system.

3.5.1 Instrumentation devices

The instrumentation devices used in R245fa ORC system were temperature and pressure sensors, a working fluid flow meter, power meter, airflow meter, speed sensor for working fluid pump and scroll expander, and infrared thermography. All the calibrated instrumentation and measuring points are shown in Fig. 3.4. Each of the following sections provides an overview of individual instrumentation device used for the ORC system.

3.5.1.1 Temperature and pressure measurements

To measure the performance of the system and its main components, a temperature sensor and a pressure transducer were installed at the inlet and outlet of each component in the ORC system. All the thermocouples and pressure transducers were inserted into the pipelines at locations close to each component of the system.

Every temperature in the system was measured by a K-type 310 stainless steel sheath thermocouple. In addition, the thermal oil and air flow inlet and outlet temperatures were also measured by K-type PTFE thermocouple at the evaporators and condenser. The K-type thermocouples have temperature measurement range -10 ^{o}C to 1100 ^{o}C with specific error (specified by manufacturer) of ±0.5 ^{o}C. All thermocouples were calibrated using a calibration bath and a precision thermometer (ASL type F250MK II, probe J100-250-10-NA) with accuracy of ±0.04 ^{o}C. The temperature range of calibration was set between 10 ^{o}C and 90 ^{o}C. It was found that all thermocouples had calibration error within the specifications. All of temperature measuring points in the ORC system and the calibration equations of each thermocouple with their calibration errors are summarised in Appendix C.

Fourteen pressure transducers in total were installed on the ORC system. The pressure transducers were mainly used for measurement purpose; however, were also used for the control system. The pressure transducers measured pressure within the range of 0~25 bar, and converted the measured value to a 0-10 V DC output signal with a 0.5s response time to the data logging system. Each pressure transducer was calibrated using a deadweight pressure gauge calibrator. The voltage outputs were recorded for a series of known pressures from the calibrator. The pressure range of calibration was set between 0 and 24 bar.

The relation of the voltage outputs against the pressures was then analysed along with derivation of best-fit linear equations. These equations were used in the data logging software to enable an automatic recording of the measured pressures depending on the voltage output. The coefficient of correlations of the pressure transducers were about 99.9% with manufacturer uncertainty of ± 0.3%. The calibration equations of the pressures transducers for ORC system can be found in Table C.2 (Appendix C).

3.5.1.2 Flow meter

In the R245fa ORC system, a twin tube type mass flowmeter was used to measure the liquid mass flow of R245fa after the pump. The flowmeter Optimass 1000-S15 (Fig. 3.14) could measure mass flow in the range of 0~6500 kg/h with an accuracy of ±0.15%.

In addition, the flow meter provided a current output 4-20 mA which is directly connected in the data logging system. In order to convert the current to a mass flow rate, a calibration was carried out by the manufacturer. The best-fit linear equation from the calibration was used into the data logging software to enable automatic recording of mass flow rate.

Figure 3.14 Flow meter Optimass 1000-S15

3.5.1.3 Power meter

The power generated by the ORC system is basically the power output of turboexpander and scroll expander. Both the expanders had single phase power output. In order to measure the power output, a power meter was installed in the electrical control panel. The power meter selected for the purpose was HAMEG HM 8115-2, as shown in Fig. 3.15. It is a single phase power meter which has accuracy class of ±0.8%. The measured voltage, current and power were displayed in the LED screen. The recorded data of power meter were also logged in the computer via a USB cable.

Figure 3.15 Power Meter HM8115-2

3.5.1.4 Hot wire anemometer

A hot wire anemometer, as shown in Fig. 3.16, was used to measure the ambient air velocity of the air-cooled condenser. The hot wire anemometer chosen to conduct the measurement was AIRFLOW INSTRUMENTS TA465 with an accuracy of ±0.15 m/s at full range of 1.27m/s ~78.7 m/s. Twelve test points were taken into consideration for

each main fan speed from 0% to 100% at 20% intervals in a single quadrant of the condenser. The other quadrants were assumed to be the same as the last test quadrant. The graphs of the main fan speed against the average air velocity were then plotted along with the derivation of the best-fit linear equation. This equation was once again used for the data analysis process. Both the graphs and equation are provided in Appendix C.

Figure 3.16 Air flow meter TA465

3.5.1.5 Laser speed sensor

The laser speed sensors, as shown in Fig. 3.17, were used to measure RPM of pump shaft and scroll expander shaft. The laser speed sensor used was the COMPACT VLS/DA1, unit measurement RPM, with an accuracy of ±0.75% at full scale of 50~6000RPM. The sensors provide a voltage output of 0-6 V which was directly recorded in the data logging system. In order to convert the voltage to RPM, calibration was carried out.

Figure 3.17 Speed sensor VLS/DA1

3.5.1.6 Infrared (IR) thermography

In order to investigate the working fluid flow in the air-cooled condenser and scroll expander, the infrared (IR) thermography type Thermal CAMTM S60 infrared camera from FLIR, as shown in Fig. 3.18, was used in the experiment. This is important to ensure the temperature difference between each pipe in the condenser. Also, the IR thermal imaging camera can provide a proportional temperature contour at scroll expander surface as additional visual data.

Figure 3.18 Infrared (IR) thermal imaging camera

3.5.2 Data logging system

To enable the measured data to be read and recorded for system evaluation and analyses, all measured experimental data were transmitted by a National Instruments (NI) data logger system and recorded automatically by a computer with LabView software. The output signals from individual instrumentation devices were logged by the data logger system which comprises of data acquisition modules, and recording and display system. The data acquisition modules basically unitise the NI cDAQ-9178, which consists of 8 channels and a USB cable connected to the computer. There are three different expansion modules connected to the data acquisition modules, each for the measurement of current, voltage and thermocouple individually. Overall, one data acquisition module and five expansion modules were prepared for the data logging, as shown in Fig. 3.19 (a). The computer sets for the data logging system is shown in Fig. 3.19 (b).

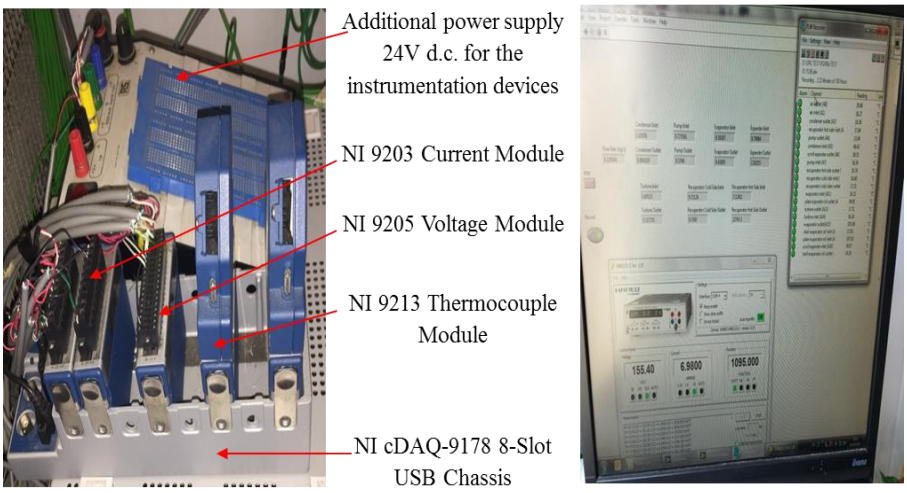

Figure 3.19 Data logging system and computer sets

3.6 Summary

This chapter overall provides a thorough overview on the construction of the heat source system, which consists of an 80kW$_e$ combined heat and power unit, also abbreviated as CHP throughout the chapter, and the thermal oil transport loop.

The chapter also explores and provides a detailed outline on the design and construction of a small-scale low-grade R245fa ORC test facility which incorporates various mechanical, electrical, control and monitoring systems. The test facility setup consisted of typical ORC system components, such as plate type and shell and tube type evaporators, a turboexpander with high speed generator, a scroll expander with a generator, plate-type recuperator, finned-tube air cooled condenser, ORC liquid pump and some auxiliary components. All the individual components used in the system and its purpose have been outlined in the chapter along with the instruments and devices used for measurement purpose. Various figures of the system and individual components have been illustrated where necessary.

The following chapter, Chapter 4, will present the test results from the experiments conducted on the R245fa ORC system with turboexpander and plate-type evaporator. The chapter will further discuss and highlight the effects of recuperator installation, variations of heat source temperatures, changes of R245fa liquid pump speeds and

condenser fan speeds on the turboexpander efficiency and the overall system's performance.

Chapter 4 – EXPERIMENTAL RESULTS AND DISCUSSION USING R245fa ORGANIC RANKINE CYCLES WITH TURBOEXPANDER

This chapter provides an overview of the as-built test facility and the experimental results from a series of tests carried out on the R245fa ORC system with turboexpander and plate-type evaporator. The discussion considers the performance of the ORC system with turboexpander at different heat source (thermal oil) temperatures and running speeds of ORC pump and heat sink (ambient air) velocities, when the system is with or without recuperator.

4.1 Overview of the As-built Test Facility and Test Conditions

In previous chapter, the experimental set-up and system components were described. The R245fa ORC test rig had a standard cycle design and consisted of two operational loops; a heat source where thermal oil circulates and the actual ORC loop where the R245fa flows. Both loops were connected by a plate-type evaporator heat exchanger. A simplified process flow diagram with the relative sensors position of an ORC test rig is illustrated in Figure 4.1. The ORC loop consisted of a number of essential components: an oil heated plate-type evaporator, R245fa turboexpander/ turbine and power generator, plate-type recuperator, finned-tube air cooled condenser, liquid receiver and liquid pump. In order to operate the appropriate operational conditions and stationary conditions, there were five main parameters that could be controlled during the experiment: the heat source temperature and mass-flow rate, the R245fa working fluid mass-flow rate and the heat sink temperature and mass-flow rate.

After the test rig was setup, a series of experiments were conducted to evaluate the performance of the ORC system with turboexpander at different heat source (thermal oil) temperatures and running speeds of ORC pump and heat sink (ambient air) velocities for both scenarios, when with and without recuperator. For the system without recuperator, the thermal oil temperature was controlled within the range of 138 ^{o}C to 156 ^{o}C by modulating the CHP system power outputs, while the speed of the ORC

pump was controlled within the range of 630RPM to 779RPM by changing the pump's motor frequencies.

On the other hand, for the system with recuperator, the thermal oil temperature control range was between 154 °C to 166 °C while the speed of ORC pump was varied between 580RPM to 731RPM. The condenser air velocity was set within the range of 1.5 m/s to 4 m/s by adjusting the frequency of the main fan of air-cooled condenser. Rest of the control parameters were kept constant.

These settings ensured the turbine inlet temperatures and pressures were within their maximum limits when the tests were conducted, with temperature set as 110 °C (120 °C for a short period) and pressure at 14bar respectively by the turbine manufacture. The results for the experiments using these operational and constant parameters are presented in Section 4.3.

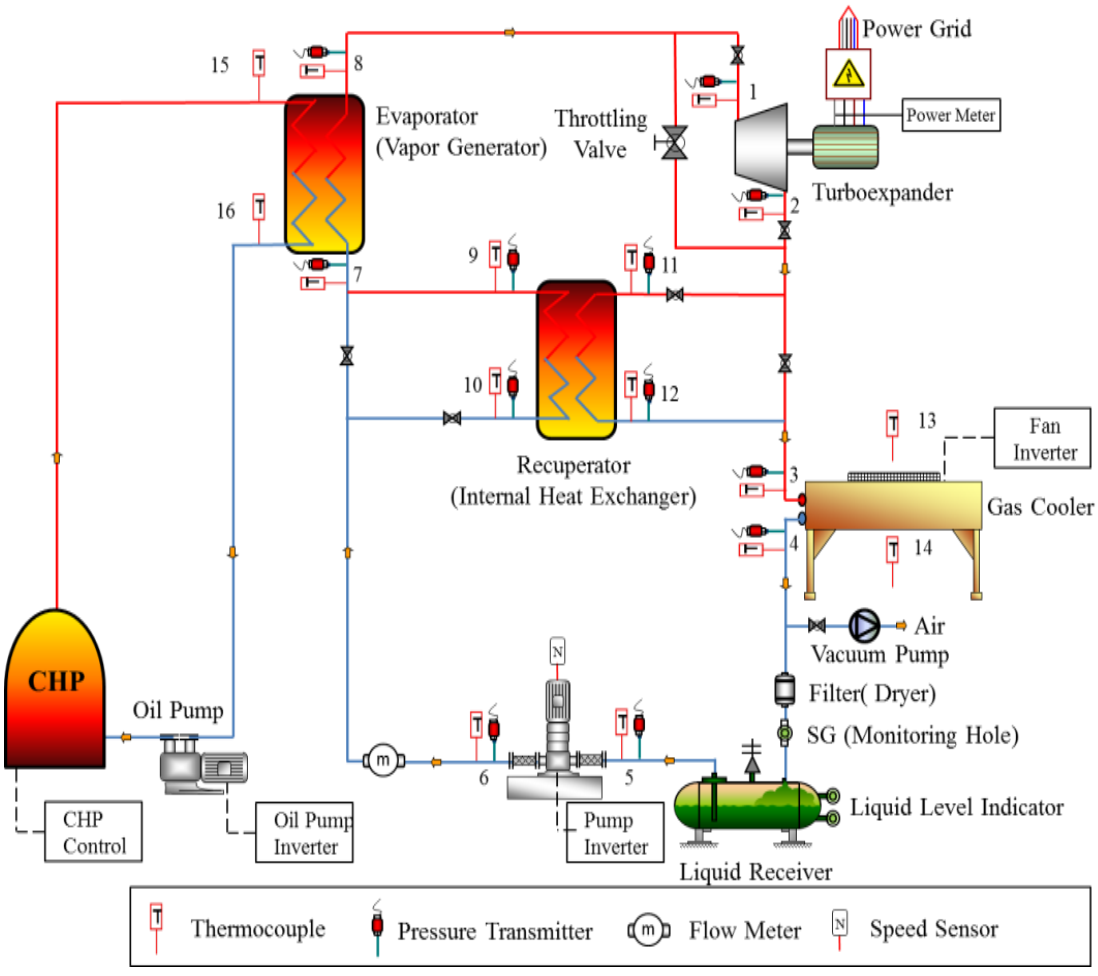

Figure 4.1 Process flow diagram with the relative sensors position of an ORC test rig with turboexpander

4.2 Experimental Data Collection and Processing

4.2.1 Experimental data collection

Measured performance parameters from the instrumentation devices such as temperatures, pressures, mass flow rate and other parameters of R245fa, heat source (thermal oil) and heat sink (ambient air) were recorded by a dedicated data logger when the system was at steady state. The steady state is the temperature of each system point in the range of ±2 ^{o}C and the pressure in the range of ±0.2bar. For all operating scenarios, a timeframe of 30 minutes was assigned to reach the steady state, with the data being recorded every one second. Once the steady state was achieved (with 1800 direct measurements), an average of the last 20 minutes (1200 measurements) was taken to find the measured data. For detailed explanation on the measurement instruments and data logging system, please refer Section 3.5 (Chapter 3).

4.2.2 Experimental data processing

Collected data were processed in a spread sheet programme. All relevant fluid thermophysical properties such as enthalpy and entropy etc. were calculated by REFPROP 8.0 software (Lemmon et al., 2007) based on the average measured temperature and pressure at each cycle point. The energy performance parameters of R245fa ORC system were then calculated, which included the isentropic efficiencies of turbine and ORC pump, the overall efficiency of turbine, and thermal and overall efficiencies of ORC system. The calculation also accounted the working fluid of pressure ratio of the turbine and pump power consumption.

4.2.2.1 Isentropic efficiencies of turbine and ORC pump

As shown in Fig. 4.1, the ORC system is a closed loop system, the first law of thermodynamics and mass conservation of working fluid can be applied to the ORC system analysis. The isentropic efficiencies of turbine ($\eta_{T,is}$) and pump ($\eta_{P,is}$) are calculated using Equations (4.1) and (4.2) based on the measurements. The variable subscript numbers in these equations are in correspondence to the ones indicated in Fig. 4.1.

$$\eta_{T,is} = \frac{(h_1 - h_2)}{(h_1 - h_{2,is})} \tag{4.1}$$

$$\eta_{P,is} = \frac{(h_{6,is} - h_5)}{(h_6 - h_5)} \tag{4.2}$$

The thermocouples and pressure transducers before the inlet and after the outlet of the turbine are installed to measure the temperatures and pressures in the ORC system. With the known temperatures (T_1 andT_2) and pressures (P_1 andP_2), the thermodynamic properties of state point 1 and point 2, in particular the enthalpy of point 1 (h_1) and point 2 (h_2) were calculated using REFPROP 8.0 software. For the isentropic expansion process of the turbine, the entropy value of point 2_{is} should be equal to point 1, which can be solved using the enthalpy of point 2_{is} ($h_{2,is}$). The pressure of point 2_{is} is the same as that of state point 2 as they both are on the same isobaric line. With the known values of pressure and entropy, the enthalpy valve ($h_{2,is}$) of the state point 2_{is} can be calculated via the REFPROP 8.0 software. The isentropic efficiency of turbine can then be calculated using Equation 4.1. Similarly, the isentropic efficiency of working fluid pump can be calculated using Equation 4.2.

4.2.2.2 Overall efficiency of turbine

As listed in Equation 4.3, the turbine's overall efficiency (Liang et al., 2014; Chen et al., 2002) can be calculated as a product of isentropic, mechanical and electrical efficiencies. The overall efficiency can also be calculated as the ratio of measured turbine power output and the turbine isentropic power output. Accordingly, if the mechanical efficiency is assumed as constant 0.98, the electric efficiency can be calculated. For this case, the electrical loss is the main sources of energy loss affecting the performance of the turbine according to the turbine manufacturer.

$$\eta_{T,all} = \eta_{T,is}\,\eta_{T,m}\,\eta_{T,e} = \frac{\dot{W}_T}{\dot{m}_f(h_1 - h_{2,is})} \tag{4.3}$$

where $\dot{m}_f$ is the ORC working fluid mass flow rate (kg/s) measured by the ORC flow meter, as described in Section 3.5.

4.2.2.3 ORC pump power consumption and ORC system thermal and overall efficiencies

When mechanical and electrical efficiencies are not included in the calculations of the overall efficiency for the pump, the power inlet of the pump can be calculated using Equation 4.4.

$$\dot{W}_P = \dot{m}_f(h_6 - h_5) \tag{4.4}$$

The system thermal ($\eta_{s,th}$) and overall ($\eta_{s,all}$) efficiencies can therefore be calculated using Equation 4.5 and 4.6 respectively. It should be noted that the thermal efficiency is calculated with the corresponding thermodynamic power cycle such that the mechanical and electrical efficiencies involved in the turbine and working fluid pump are not considered.

$$\eta_{s,th} = \frac{(h_1 - h_2) - (h_6 - h_5)}{(h_8 - h_7)} \tag{4.5}$$

$$\eta_{s,all} = \frac{\dot{W}_T - \dot{W}_P}{\dot{m}_f(h_8 - h_7)} \tag{4.6}$$

4.2.3 Uncertainty in calculation

Considering the uncertainty of measured variables, which include, R245fa temperatures, R245fa pressures, R245fa mass flow rates, and R245fa turbine power generations, an error margin was found for each variable. Thus, the uncertainty in the calculation of condenser heat capacity, evaporator heat capacity, turbine isentropic efficiency, turbine overall efficiency, system thermal efficiency and system overall efficiency were found to be ±0.35%, ±0.36%, ±11.74%, ±0.94%, ±1.09%, ±17.91% respectively. Detailed explanation of the uncertainty analysis is given in Append D.

4.3 Test Results

4.3.1 The effect of the heat source temperature swing

For this particular test, the effect of heat source (thermal oil) temperature on the ORC system performance was examined. During the test, the thermal oil was controlled within the range of 135 ^{o}C to 160 ^{o}C when the system was running without recuperator and from 154 ^{o}C to 166 ^{o}C when the system was running with recuperator. This control was achieved by modulating the CHP power outputs. The design parameters of the test are listed in Table 4.1. Operating parameters such as thermal oil flow rate, R245fa pump speed, condenser air flow rate and ambient air temperature were maintained at constant rate.

Table 4.1 The operating conditions for R245fa ORC systems without and with recuperator of thermal oil temperature swings

Recuperator of system In/ Out	Oil temperature ^{o}C	Oil flow rate Kg/s	R245fa pump speed RPM	Condenser air velocity m/s	Ambient air temperature ^{o}C
Out	135~160	0.65	680	3.67	17.0
In	154~166	0.36	680	3.67	18.5

For the test, the cycle point and thermal oil outlet temperatures were varied to see its effect on the system when without or with recuperator. The results for the test are illustrated in Fig. 4.2. For the system without recuperator, the measurements demonstrated that the evaporator outlet temperature of thermal oil and the R245fa fluid temperatures at turbine inlet and outlet, and condenser inlet increased linearly along with the increasing heat source temperature. With the turbine inlet temperature, however, a linear increase in temperature only occurred once the heat source temperature surpassed 140 ^{o}C. This illustrates that when the temperature of the heat source is below 140 ^{o}C, the R245fa fluid does not evaporate completely, requiring a higher temperature to ensure dry R245fa fluid at the evaporator outlet or the turbine inlet. Meanwhile, both the condenser and pump outlet temperatures were not affected much by the heat source temperatures when within constant heat sink parameters and pump speed.

It was also noted that the condenser outlet temperature or pump inlet temperature was more or less the same as the pump outlet temperature when the liquid pumping process was involved.

Precisely, for dry turbine operations, when the heat source temperature increased from 141 ^{o}C to 155 ^{o}C, the temperature of thermal oil outlet, turbine inlet, turbine outlet and condenser inlet increased about 9.0K, 25.6K, 27.8K and 27.8K respectively.

Similarly, for the system running with recuperator, the R245fa fluid temperatures at turbine inlet and outlet, evaporator inlet, and the thermal oil evaporator outlet increased along with the increasing heat sources temperature. Precisely, when the heat source temperature increased from 154 ^{o}C to 166 ^{o}C and the system with recuperator, the temperatures of thermal oil outlet, turbine inlet, turbine outlet and evaporator inlet increased about 7.6K, 22.2K, 28.9K and 13.9K, respectively. The temperatures for the condenser inlet and outlet and pump outlet, however, were not affected much by the heat source temperatures.

When analysing this particular test, the main difference noted between the system running with and the system running without recuperator is the different inlet temperature of evaporator and condenser. For the system with recuperator, the evaporator inlet working fluid was being heated by the working fluid flow from turbine outlet while the condenser inlet working fluid was being cooled by the working fluid flow from the pump outlet in recuperator. This caused the inlet temperature of the evaporator and condenser of the system with recuperator to be different that the one without.

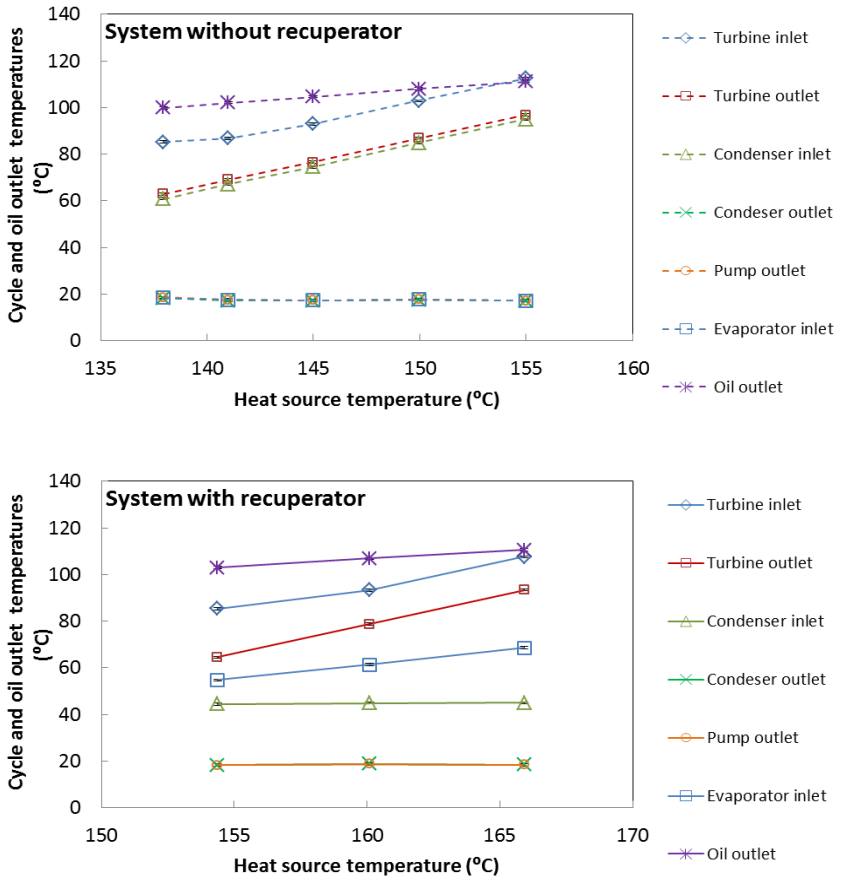

Figure 4.2 Variations of cycle point and thermal oil outlet temperatures with heat source (thermal oil) temperatures on system without and with recuperator

Fig. 4.3 illustrates the variations of cycle point pressures and pressure ratios between the turbine inlet and outlet with the increasing heat source (thermal oil) temperature for the system in both the scenarios.

Obviously, the working fluid pressure can be separated into two groups, high pressure side and low pressure side. For both the scenarios of the system, with and without recuperator, the pressure of pump outlet, evaporator inlet, evaporator outlet and turbine inlet comes under high pressure side. The pressure of turbine inlet is lower than the pressure of pump outlet, due to the pressure drop (loss) through the pipe connections and components etc. The low pressure side, on the other hand, includes the pressures of turbine outlet, condenser inlet, condenser outlet, and pump inlet.

The obtained results illustrate that the working fluid pressure at high pressure side experienced an increase along with the increasing heat source temperature. However,

the working fluid pressure at low pressure side did not result in much change. Subsequently, the pressure ratios of turbine inlet and outlet for both the systems increased along with the increasing heat source temperature.

It has been detected that the pressure ratios of the turbine in the system with recuperator were much lower than for the system without while the turbine inlet pressures for both the systems were within the same range. The turbine outlet pressures of the system with recuperator, on the other hand, were higher than for the system without, as presented in Fig. 4.3. For the system in both the scenarios, the cycle point pressures at each pressure side were different indicating the diverse fluid pressure drops throughout the connection pipes, fittings and components with the maximum and minimum pressure points at pump outlet and inlet respectively.

In percentage, when the temperature of the heat source increased from 141 ^{o}C to 155 ^{o}C for the system without recuperator, the cycle point pressures of ORC pump outlet, evaporator inlet, evaporator outlet, turbine inlet, turbine outlet, condenser inlet, condenser out, and ORC pump inlet amplified 7.41%, 7.46%, 7.49%, 7.89%, 4.12%, 4.38%, 1.34% and 0.38 respectively. When the temperature of the heat source was increased from 154 ^{o}C to 166 ^{o}C and the system with recuperator, the cycle point pressure of the ORC pump outlet, evaporator inlet, evaporator outlet and turbine inlet amplified 7.22%, 7.05%, 7.38% and 7.84%, respectively.

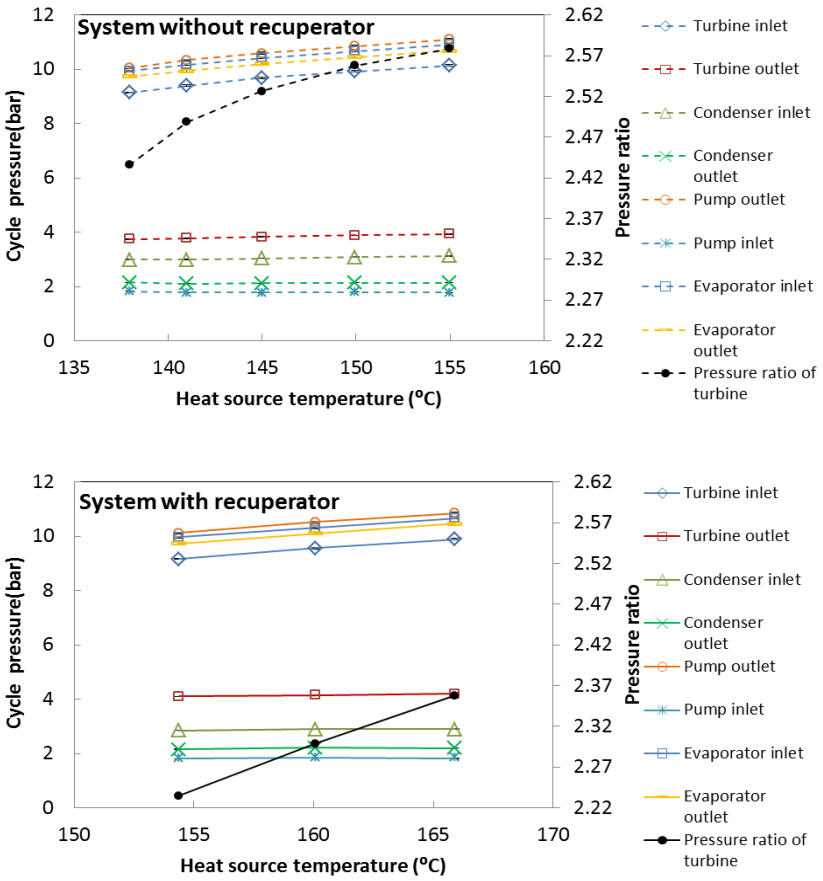

Figure 4.3 Variations of cycle point and thermal oil outlet temperatures with heat source (thermal oil) temperatures on system without and with recuperator

As shown in Table 4.1, a constant ORC pump speed was used for both the systems. The R245fa mass flow rate was kept constant at 0.25kg/s when the system was tested without recuperator. However, the mass flow rate was changed to 0.24kg/s and kept constant at this value when the system was tested at different heat source temperatures.

Based on the measured temperature and pressure at each component inlet and outlet, the pump power and evaporator and condenser capacities for both the systems could be calculated at different heat source temperatures, as shown in Fig. 4.4. The actual turbine power outputs for both the systems were measured directly with an installed power meter; the measured power outputs for the test are also illustrated in the same figure.

As expected, the increasing heat source temperature resulted in greater heat transfer rate to the evaporator, leading both the systems to have high evaporator heat capacities. Though the overall heat source temperature of the system with recuperator was higher

than the temperature of the system without, the overall evaporator heat capacity of the system, in contrast, was found to be much lower. In addition, for the system without and with recuperator, the increasing heat source temperature caused the condenser inlet temperature and condenser heat output to increase alongside.

In addition, as depicted in Fig. 4.3, the increasing heat source temperature also increased the working fluid pressure ratio of the turbine inlet and outlet and thus the turbine power output of both the systems. The turbine pressure ratio of the system with recuperator was much lower than the turbine pressure ratio of the system without causing the turbine power output to have similar effect. Compared to other input and output parameters, the pump power input of both the systems experienced a minimum increment with the changing heat source temperature.

Quantitatively, when the heat source temperature increased from 145 ^{o}C to 155 ^{o}C for the system without recuperator, the percentage increase rates of turbine power output, evaporator heat input, condenser heat output and pump power input were 13.6%, 12.7%, 9.4% and 6.6% respectively. When the heat source temperature increased from 154 ^{o}C to 166 ^{o}C for the system with recuperator, the percentage increased rate of turbine power output, evaporator heat input, condenser heat output and pump power input were 31.2%, 7.05%, 5.94% and 8.5% respectively.

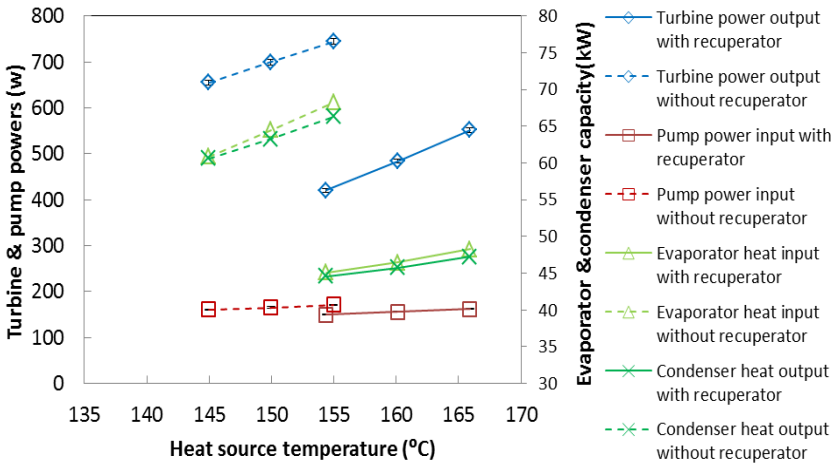

Figure 4.4 Variations of turbine and pump powers and evaporator and condenser capacities with heat source (thermal oil) temperatures on system without and with recuperator

The next stage of the test considered calculating the turbine's and the system's efficiency at different heat source temperatures when with and without recuperator. The results obtained for this part is illustrated in Fig. 4.5.

As illustrated in Fig. 4.3 before, the turbine pressure ratio increased along with the higher heat source temperature, leading the turbine isentropic efficiency and the system thermal efficiency to increase alongside. Due to lower turbine pressure ratios of the system with recuperator, the efficiencies of the turbine and the system were lower compared to the system without.

Similarly, as presented in Fig. 4.4, the evaporator heat inputs of the system with recuperator were found to be less than for the system without, meaning the system with recuperator had higher system thermal efficiency. The obtained results demonstrated that a recuperator could only be introduced in the system if the heat source temperature was sufficient enough (higher enough), else, the system efficiencies would result to be lower than for the system without.

In percentage, when the heat source temperature of the system without recuperator increased from 145 ^{o}C to 155 ^{o}C, the turbine isentropic, turbine overall, system thermal, and system overall efficiencies increased by 14.38%, 1.08%, 14% and 20.80% respectively. When the heat source temperature of the system with recuperator increased from 154 ^{o}C to 166 ^{o}C, the turbine isentropic, turbine overall, system thermal, and system overall efficiencies increased by 39.85%, 7.21%, 61.97% and 34.32% respectively.

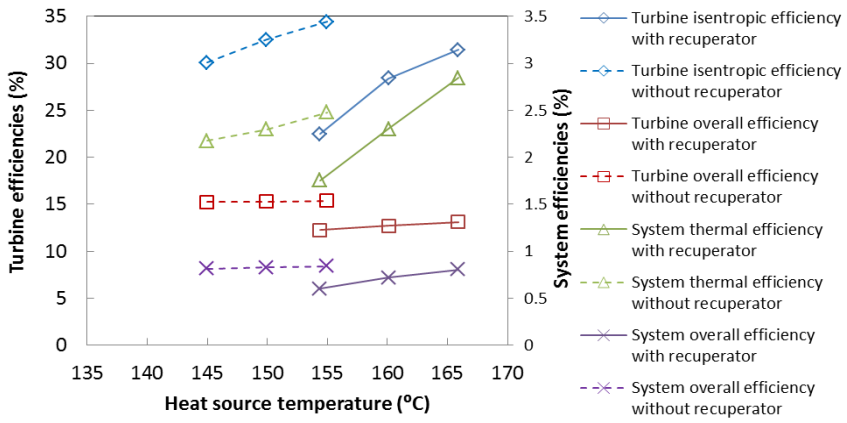

Figure 4.5 Variations of turbine and system efficiencies with heat source (thermal oil) temperatures on system with and without recuperator

4.3.2 The effect of the ORC pump speed swing

As shown in Fig. 4.1, an ORC liquid pump was installed after the liquid receiver. The pump speed could be controlled so as to modulate the ORC fluid mass flow rate and pressure at the turbine inlet. In order to examine the effect of variable pump speeds on the system performance, a test matrix of the ORC pump speed swing was designed for the system. The parameters of the test matrix are listed in Table 4.2. As can be seen in the table, the ORC pump speed swing could be varied between the range of 630 to 779 RPM for the system without recuperator, and from 580 to 731 RPM for the system with recuperator. Meantime, other parameters such as thermal oil (heat source) temperature, thermal oil flow rate and condenser air (heat sink) flow rate and its temperature were kept constant throughout the test.

Table 4.2 The operating conditions for R245fa ORC systems with and without recuperator of ORC pump speed swings

Recuperator of system In/ Out	Oil temperature ^{o}C	Oil flow rate Kg/s	R245fa pump speed RPM	Condenser air velocity m/s	Ambient air temperature ^{o}C
Out	131.1	1.08	630~779	3.67	17.0
In	156.1	0.366	580~731	3.67	18.0

Using the test parameters presented in Table 4.2, the changes in the turbine inlet, turbine outlet, condenser inlet, condenser outlet, pump outlet, evaporator inlet, oil outlet, and the ORC mass follow rates in respect to the increasing ORC pump speed were measured and recorded. This test was performed in the system, both when with and without recuperator. Fig. 4.6 illustrates the results.

For both the systems, the ORC mass flow rate increased along with the ORC pump speed. The increased mass flow rate in the system resulted in higher heat transfer rate from the heat exchangers (evaporator, condenser or recuperator). The increased heat capacity of the heat exchangers along with increasing pump speed resulted in decreased thermal oil outlet temperature. Similarly, for both the systems, the temperature of ORC evaporator outlet (turbine inlet) decreased with increasing ORC pump speed due to fixed heat source parameters.

Likewise, the turbine inlet temperature experienced a similar decline with the increasing pump speed, almost linearly when the ORC pump speed was increased from 580 RPM to 730 RPM. This indicates that when the pump speed was higher than 730 RPM, the ORC was at saturated state and the heat source capacity was not adequate enough to superheat the ORC fluid in the evaporator. The decline in the ORC fluid temperature at turbine inlet further triggered the fluid temperature at the turbine outlet to decrease.

As depicted from the results, the ORC pump speed of the system in both the scenarios (with or without recuperator) should not be higher than 730 RPM or 731 RPM (max) to ensure dry fluid flow into the turbine.

In contrast, the ORC fluid temperatures at condenser outlet (pump inlet) and pump outlet increased with higher ORC pump speed due to the constant heat sink parameters.

For the system with recuperator, a decline in the evaporator inlet temperature and an increase in the condenser inlet temperature were detected along with the increasing pump speed. However, for the system without recuperator, an exact opposite results was obtained. This illustrates that the recuperator cold side outlet (evaporator inlet) followed the same trend as the recuperator hot side inlet (turbine outlet), while the recuperator hot side outlet (condenser inlet) followed the same trend as recuperator cold side inlet (pump outlet). In addition, the decreases scope of the turbine inlet and outlet temperatures with higher pump speed when the system with recuperator is higher than the system without. The main reason is due to higher heat source temperature employed when the system with recuperator.

Quantitatively, when the ORC pump speed was increased from 630 RPM to 730 RPM in the system without recuperator, the temperatures of thermal oil outlet, turbine inlet, turbine outlet and condenser inlet decreased by 1.3K, 18.9K, 21.7K and 21.9K approximately. On the other hand, the ORC mass flow rate increased by 14.4% and the ORC temperatures at condenser outlet and pump outlet increased 2.3K and 2.5K each.

Similarly, when the speed of ORC pump was increased from 580 RPM to 731 RPM in the system with recuperator, the temperatures of thermal oil outlet, turbine inlet, turbine outlet and evaporator inlet decreased approximately by 7.10K, 34.79K, 48.60K and 21.94K. On the contrary, the ORC mass flow rate increased by 21.4% while the cycle

point temperatures of condenser inlet, condenser outlet and pump outlet increased by 3.48K, 0.49K and 0.76K respectively.

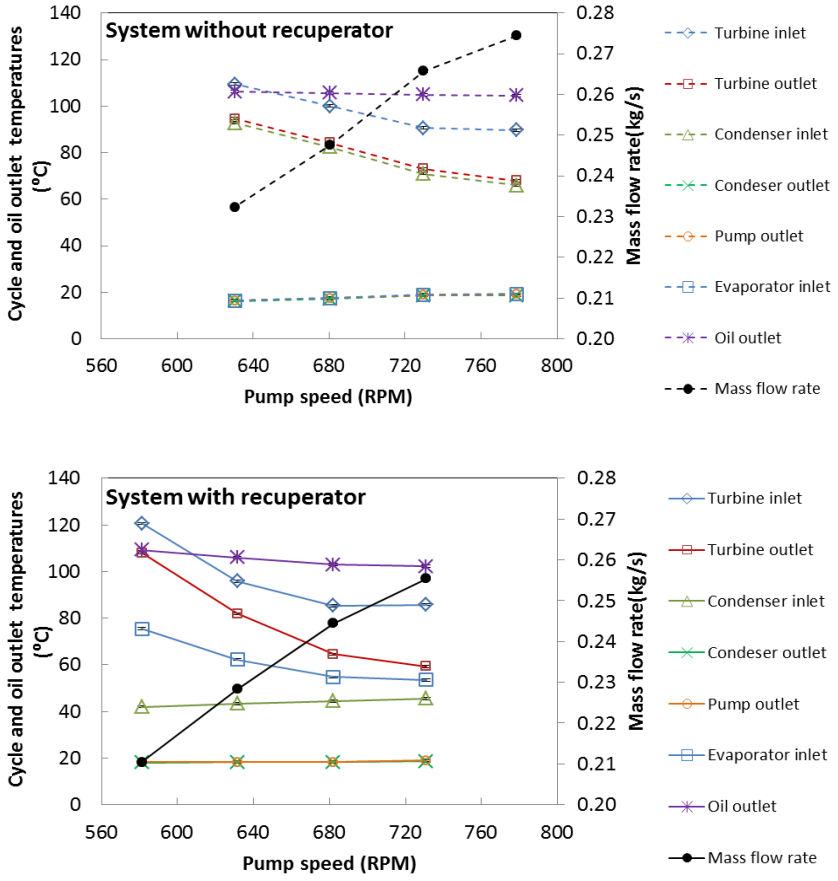

Figure 4.6 Variations of cycle point and thermal oil outlet temperatures and ORC mass flow rates with ORC pump speeds on system without and with recuperator

The effect of the increasing ORC pump speed on cycle point pressures for the system (without or with recuperator) is illustrated in Fig. 4.7. The effects on the pressure ratio of the turbine inlet and turbine outlet are also illustrated in the same figure.

Clearly, the cycle point pressures can be classified into two groups based on their pressure magnitudes, higher pressure group and low pressure group. The high pressure group includes the points at the ORC pump outlet, evaporator inlet and outlet, and turbine inlet while the low pressure group includes the points at turbine outlet, condenser inlet and outlet, and pump inlet. Both the pressure groups were considered for this particular test.

The pressure difference between two neighbour points in each group represented the pressure drop through the relevant pipe line or component. For the system in both the scenarios, the largest pressure drop in high pressure category occurred in fittings and along the connection pipes between evaporator out and turbine inlet (please refer Fig. 4.1 to view the schematic diagram of test rig). As expected, the ORC pump outlet pressure increased along with higher pump speed leading all other cycle point pressures to increase alongside, however at different rate.

For the low pressure category of the system without recuperator, the largest pressure drop occurred across the condenser. In contrast, the largest pressure drop for the system with recuperator occurred across the recuperator, between the turbine outlet and condenser inlet. This illustrates that when a recuperator is introduced in the system, a larger pressure drop and a higher pressure could be expected in the low pressure category as the pressure ratio of the turbine inlet and outlet could fall lower compared to the system without recuperator.

In percentage, when the ORC pump speed increased from 630 RPM to 730 RPM in the system without recuperator, the cycle point pressures of ORC pump outlet, evaporator inlet, evaporator outlet, turbine inlet, turbine outlet, condenser inlet, condenser outlet, and ORC pump inlet amplified 7.97%, 7.80%, 7.82%, 7.44%, 9.66%, 8.36%, 7.64% and 5.93% respectively. While, when ORC pump speed increased from 580 RPM to 731 RPM in the system with recuperator, the cycle point pressures of ORC pump outlet, evaporator inlet, evaporator outlet, turbine inlet, turbine outlet and condenser inlet and outlet amplified 10.68%, 5.69%, 5.64%, 4.62%, 12.61%, 10.40% and 4.69% respectively.

However, the pressure ratio of turbine inlet and outlet decreased with increasing ORC pump speed for both systems due to greater increase in turbine outlet pressure.

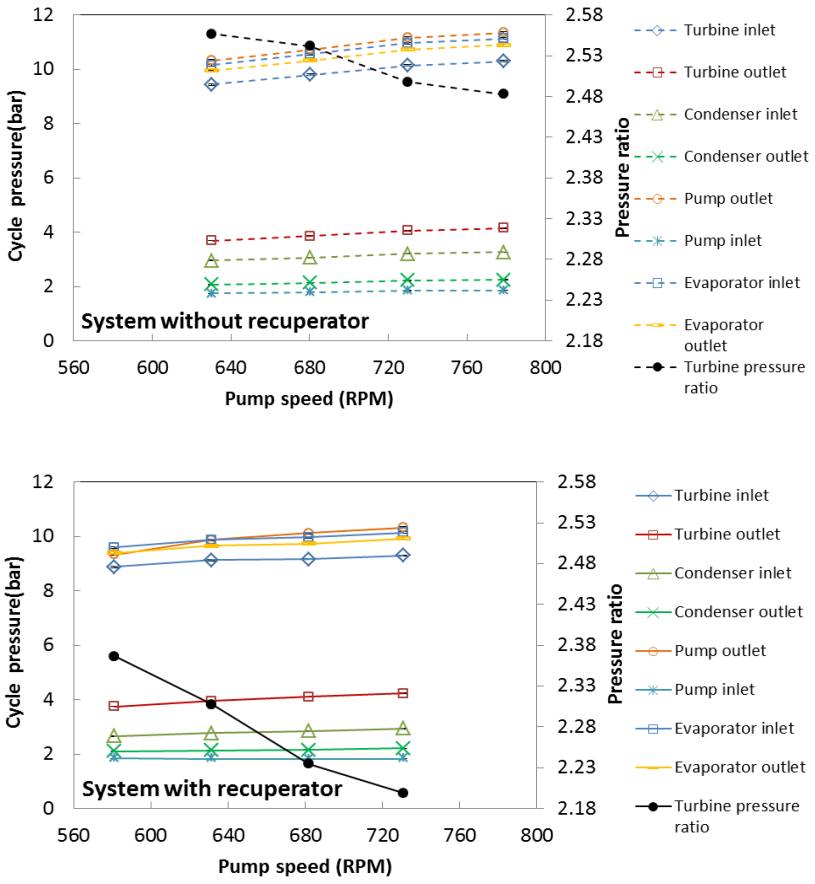

Figure 4.7 Variations of cycle point pressures and pressure ratios with ORC pump speeds on system with and without recuperator

The effects of increasing ORC pump speeds on the turbine and pump powers and on the evaporator and condenser capacities for the system (with and without recuperator) are presented in Fig. 4.8. The turbine power outputs were measured directly while other performance results were calculated based on the measurements of ORC temperature, pressure and flow rate related to each component.

As explained previously, the increased ORC pump speed would result in an increase in the ORC mass flow rate which escalated the heat transfers in the ORC heat exchangers including evaporator and condenser. Due to this reason, the evaporator heat input and condenser heat output increased along with the increasing ORC pump speed for the system in both scenarios.

When the system with recuperator was compared with the one without, the heat capacities of evaporator and condenser for system without recuperator were much

higher than for the system with. However for both the systems, more ORC pump power input was required with the increasing pump speed.

In addition, for the system with recuperator, the reduced fluid temperature at the turbine inlet and the reduced pressure ratio at turbine inlet and outlet as a result of increasing ORC pump speed caused the turbine power generation to decrease. In contrast, for the system without recuperator, the turbine power outlet increased along with the increasing pump speed. The rate of increase however was found to be less in comparison to other elements due to reduced pressure ratio at turbine inlet and outlet, and consequent turbine efficiency.

The results indicated that when the ORC speed was above 730RPM in the system without recuperator and 731 RPM in the system with recuperator, the ORC fluid at turbine inlet would be wet which would reduce the increase rates of those powers and capacities. This once again highlights the importance of ORC pump speed control in the ORC system.

Generally, when the ORC pump speed was increased from 630 RPM to 730 RPM in the system without recuperator, the turbine power output, evaporator heat input, condenser heat output and ORC pump power input increased by 4.92%, 1.66%, 3.18% and 24.49% respectively. While, when ORC pump speed was increased from 580 RPM to 721 RPM in system with recuperator, the evaporator heat input, condenser heat output and ORC pump power input increased by 6.36%, 8.82% and 37.81% respectively. However, the turbine power output decreased by 15.14%.

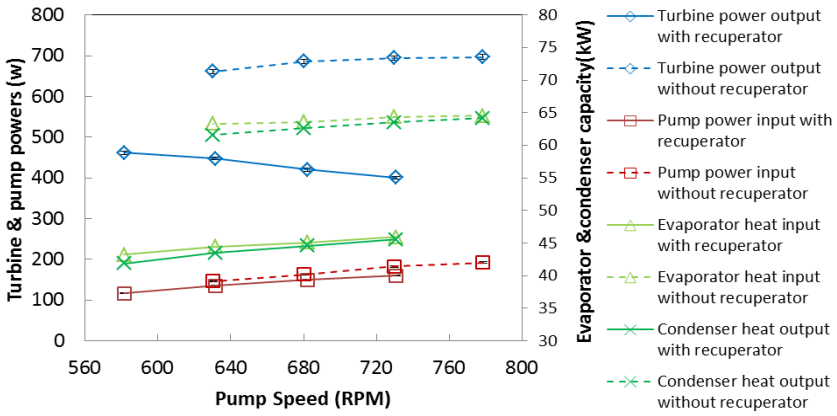

Figure 4.8 Variations of turbine and pump powers and evaporator and condenser capacities with ORC pump speeds on system with and without recuperator

The effects of varied ORC pump speeds on the turbine isentropic and overall efficiencies, and system thermal and overall efficiencies when without and with recuperator are presented in Fig. 4.9.

As shown in Fig.4.7, the pressure ratio of turbine inlet and outlet for both the systems decreased with higher ORC pump speed which could directly result in lower turbine isentropic efficiency with the increasing pump speed. However, the turbine overall efficiency increased with higher ORC pump speed in both the systems indicating an improved turbine electrical efficiency provided the mechanical efficiency remains constant.

For the system without recuperator, the turbine isentropic and overall efficiencies were higher due to higher pressure ratio of the turbine inlet and outlet. For both the systems, the system thermal and overall efficiencies decreased with higher pump speed, as shown in the figure below. In addition, the differences in the system overall efficiencies between both the systems increased with the increasing pump speed. This demonstrated that there was an optimal ORC pump speed for system with recuperator where the overall efficiency for the system with recuperator could be higher than the system without.

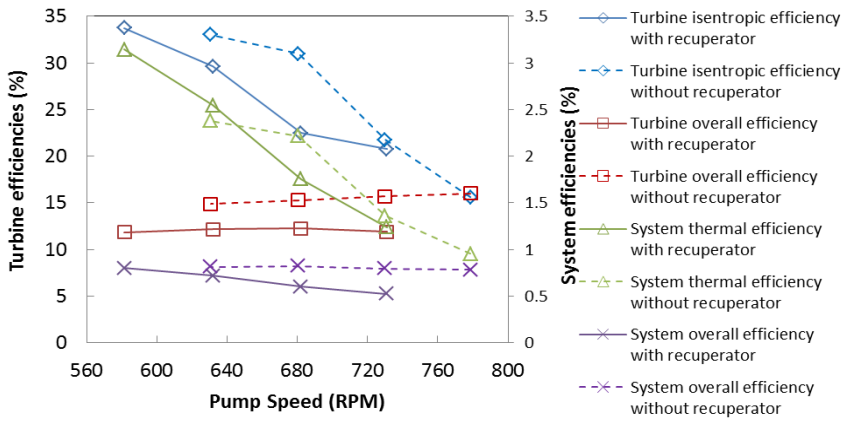

Figure 4.9 Variations of turbine and system efficiencies with ORC pump speeds on system with and without recuperator

4.3.3 The effect of the condenser fan speed swing

To examine the effect of condenser fan speed on the performance of ORC system, the ambient air (heat sink) flow velocity was varied from 1.5 m/s to 4.0 m/s while the fan speed was controlled form 40% to 100% (maximum rate). Meanwhile, as listed in Table 4.3, rest of other operating parameters were maintained at constant for the ORC system with recuperator.

Table 4.3 The operating conditions for R245fa ORC systems with recuperator of condenser fan speed swings

Recuperator of system In/ Out	Oil temperature ^{o}C	Oil flow rate Kg/s	R245fa pump speed RPM	Condenser air velocity m/s	Ambient air temperature ^{o}C
In	155.5	0.416	640	1.58~3.67	18.0

The variations of cycle point and thermal oil outlet temperatures with heat sink (ambient air) velocities in the system with recuperator are illustrated in Fig. 4.10. The measurements demonstrated that the condenser outlet and pump outlet all decreased with higher ambient air velocity. Meanwhile, as mentioned previously, the condenser inlet temperatures followed similar declination as pump outlet temperatures when the system was with recuperator. Therefore, the temperature of condenser inlet decreased with higher ambient air velocity as shown in the figure.

In addition, the measurements showed that the cycle point temperatures at turbine inlet and outlet and evaporator inlet increased with higher ambient air velocity while the thermal oil outlet temperatures were not much affected by the ambient air velocity considering the constant heat source parameters involved. This led the evaporator inlet temperatures to follow similar trend as the turbine outlet temperatures.

However, the R245fa mass flow rates decreased drastically with increasing ambient air velocity, which was resulted due to the changers in each cycle point density. Quantitatively, when the ambient air velocity increased from 1.58 m/s to 3.67 m/s for the system with recuperator, the temperatures of condenser inlet and outlet and pump outlet decreased about 3.04K, 4.56K and 4.60K respectively. On the contrary, the temperatures of turbine inlet and outlet and evaporator inlet increased about 8.95K, 9.26K and 3.18K respectively.

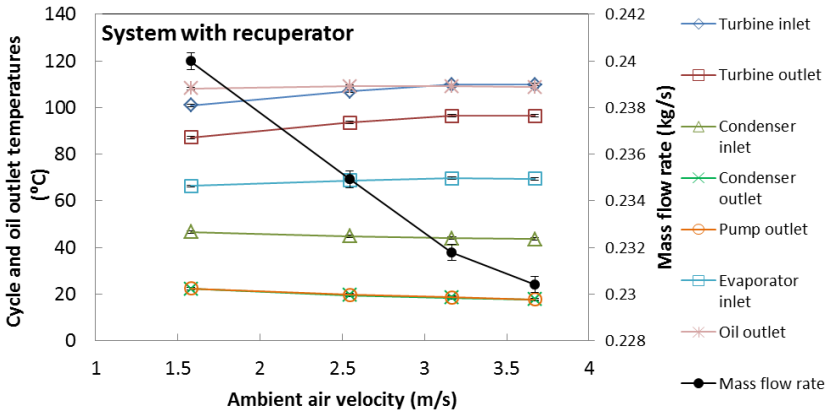

Figure 4.10 Variations of cycle point and thermal oil outlet temperatures with ambient air velocities on system with recuperator

The variations of cycle point pressures and pressure ratios of turbine inlet and outlet with ambient air velocities on system with recuperator are depicted in Fig. 4.11. It is seen from the figure that the working fluid pressures can be classified into two groups which are evaporating and condensing pressure sides. The evaporating pressure side includes the cycle locations at pump outlet, evaporator inlet and outlet and turbine inlet while the condensing pressure side includes the cycle locations at turbine outlet, condenser inlet and outlet and pump inlet.

The results from the test showed that both the evaporating and condensing pressure sides decreased with increasing ambient air velocities. This is mainly due to the high air flowrate increasing the overall heat transfer rate along the condenser air side, resulting in enhanced heat transfer performance. The temperature difference between the condensing and incoming ambient air flow is therefore reduced which led to lower condensing temperature and pressures at condensing pressure side.

The lower condensing pressure side (turbine outlet) also caused the working fluid pressure at evaporating pressure side (turbine inlet) to decrease considering of less fluid flow resistance through the turbine. However, the pressure reduction at the turbine inlet was relatively less than the decrease of outlet pressure such that the pressure ratio of turbine inlet and outlet increased with higher ambient air velocity. In percentage, when the ambient air velocity increased from 1.58 m/s to 3.67 m/s when the system was with recuperator, the cycle point pressures of ORC pump outlet, evaporator inlet, evaporator outlet, turbine inlet, turbine outlet, condenser inlet, condenser outlet, and ORC pump

inlet reduced by 1.91%, 1.96%, 1.95%, 1.72%, 6.52%, 8.74%, 14.54% and 17.74% respectively.

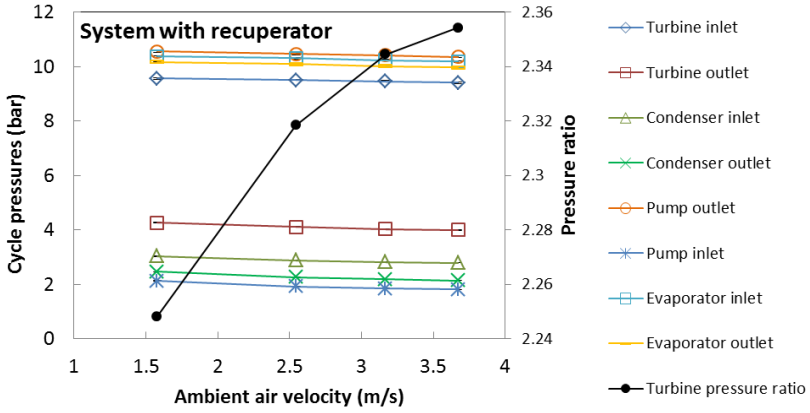

Figure 4.11 Variations of cycle point pressures and pressure ratios with ambient air velocities on system with recuperator

The effect of increasing ambient air velocity on turbine and pump powers, and evaporator and condenser capacities are shown in Fig. 4.12. As depicted in Fig. 4.11, the higher ambient air velocity increased the working fluid pressure ratio of turbine inlet and outlet and thus the turbine power generation. However, the pump power consumption and evaporator heat input did not change much with higher ambient air velocity due the constant ORC pump speed and heat source parameters during the test.

In addition, as shown in Fig. 4.10, the condenser inlet and outlet temperatures also decreased with higher ambient air velocity. Similarly, the mass flow rate of the working fluid also decreased significantly with higher ambient air velocity such that the condenser heat output decreased in contrast. In percentage, when the ambient air velocity was increased from 1.58 m/s to 3.67 m/s for the system with recuperator, the turbine power generation increased by 7.41%.

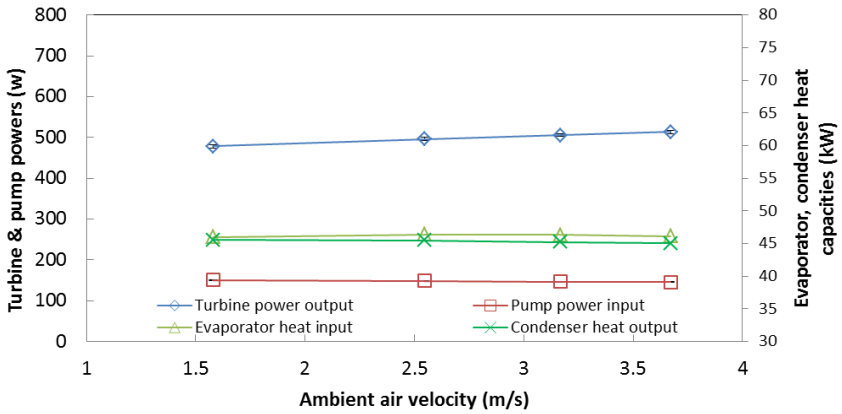

Figure 4.12 Variations of turbine and pump powers and evaporator and condenser capacities with ambient air velocities on system with recuperator

The effects of increasing ambient air velocity on the turbine isentropic and overall efficiencies, and system thermal and overall efficiencies are illustrated in Fig. 4.13. As explained previously, the pressure ratio of turbine inlet and outlet increased with higher ambient air velocity leading to higher efficiency for all the selected parameters. In percentage, when the ambient air velocity increased from 1.58 m/s to 3.67 m/s for the system with recuperator, the turbine isentropic and overall efficiencies, and system thermal and overall efficiencies increased by 3.13%, 1.22%, 26.86% and 12.05% respectively.

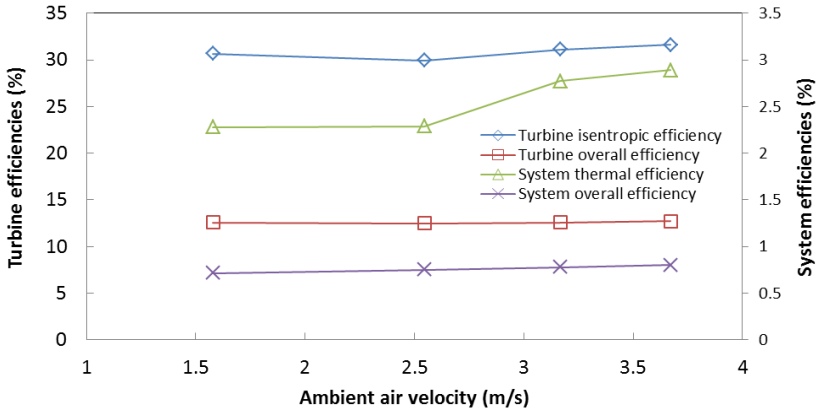

Figure 4.13 Variations of turbine and system efficiencies with ambient air velocities on system with recuperator

4.4 Control Strategies

The turbine inlet superheat temperature and pressure are two important control parameters in an ORC system (with or without recuperator). Considering these two parameters can help adjust the turbine temperature and pressure to maximum limitation along with controlling the conditions of dry turbine inlet.

As explained in section 4.3.1, the heat source temperatures can have major effects on both the turbine inlet temperature and pressure. The superheat at the turbine inlet is defined as the temperature difference between the turbine inlet temperature and equivalent saturated vapour temperature based on turbine inlet pressure. The effect of increasing heat source temperature on ORC fluid superheat temperature for the system (both when with and without recuperator) is illustrated in Fig. 4.14.

According to the test results, in order to get same superheat temperature at the turbine inlet, the heat source temperatures for the system with recuperator need to have much higher temperature than for the system without. In addition, the results show a linear increase in heat source temperature along with increasing ORC fluid superheat temperature (for both the systems). The correlation between the two parameters can be denoted by the equations below:

$$T_s = 0.4711\Delta T_{sh,T} + 144.87, \quad for\ system\ without\ recuperartor \tag{4.7}$$

$$T_s = 0.6153\Delta T_{sh,T} + 155.09, \quad for\ system\ with\ recuperartor \tag{4.8}$$

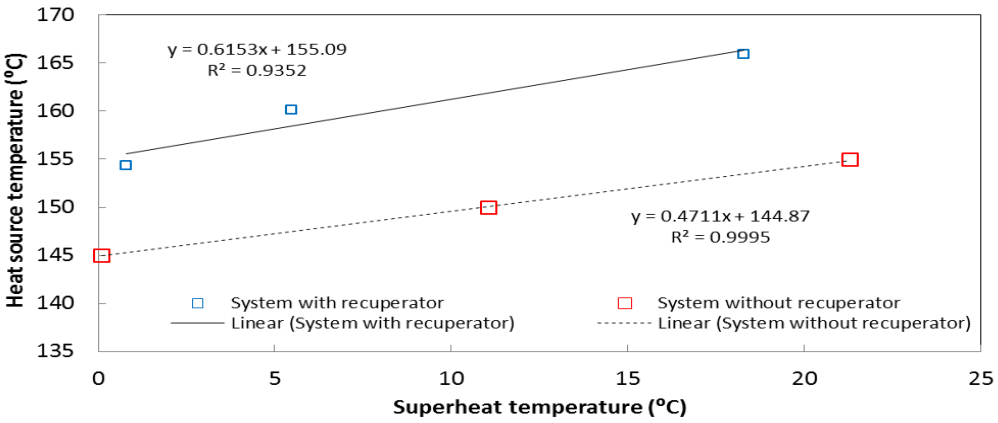

Figure 4.14 Relations between heat source temperatures and ORC fluid superheats at turbine inlet on system with and without recuperator

As explained in Section 4.3.2, the ORC fluid pressure at turbine inlet is strongly affected by the ORC fluid pump speed such that the control function between these two parameters can be constructed for both systems. As depicted in Fig. 4.15, the ORC pump speed for both systems should increase near linearly if higher ORC fluid pressure at turbine inlet is required which can be correlated as the following equations:

$$R_P = 141.45P_{T,in} - 705.59, \quad for\ system\ without\ recuperartor \tag{4.9}$$

$$R_P = 363.22P_{T,in} - 2646.7, \quad for\ system\ with\ recuperartor \tag{4.10}$$

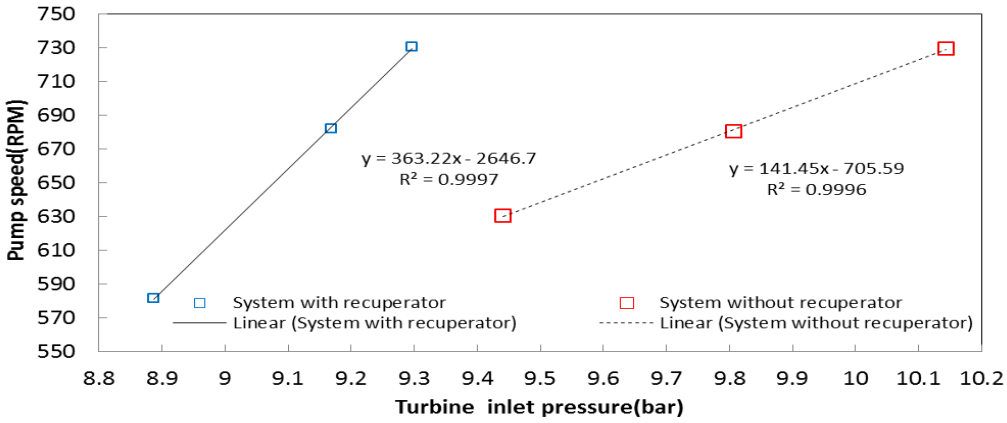

Figure 4.15 Relations between ORC pump speeds and ORC turbine pressures on system with and without recuperator

In practice, these four functions listed in Equations 4.7, 4.8, 4.9 and 4.10 can be used to control the ORC fluid superheat temperature and pressure at turbine inlet for the system in both the scenarios. For the superheat control, two sensing parameters of ORC fluid temperature and pressure at turbine inlet are required to modulate the heat source temperature. Meanwhile, only one sensing parameter of ORC fluid pressure at turbine inlet is required to modulate the pump speed.

As discussed in section 4.3.3, the ambient air velocity can have a significant effect in the ORC working fluid pressure at turbine outlet for the system with recuperator. Fig. 4.16 illustrates the results for ambient air velocity with decreasing turbine outlet pressure. As shown, the ambient air velocity increases almost linearly with lower ORC fluid pressure at turbine outlet. This relationship can be correlated with the equation below:

$$V_A = -6.934 P_{T,out} + 31.077, \quad for\ system\ with\ recuperartor \tag{4.11}$$

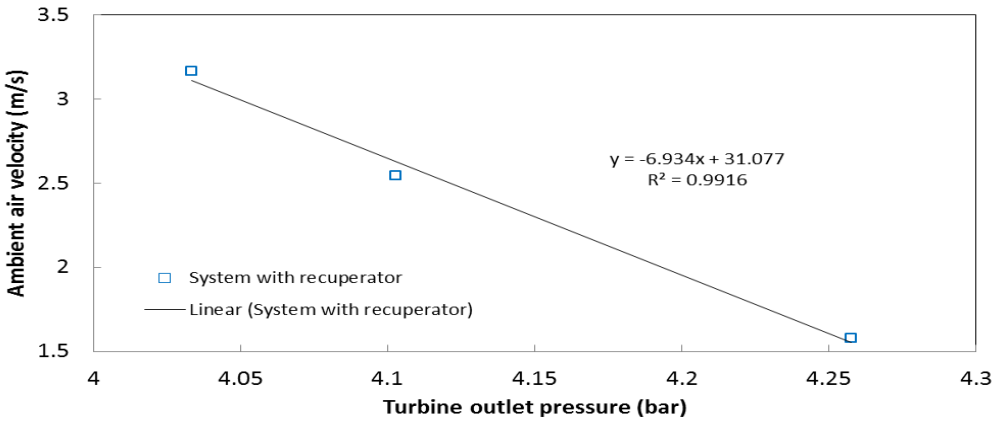

Figure 4.16 Relations between ambient air velocities and condenser outlet temperatures on system with recuperator

4.5 Summary

This chapter initially provided a briefly review on the test facility of the R245fa ORC systems with turboexpander and plate-type evaporator. The next part of the chapter provides a thorough discussion on the results for three different experiments conducted in the system. Each test involved the effect of varying each important operating parameter in the system's overall performance. The three important parameters included heat source temperature, ORC pump speed, and ambient air velocity of air cooled condenser. It was found that at a fixed working fluid speed and constant heat sink parameters, the performances of both the recuperative and basic ORC systems could be enhanced with increased heat source temperatures. However, due to the maximum working fluid temperature limitation at the turbine inlet, the heat source flow rates couldn't be maintained constant for both systems such that the temperature ranges were also varied. These led to less efficiency for the system with recuperator at those specific test conditions. The pressure drop from the recuperator had also contributed to the decrease of system efficiency. On the other hand, at a constant heat source and sink parameters, the higher R245fa pump speed could further reduce the thermal efficiency of both systems. The discussion part also provides a detailed comparison on the effects of changing the parameters in the system with recuperator and without recuperator.

Chapter 5 will present experimental test results for the R245fa ORC systems with scroll expander and different kind evaporators.

Chapter 5 – EXPERIMENTAL RESULTS AND DISCUSSION USING R245fa ORGANIC RANKINE CYCLES WITH SCROLL EXPANDER

This chapter provides a brief overview of the as-built test facility and discusses the experimental test results of scroll expander integrated into a prototype of ORC system with R245fa as the working fluid. The experimental investigation discussed in this chapter only focuses on the experimental characterizations of the scroll expander and different kind of evaporators and not the ORC system as a whole (please refer Chapter 3 for description of individual system components and experimental set-up).

5.1 Overview of the As-built Test Facility and Test Conditions

A schematic diagram of the small-scale R245fa ORC test rig is presented in Fig. 5.1. The system consisted of two operational loops: ORC and heat source. The ORC loop comprised of two oil heated evaporators connected in parallel (shell and tube evaporator and plate-type evaporator), a R245fa scroll expander and squirrel cage generator, plate-type recuperator, finned-tube air cooled condenser, liquid receiver, liquid pump, and other ancillary equipments. The shell and tube evaporator and plate-type evaporator are same size, which is 54.8kW. Both of them are selected by the thermodynamic analysis, which is shown in Chapter 8.

In order to examine the integration effects of two evaporators in the ORC system, two-way valves were installed on both heat source and ORC sides of evaporators and both sides of the recuperator. In order to operate the appropriate operational conditions and stationary conditions, a specific test condition was specified for each of the four experiments: the system with shell and tube evaporator when with recuperator, the system with shell and tube evaporator when without recuperator, the system with plate-type evaporator when with recuperator, and the system with plate-type evaporator when without recuperator.

Once the test rig was setup, experimental investigation could be carried out to evaluate and compare the system performance at different structural layouts and operating conditions. In total, a series of 32 performance points were achieved for the system running with or without recuperator and different evaporators. Each steady state point

was recorded at a time interval of at least 30 min, with sample period of 1 second. There were 1800 direct measurements for each steady state in total. The final measured data of each instrument device was worked out by averaging the 1200 direct measurements collected for the time period of last 20 minutes for each 30 minutes.

The thermal oil temperature was varied from 159 ^{o}C to 185 ^{o}C by modulating the CHP system power outputs while the ORC working fluid mass flow rate was varied from 0.121 kg/s to 0.142 kg/s by changing the ORC pump motor frequencies. Being able to control both the parameters ensured the scroll expander inlet pressure and temperature were within their maximum limitations during the experiment. The maximum pressure was set at 13.8bar and temperature at 160 ^{o}C by the scroll expander manufacturer. The rotation speed of the scroll expander and air velocity of the air-cooled condenser were kept constant at 1620 RPM and 3.67 m/s for all experiments. Further details on the range of operating parameters for scroll expander, plate-type evaporator, and shell and tube evaporator are summarised in following Section 5.3.

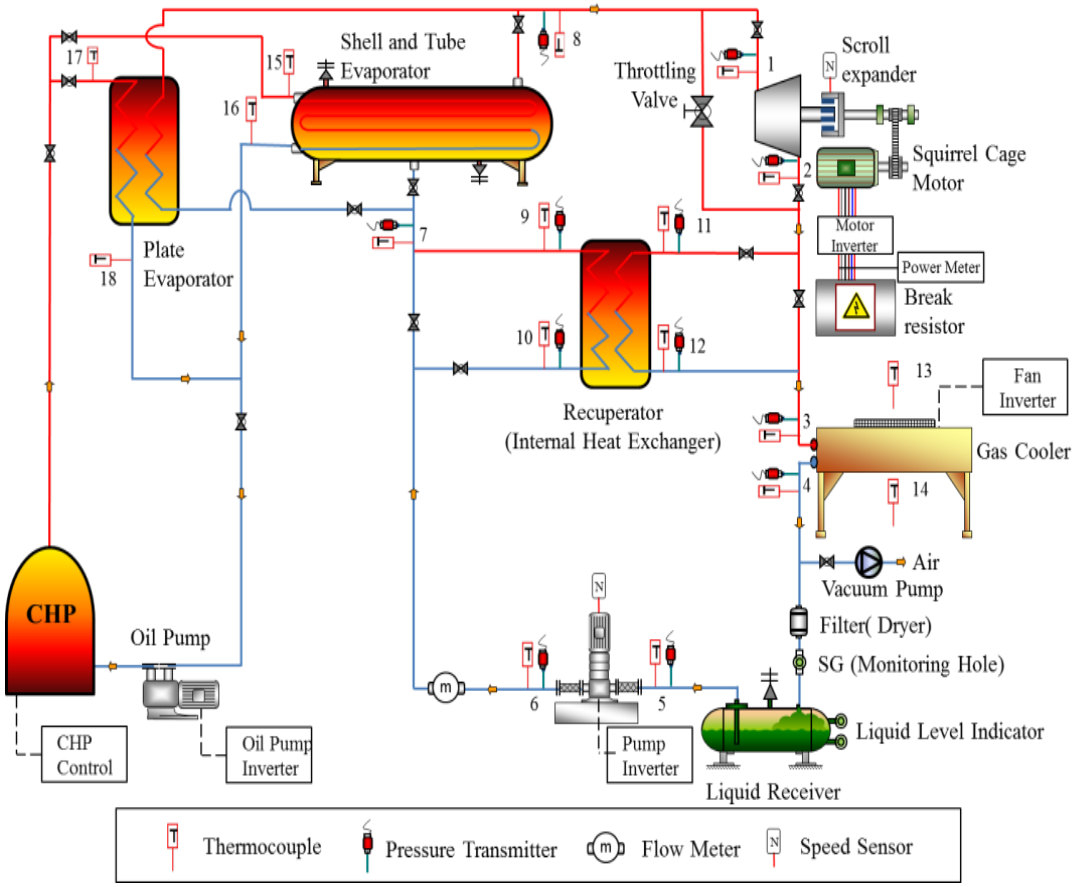

Figure 5.1 Schematic representation of an ORC test rig with scroll expander

5.2 Experimental Data Collection and Processing

Parameters for temperatures, pressures, and fluid mass flow rates for both sides of the ORC working fluid (R245fa) and heat source (thermal oil) were measured and recorded by the data logger system at each steady state. In addition, the power generation from the scroll expander and power input from the R245fa liquid pump were also measured. The scroll expander power outputs were measured directly using a power meter installed at outlet electric wire of the power generator in both conditions. Detailed description on the instrumentations and data logging system is presented in Section 3.5 (Chapter 3).

All the thermophysical properties of R245fa such as enthalpy and entropy etc. were calculated using REFPROP 8.0 software (Lemmon et al., 2007) based on the average measured temperature and pressure at each measured point.

5.2.1 Overall efficiency of scroll expander

For the system with shell and tube evaporator or plate-type evaporator, the expander overall efficiency $\eta_{exp,all}$ is calculated in Equation 5.1 which is ratio of measured power generation and power generation of isentropic expander process. The overall efficiency can take account of the expander's isentropic, mechanical and electrical efficiencies.

$$\eta_{exp,all} = \frac{\dot{W}_{exp}}{\dot{m}_f(h_1 - h_{2,is})} \tag{5.1}$$

where $\dot{W}_{exp}$ is the measured scroll expander electrical power output, as described in Section 3.5.

5.2.2 ORC system overall efficiency and the evaporator heat capacity

The system overall efficiency ($\eta_{s,all}$) is defined as the system net power generation over the heating input through the evaporator and calculated in Equation 5.3. The power consumption of the ORC pump (W_P) can be calculated using Equation 4.4 (please refer Chapter 4 for further details).

$$\eta_{s,all} = \frac{\dot{W}_{exp} - \dot{W}_P}{\dot{m}_f(h_8 - h_7)} \tag{5.3}$$

Due to two different type evaporators used into the ORC system, as shown in Equation 5.3, the evaporator heat capacity is a key impact factor for the system overall efficiency which is defined by the scroll expander power as well. Thus, the heat capacity of each evaporator was calculated separately using the equation specified below:

$$Q_{evp} = \dot{m}_f(h_8 - h_7) \tag{5.4}$$

5.2.3 Temperature difference of the evaporator

The temperature difference of the evaporator can be defined as the temperature difference of the thermal oil inlet and the evaporator ORC fluid outlet, as shown in Equation 5.5 and 5.6.

$$\Delta T_{evp} = T_{15} - T_8 \tag{5.5}$$

for the system with shell and tube evaporator

$$\Delta T_{evp} = T_{17} - T_8 \tag{5.6}$$

for the system with plate-type evaporator

5.2.4 Temperature transfer efficiency of the evaporator

In this study, both the evaporators were single heat exchangers. Comparing the temperature transfer efficiency of each evaporator is a good method of comparing the performance of both evaporators, especially since the efficiency takes into account the parameters of thermal oil and ORC fluid sides. The temperature transfer efficiency of the evaporator can be calculated using Equation 5.7 and Equation 5.8.

$$\mu_{evp} = \frac{T_8 - T_7}{T_{15} - T_7} \tag{5.7}$$

for the system with shell and tube evaporator

$$\mu_{evp} = \frac{T_8 - T_7}{T_{17} - T_7} \tag{5.8}$$

for the system with plate-type evaporator

5.2.5 Uncertainty in calculation

Considering the uncertainty of the measured variables, which include heat source temperatures and R245fa temperatures, an error margin was found for each variable. Thus, the uncertainty in the calculation of temperature transfer efficiency of evaporator was found to be ±0.91%. Detailed explanation of the uncertainty analysis is given in Append D.

5.3 Test Results

5.3.1 Performances of the scroll expander

In order to examine the performance of the scroll expander at different pressure ratios, a series of tests were carried out for the system with either shell and tube evaporator or plate evaporator, with or without the recuperator. As listed in Table 5.1, the measured parameters for the expander include the variations of temperatures and pressures at the expander inlet and outlet, ORC fluid mass flow rates, expander power generations and pump power consumptions. The pressure ratio is also calculated and listed in the table. It is seen from the table that the ORC fluid flow rates and expander outlet pressures were all mostly higher for the test system with shell and tube evaporator than those with plate evaporator but the pressure ratios are relatively lower. Consequently, the power generations for the system with plate evaporator were relatively higher than those of system with shell and tube evaporator. Although it is not clear which evaporator matched well in the system, the system test results with different component combinations can provide extensive data to evaluate the expander and system performances.

Table 5.1 Ranges of the main measured variables for scroll expander

Evaporator Type	Recuperator	Range	$P_{ex,in}$ (bar)	$P_{ex,out}$ (bar)	Pressure ratio	$T_{ex,in}$ °C	$\dot{M}$ (kg/s)	$T_{ex,out}$ (°C)	$\dot{W}_{el}$ (W)	$\dot{W}_p$ (W)
Shell and tube	with	Min	10.01	4.34	2.31	93.93	0.1278	68.99	689.93	67.69
		Max	11.6	4.49	2.58	120	0.1416	96.23	1195.12	95.32
	without	Min	8.73	4.03	2.17	87.07	0.1328	57.02	395.05	62.67
		Max	9.64	4.06	2.37	93.42	0.1354	69.57	802.43	73.85
Plate-type	with	Min	7.02	3.12	2.25	77.22	0.1224	48.74	288.16	52.24
		Max	10.58	3.25	3.26	157.38	0.1275	124.94	1556.42	92.96
	without	Min	9.48	3.11	3.05	109.95	0.1207	81.85	1174.79	78.36
		Max	10.45	3.25	3.22	156.71	0.1251	122.85	1443.78	87.36

From the test results, the variations of expander power generation and pump power consumption with expander pressure ratios are depicted in Fig. 5.2. It is seen that the expander power generation increases polynomially with higher expander pressure ratio which could be correlated as indicated in the diagram. On the other hand, the pump power consumption increases linearly with higher expander pressure ratio. Additionally, the system with plate evaporator presents the test results with the whole range of pressure ratios while only smaller pressure ratios are covered by the test results of system with shell and tube evaporator. When the pressure ratios are within the lower range, at a constant pressure ratio, the expander power generation and pump power consumption are both relatively higher for the system with shell and tube evaporator.

Maximum electrical power outputs of 1556.24W and 1195.12W of the scroll expander were observed at pressure ratio points of 3.3 and 2.6 for the system with plate-type evaporator and shell and tube evaporator respectively. The relation between scroll expander outlet and pressure ratio across the scroll expander can be correlated using the following equation:

$$W_{exp} = -457.49{PR_{exp}}^2 + 3340.4PR_{exp} - 4582.9 \quad (5.9)$$

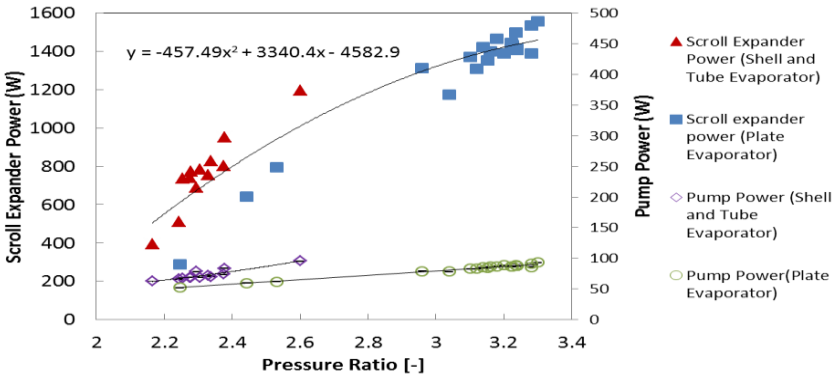

Figure 5.2 Variations of scroll expander and pump powers with expander pressure ratio for the system with various evaporator and with and without recuperator

Subsequently, the variations of expander overall efficiency with pressure ratio are calculated and plotted in Fig. 5.3. Similar to that of expander power generation, when the pressure ratio is less than 3, the overall efficiency increases polynomially with higher pressure ratio and decreases with the pressure ratio if the pressure ratio increases further. Therefore, the maximum expander overall efficiency is found to be 0.47 when the pressure ratio is around 3. Again the relation between the overall efficiency and pressure ratio can be correlated and indicated in the same diagram. The relation between scroll expander overall efficiency and pressure ratio can be correlated using the following equation:

$$\eta_{exp,all} = -0.3715 {PR_{exp}}^2 + 2.1721 PR_{exp} - 2.7162 \quad (5.10)$$

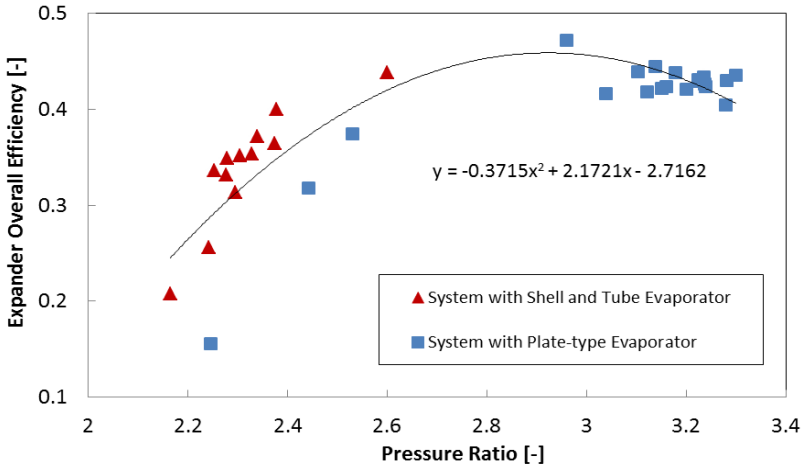

Figure 5.3 Variations of scroll expander overall efficiency with expander pressure ratio for the system with various evaporator and with and without recuperator

To evaluate and compare the effect of recuperator installation on the system performance, the variations of system overall efficiency with expander pressure ratios for the system with different evaporators, with or without recuperator are demonstrated in Fig. 5.4.

As seen in Fig. 5.4, the system overall efficiency also increases polynomially with higher expander pressure ratio no matter what the system structures are. However, the system with shell and tube evaporator can only operate in a lower range of pressure ratios while the system with plate evaporator is able to work in a larger range of pressure ratios. Consequently, the system overall efficiency is higher when the plate evaporator is utilized. On the other hand, the system overall efficiency can be greatly improved when a recuperator is applied due to the reduction of heat input to the ORC system. It is also noted that the maximum overall efficiency of the system with plate-type evaporator is 5.09 when with recuperator and 3.59 when without. The maximum overall efficiency of the system with shell and tube evaporator is 3.91 when with recuperator and 2.15 when without.

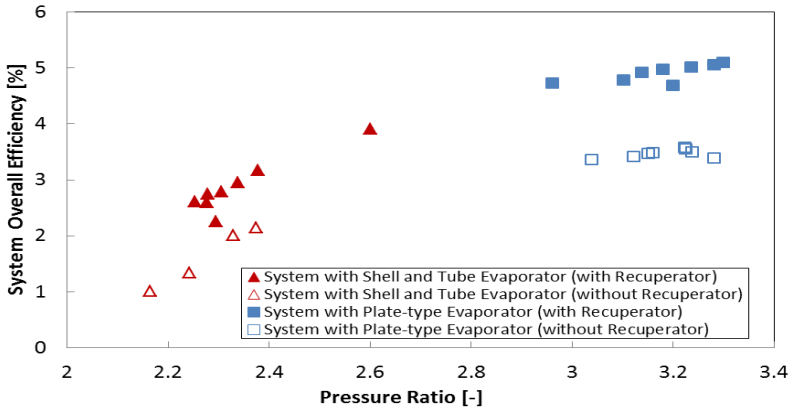

Figure 5.4 Variations of system overall efficiency with expander pressure ratio for the system with various evaporators and with and without recuperator

The effect of recuperator on the evaporator heat capacity can be further demonstrated in Fig. 5.5. Again, the system with plate evaporator can operate in larger pressure ratio range while the system with shell and tube evaporator works in lower pressure ratio range. At all circumstances, the evaporator heat capacity increases with higher expander pressure ratio. Notably, the integration of recuperator can greatly reduce the required evaporator heat capacity irrespective of evaporator type employed in the system. This will then lead to higher system overall efficiency as shown in Fig. 5.4.

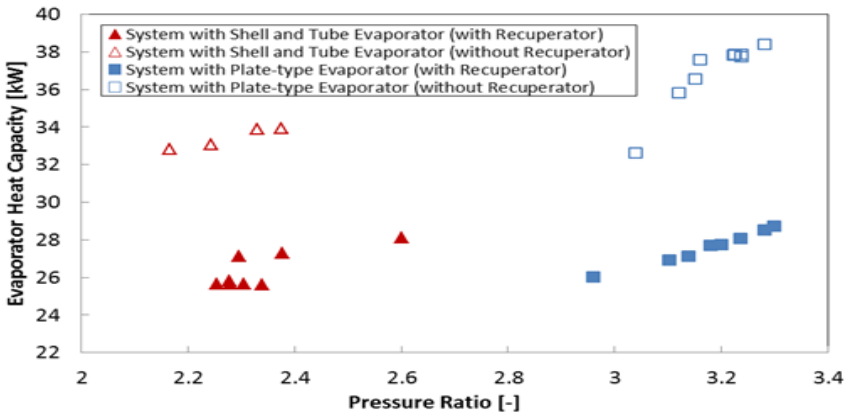

Figure 5.5 Variations of evaporator capacity with expander pressure ratio for the system with various evaporators and with and without recuperator

Similarly, Fig. 5.6 presents the results of the scroll expander power generation and the system overall efficiency at different evaporator heat capacities and with and without

recuperator. It is noted that the scroll expander power generation and system overall efficiency both increase with higher evaporator heat capacity irrespective of the system components. However, the system with recuperator can operate at a lower required evaporator heat capacity while both expander power generation and system overall efficiency are higher when plate evaporator is employed. The measurements can also illustrate that the integration of recuperator can greatly improve the ORC system performance in terms of power generation, system overall efficiency an evaporator heat capacity required.

Quantitatively, a maximum scroll expander power generation of 1556.24W was observed for system with plate-type evaporator at heat capacity of 28.72kW when with recuperator, and 1443.78W at 37.85kW when without. Similarly, a maximum value of 1195.12W scroll expander power generation was observed for the system with shell and tube evaporator at heat capacity 28.1kW when with recuperator, and 802.43W at 33.93 kW when without. In addition, almost 5.09% (with recuperator) and 3.59% (without recuperator) of the system overall efficiency are achieved using plate-type evaporator, compared to the maximum of about 3.91% (with recuperator) and 2.15% (without recuperator) obtained when using shell and tube evaporator.

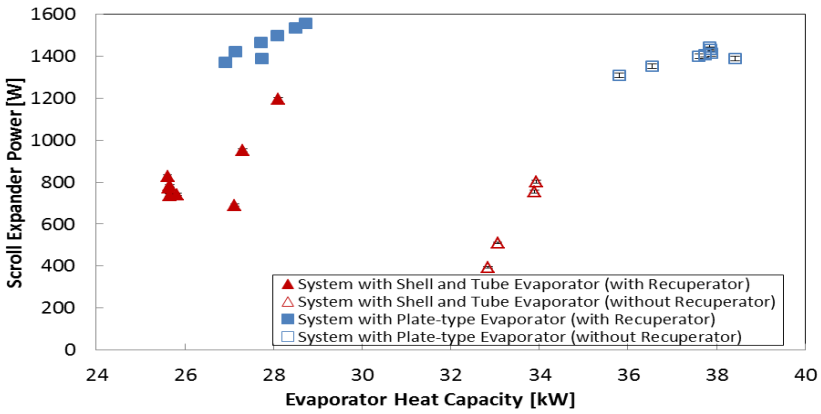

(a)

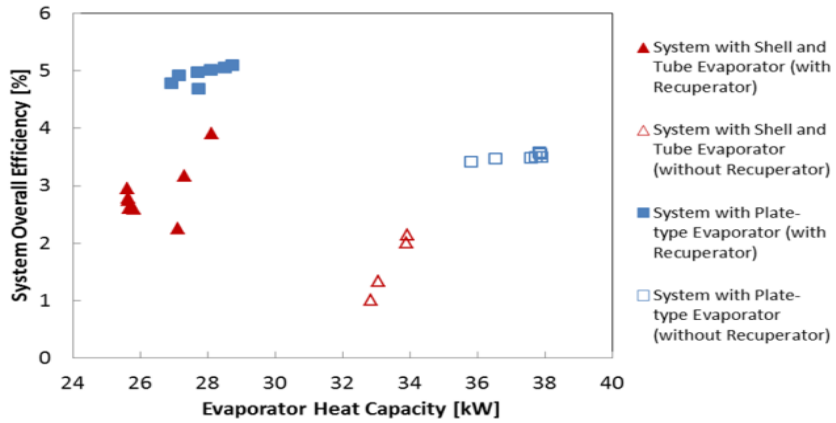

(b)

Figure 5.6 Variations of scroll expander power (a) and system overall efficiency (b) with different evaporator heat capacities and with and without recuperator

5.3.2 Performances of plate-type evaporator and shell and tube evaporator

As shown in Fig. 5.1, two oil-heated evaporators (shell and tube evaporator and plate-type evaporator) were installed before the scroll expander. The thermal oil temperature of the evaporator oil side was controlled by modulating the CHP power output. In addition, the ORC pump speed could be controlled to modulate the mass flow rate of ORC fluid through the evaporators and pressure in the evaporators. To examine the performance of the plate-type evaporator and shell and tube evaporator when integrated in the ORC system, a series of parametric range, as illustrated in Table 5.2, were selected for the experiment. As seen in the Table, the ORC system was integrated with the shell and tube evaporator or plate-type evaporator for both scenarios, with and without recuperator.

Table 5.2 Ranges of the main measured variables for evaporators

Evaporator Type	Recuperator		Oil Side Variables		ORC Fluid Side Variables		
			$T_{oil,in}$ °C	$T_{oil,out}$ °C	$T_{evp,in}$ °C	$T_{evp,out}$ °C	$\dot{M}$ kg/s
Shell and tube	with	Min	168.84	139.32	60.95	94.47	0.1278
		Max	180.06	149.45	75.50	120.86	0.1416
	without	Min	168.73	135.26	15.08	87.78	0.1328
		Max	179.42	142.70	15.95	93.45	0.1354
Plate-type	with	Min	173.11	106.76	76.02	135.66	0.1234
		Max	177.75	122.21	87.12	158.60	0.1275
	without	Min	159.91	102.89	17.32	133.70	0.1233
		Max	168.56	112.18	23.19	146.57	0.1251

The temperature differences in the evaporator as a result of the increasing heat source temperature for the system with each evaporator (shell and tube, and plate-type) when with and without recuperator are illustrated in Fig. 5.7

For all scenarios, the temperature difference of the evaporator increases slightly with higher heat source temperature. The values are also affected by the mass flow rates of evaporator oil side and ORC fluid side. The temperature difference of shell and tube evaporator is much higher when compared with plate-type evaporator, both when with or without recuperator.

For the same range of heat source temperature of shell and tube evaporator, the temperature different when with recuperator is lower than when without. This is mainly due to higher ORC fluid inlet temperature in the evaporator of the system with recuperator. However, for the system with plate-type evaporator, the evaporator temperature difference of the system when with and without recuperator are within similar range due to lower heat source temperature in the system without recuperator.

A minimum temperature difference of 16.28 °C was achieved for the system with plate-type evaporator at heat source temperature of 161.37 °C when without recuperator, and 15.48 °C at 174.09 °C when with. Similarly, a minimum temperature difference of 80.95 °C was achieved for the system with shell and tube evaporator at heat source temperature 168.73 °C when without recuperator, and 52.85 °C at 173.71 °C when with.

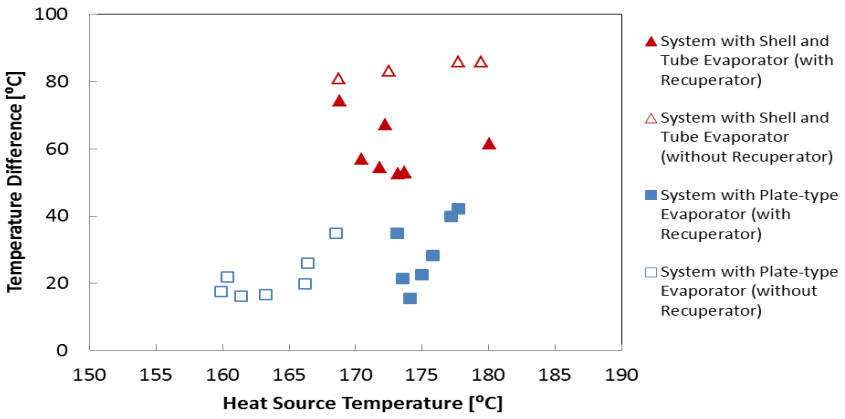

Figure 5.7 Variations of temperature difference of the evaporator with heat source temperature in the system with shell and tube evaporator and plate-type evaporator and different recuperator situations

The variations in evaporator temperature transfer efficiency with heat source temperature for both evaporators and different recuperator situations are illustrated in Fig. 5.8. The temperature transfer efficiency of plate-type evaporator is much higher than the shell and tube evaporator for the system (with and without recuperator) due to the lower temperature difference of plate-type evaporator. In addition, the temperature transfer efficiency of both evaporators in the system without recuperator is slightly higher than the system with recuperator in most of tests due to the lower ORC fluid inlet temperature of the evaporator when without recuperator.

A maximum temperature transfer efficiency of 0.88 was observed for the system with plate-type evaporator at heat source temperature of 161.37 ^{o}C when without recuperator, and 0.82 at 174.09 ^{o}C when with. Similarly, a maximum temperature transfer efficiency of 0.48 was observed for the system with shell and tube evaporator at heat source temperature of 179.42 ^{o}C when without recuperator, and 0.47 at 172.51 ^{o}C when with recuperator.

For the plate-type evaporator, the minimum evaporator temperature difference and maximum evaporator temperature transfer efficiency are located at same heat source temperature. However, for the shell and tube evaporator, the heat source temperature locations for both values are slightly difference, due to the changes in ORC fluid inlet temperature as a result of different ORC mass flow rate and allowed range of measurements errors.

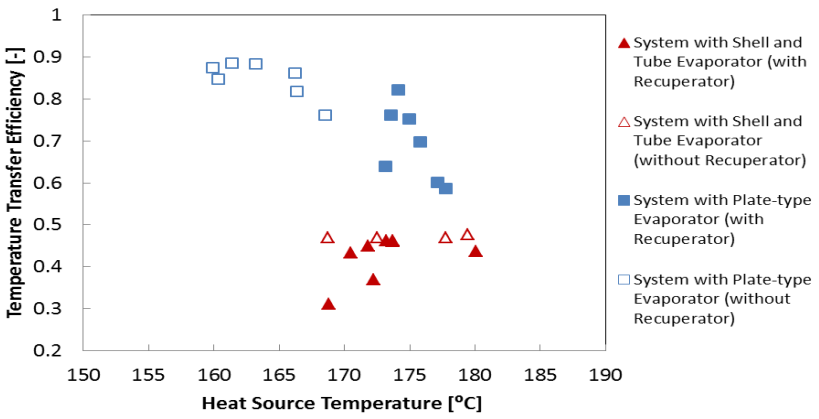

Figure 5.8 Variations of temperature transfer efficiency of the evaporator with heat source temperature in the system with shell and tube evaporator and plate-type evaporator and different recuperator situations

In order to further evaluate the performance of evaporator when integrated into the ORC system, the heat capacity of the evaporator at different heat source temperature in the system (with and without recuperator) with both evaporators were calculated, as illustrated in Fig. 5.9. As stated before, the heat capacity of evaporator in the system without recuperator is higher than the system with recuperator due to low ORC fluid inlet temperature of the evaporator when without recuperator. However, the heat capacities itself were not much affected by the higher heat source temperature due to changes in ORC mass flow rate.

A maximum plate-type evaporator heat capacity of 37.89kW was obtained for heat source temperature 159.91 ^{o}C when without recuperator, and 28.72kW for 173.54 ^{o}C when with. Likewise, a maximum shell and tube evaporator hear capacity of 33.93kW was obtained for heat source temperature 179.42 ^{o}C when without recuperator, and 28.1kW for 180.06 ^{o}C when with.

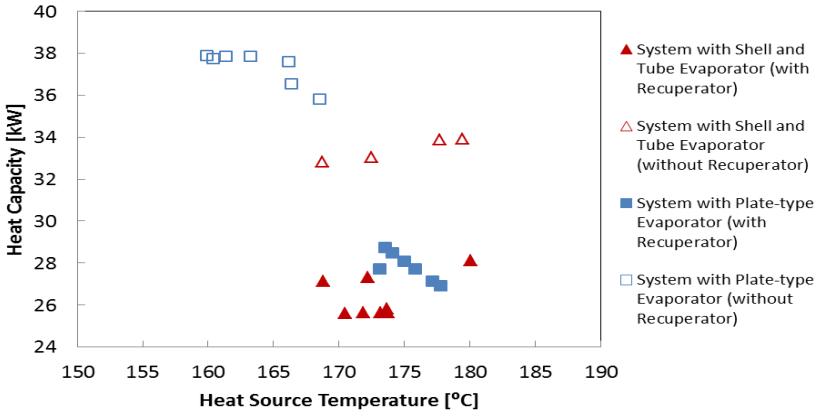

Figure 5.9 Variations of heat capacity of the evaporator with heat source temperature in the system with shell and tube evaporator and plate-type evaporator and different recuperator situations

In order to analyse the performance of different types of evaporator when integrated into an ORC system, temperature vs. heat transfer (TQ) diagram is usually a good measure for understanding the internal process of heat exchanger. The TQ diagram for R245fa with the evaporating pressure of 13.15bar for the shell and tube evaporator is presented in Fig. 5.10 (a) and the diagram for R245fa with the evaporating pressure of 11.67bar for the plate-type evaporator is presented in Fig. 5.10 (b) (for the system with recuperator). In these diagrams, the data for thermal oil and R245fa, and the pinch point are shown. The pinch point is an important working parameter for determining the heat transfer of heat exchangers; it can be employed to improve the heat fitting between the heat source and the working fluid of the ORC system. Thus, it can strongly affect the performances of ORC systems. In addition, the pinch point position of the evaporator is quite important for the ORC system performance. The pinch point position of the evaporator is usually sited at the working fluid bubble point. If the wrong pinch point position of the evaporator is used, a decrease for the cycle performance could be achieved (Pan et al., 2012).

The evaporator TQ diagrams are based on the measured inlet and outlet temperatures of the evaporator oil side and ORC fluid side corresponding to the measured evaporator ORC fluid outlet pressure. And for the heat transfer rate of the oil side, it is calculated by the energy balance of the heat exchangers. It can be observed that the amount of preheating and the transferred heat in the liquid phase for the shell and tube evaporator is larger than the plate-type evaporator. In addition, the amount of superheating and the

transferred heat in the vapour phase for the shell and tube evaporator is less than the plate-type evaporator.

Quantitatively, for the shell and tube evaporator (for system with recuperator), the preheating temperature is 30.81 ^{o}C at transferred heat of 6.51kW and the superheating temperature is 16.81 ^{o}C at transferred heat of 3.06kW respectively. For the plate-type evaporator (for system with recuperator), the preheating temperature is 12.93 ^{o}C at transferred heat of 2.52kW and the superheating temperature is 55.65 ^{o}C at transferred heat of 8.61kW respectively.

The major difference between both evaporators is the temperature of the pinch point. For both evaporators, the pinch points are positioned at the beginning of the evaporation process and, hence, the evaporation temperature can be limited by different heat exchangers. As presented in both diagrams, the pinch point temperature of the shell and tube evaporator is much higher than the plate-type evaporator. Thus, the ORC fluid outlet temperature and the temperature transfer efficiency of the shell and tube evaporator are less than the plate-type evaporator (as discussed in previous sections). As shown in Fig. 5.10, the pinch point temperature for the shell and tube evaporator is 54.76 ^{o}C and plate-type evaporator is 25.2 ^{o}C respectively for the system with recuperator.

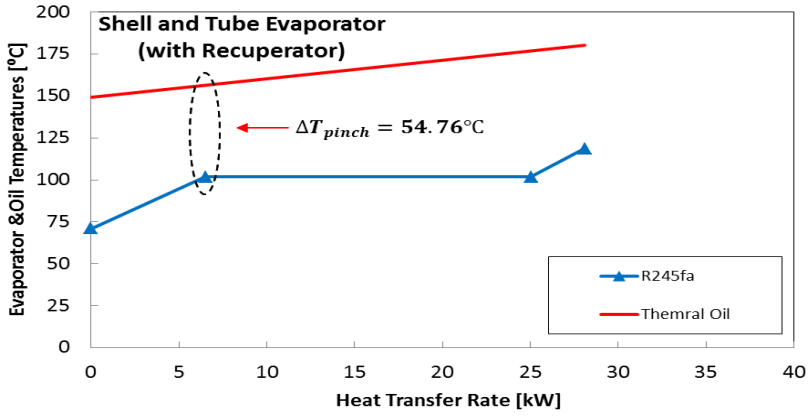

(a)

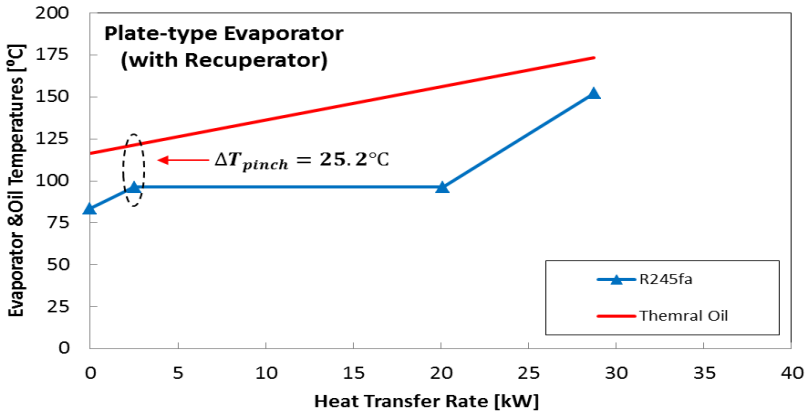

(b)

Figure 5.10 Temperature vs. heat transfer diagram of (a) shell and tube evaporator and (b) plate-type evaporator in the system with recuperator

Fig. 5.11 (a) presents the TQ diagram of R245fa at evaporating pressure of 10.89bar for shell and tube evaporator and Fig 5.11 (b) presents the diagram at evaporating pressure of 11.33bar for the plate-type evaporator (for the system without recuperator). The ORC fluid inlet temperature of the evaporator is almost same as the ambient temperature when the system is without recuperator. It can be observed that the amount of evaporator preheating and the transferred heat in the liquid phase for the system without recuperator is much larger than for the system with. Due to high preheating transferred heat in the liquid phase, the amount of superheating and the transferred heat in the vapour phase for the system without recuperator is less than for the system with.

For the shell and tube evaporator in the system without recuperator, the temperature of preheating is 78.3 ^{o}C at transferred heat of 14.85kW, while the superheating temperature is 0.07 ^{o}C at transferred heat of 0.01kW. For the plate-type evaporator, the preheating

temperature is 74.32 ^{o}C at transferred heat 12.96kW and the superheating temperature is 51.42 ^{o}C at transferred heat 7.69kW.

The pinch point temperature of both the evaporators in the system without recuperator is higher than the system with due to lower ORC fluid inlet temperature. And hence, the overall efficiency of the system without recuperator is lower than the system with, as analysed in the previous sections. The pinch point temperature for the shell and tube evaporator is 65.39 ^{o}C and the plate-type evaporator is 34.51 ^{o}C respectively for the system without recuperator.

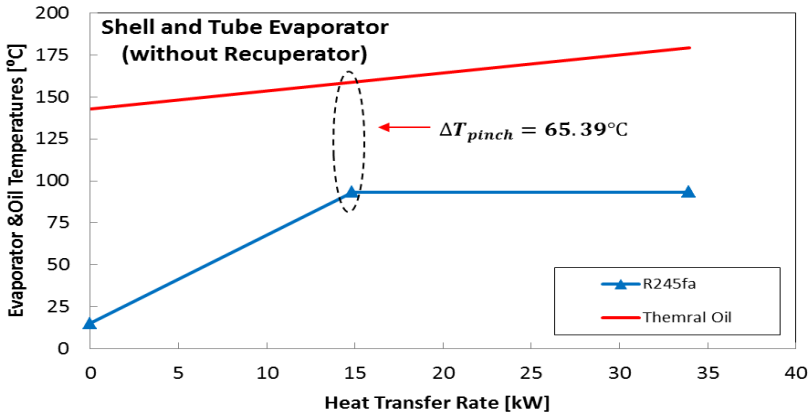

(a)

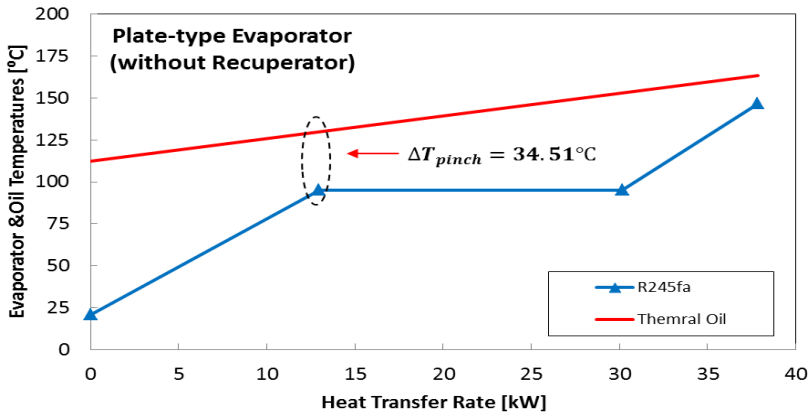

(b)

Figure 5.11 Temperature vs. heat transfer diagram of (a) shell and tube evaporator and (b) plate-type evaporator in the system without recuperator

5.4 Summary

This chapter provided a brief overview on the test facility of the R245fa ORC system. Three different components, scroll expander, shell and tube evaporator, and plate-type evaporator were integrated into the built-in test facility to test its impact in the system's

performance. The results of the experiments (each experiment focusing on a specific performance factor) are presented and discussed in this chapter. A thorough comparison of the shell and tube evaporator and the plate-type evaporator in regards to its effect in the performance of the system (with and without recuperator) has also been discussed. It is seen from the measurements that the expander power generation increases polynomially with higher pressure ratio while the expander overall efficiency increases with higher pressure ratio if it is not too high and decreases if the pressure ratio growths further. This indicates that there is an optimal pressure ratio to maximize the expander overall efficiency. In addition, the system overall efficiency also increases polynomially with higher pressure ratio and it can be greatly improved when a recuperator is employed irrespectively of the type of evaporator employed. The benefit of system performance from the recuperator integration is due to its contribution to the reduction of required evaporator heat capacity and the reduction of the required condenser capacity for the same condenser conditions. On the other hand, for a fixed system structure and component composition, both expander power generation and system overall efficiencies increase with higher evaporator heat capacity. But if the heat capacity is not quite high, the power generation and system overall efficiency are both higher when a plate evaporator and recuperator are employed compared to those with a shell and tube evaporator and recuperator. The research outcomes from this chapter can contribute significantly to the understanding of scroll expander operation at different pressure ratios and the effects of different types of evaporators and recuperator integrations on the system performance. It can therefore direct the ORC system designs and controls.

Chapter 6 will present a detailed outline on the design and construction of CO_2 transcritical power generation test facilities which includes various mechanical, electrical, control and monitoring systems.

Chapter 6 – EXPERIMENTAL SET-UP FOR THE INVESTIGATION OF THE PROPOSED CO_2 TRANSCRITICAL POWER CYCLES

6.1 Introduction

A small-scale test rig of CO_2 transcritical power generation (T-CO_2) system utilising low grade heat source to generate electric power was set up in a laboratory at Brunel University London. The T-CO_2 system was integrated with the CHP unit and the thermal oil rig, which are same facilities used into the R245fa ORC system. In order to analyse and evaluate the T-CO_2 system and its main components, several monitoring systems and instruments were installed into the system. This chapter presents a short review on the heat source system design and an overview on the T-CO_2 system.

6.2 Heat Source System Design

As mentioned in Section 3.2, the test facility of T-CO_2 system has been integrated with an existing 80 kW_e CHP Microturbine Power Generator (MTG) and its heat transfer loops, which are same as the heat source system of R245fa ORC system. Two independent power generation test rigs (R245fa ORC and T-CO2) have been installed beside the heat source system. The integration is set up with a thermal oil loop and two heat exchangers, a thermal oil boiler (Boiler heat exchanger) connected with the MTG gas flue, and a gas generator (Stacked Plate-type Heat Exchanger) attached with the T-CO_2 system. The thermal oil is heated up by the MTG exhaust gas and pumped to the T-CO_2 gas generator to generate high temperature CO_2 working fluid. The detailed design of the heat source system and the selected components are illustrated in Section 3.2.

6.3 T-CO_2 System Design and Component Selection

This section provides an overview of the experimental setup of the proposed T-CO_2 system for this project. Fig. 3.4 illustrates a detailed schematic diagram of the T-CO_2 test rig design and Fig. 3.5 illustrates the actual T-CO2 test rig installed in Brunel University London.

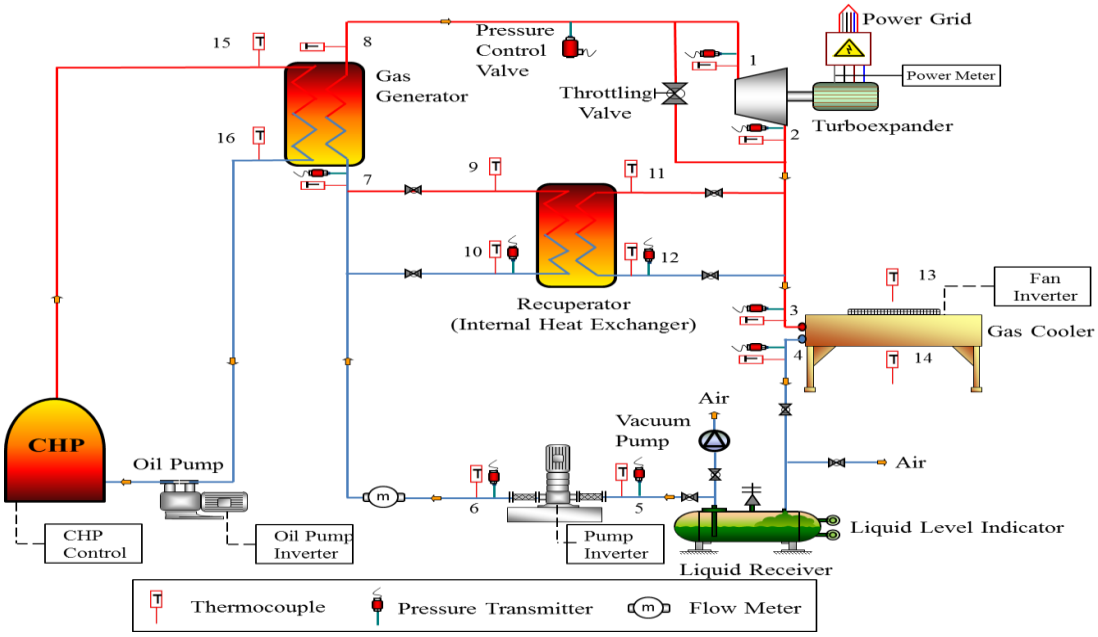

Figure 6.1 Schematic diagram of T-CO_2 test rig with heat source system

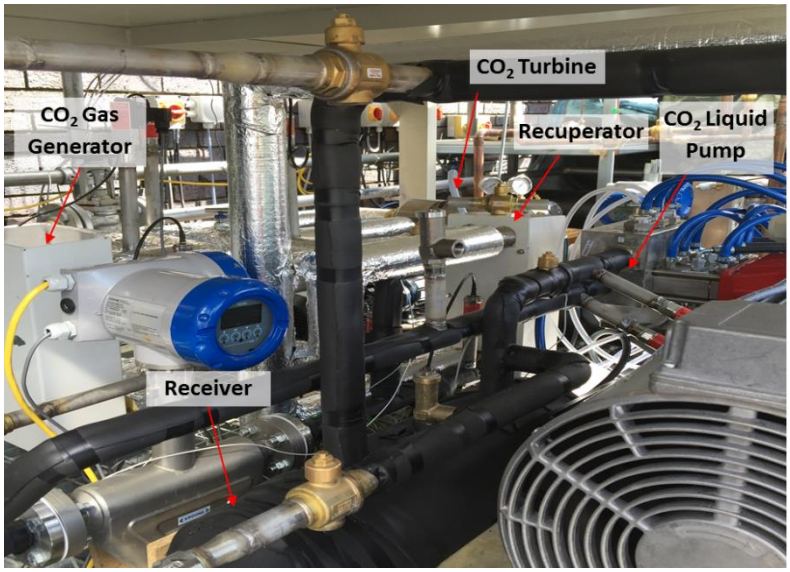

Figure 6.2 T-CO_2 test rig in Brunel University London

The T-CO_2 test rig consisted of various components including a thermal oil heated CO_2 gas generator, CO_2 turbine/expander and electric generator, recuperator, air-cooled condenser, receiver, CO_2 liquid pump, and other ancillary equipments.

Section 6.3.1-6.3.7 provides an overview (description and main parameters) of the main mechanical components of T-CO_2 system. The heat exchangers with heat capacities of 59.92kW for gas generator, 42.03kW for the recuperator and 47.3kW for condenser and the T-CO_2 turboexpander were selected using the thermodynamic analysis of the system, which is shown in Chapter 8.

6.3.1 CO_2 gas generator

For the T-CO_2 test rig, the CO_2 gas generator selected was a stacked plate-type heat exchanger. The gas generator had total heat transfer area of 1.15 m^2 and consisted of 30 plates. 14 channels and 15 channels were designated for the CO_2 flow and thermal oil flow respectively. The main parameters of the CO_2 gas generator are summarised in Table 6.1.

Table 6.1 Main parameters of the CO_2 gas generator

Parameters	Side 1	Side 2
Flow type	Counter-Current	
Heat capacity/ kW	59.92	
Total heat transfer area/ m^2	1.15	
Number of plates	30	
Vertical distance between centres of ports/ mm	329	
Horizontal distance between of ports/ mm	72	
Ports diameter/ mm	15	
Max. working fluid pressure/ bar	123	
Max. working fluid temperature/ ^oC	225	
Working fluid	R744 (CO_2)	Thermal oil
Number of channels	14	15

6.3.2 CO_2 turboexpander and electricity generator

A newly designed CO_2 extremely compact turboexpander was used for the power generation system. The purpose of the turboexpander was to reduce pressure and generate the electric power as shown in Fig. 6.3.

The high speed and permanent magnet synchronous electricity generator was driven by the CO_2 vapour (at high pressure and temperature) flowing through the turboexpander at rated revolution speed of approximately 18,000 rpm. The maximum design electric power output for this turbine is 5kW. The maximum working fluid temperature through the turboexpander was 110 ^oC (120 ^oC for short period). The turboexpander could

withstand a maximum pressure of 120 bar for high side and at 80 bar for low side respectively.

Meanwhile, the electricity generated by the generator was transmitted into the electric grid in the campus by means of a smart inverter and a transformer. The smart inverter provided by ABB allowed a generator speed matched and monitored by the electric power produced. In addition, the temperature control and safety relays of the turboexpander are connected to the main control system of the T-CO_2 test rig.

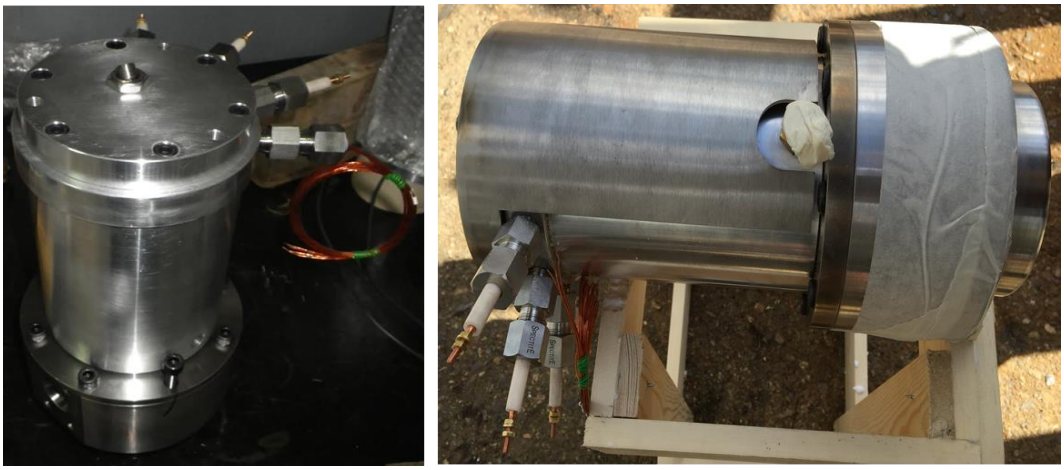

Figure 6.3 Photographs of CO_2 turboexpander

6.3.3 CO_2 recuperator

In order to examine the integration effect of recuperator in the T-CO_2 system, four two-way valves were installed respectively at the inlet and outlet of recuperator hot and cold side, as shown in Fig. 6.1. And thus, the test rig can be used to examine and compare the performance differences of the T-CO_2 system running with and without recuperator by turning the two-way valves either on or off. The total heat transfer area of plate-type recuperator is 1.15m^2 and consists of 30 plates. The high pressure CO_2 flowed through 14 channels and the low pressure CO_2 flowed through 15 channels. The main characteristics of CO_2 plate-type recuperator are summarised in Table 6.2.

Table 6.2 Main parameters of CO_2 plate-type recuperator

Parameters	Side 1	Side 2
Flow type	Counter-Current	
Heat capacity/ kW	42.03	
Total heat transfer area/ m^2	1.15	
Number of plates	30	
Vertical distance between centres of ports/ mm	329	
Horizontal distance between of ports/ mm	72	
Ports diameter/ mm	15	
Max. working fluid pressure/ bar	123	
Max. working fluid temperature/ ^oC	225	
Working fluid	R744 (CO_2) High Pressure	R744 (CO_2) Low Pressure
Number of channels	14	15

6.3.4 CO_2 condenser

Due to space limitations, the CO_2 air-cooled gas cooler/ condenser and the R245fa air-cooled condenser were installed in the same unit, with one component on top of the other, as shown in Fig. 3.9.

The CO_2 condenser is a specially designed component consisting of mechanical components such as, a CO_2 finned-tube heat exchanger, twelve electric air heater, one main fan and four recirculation fans. The detailed description and control strategies of the air cooled condenser are shown in Section 3.3.4. The main parameters of the air cooled finned-tube CO_2 condenser are summarised in Table 6.3.

Table 6.3 Main parameters of air cooled finned-tube CO_2 condenser

Parameters	
Surface area/ m^2	1.59
Heat capacity/ kW	47.3
Maximum air speed through condenser ($ms^{-1)}$	1.53
Total working fluid pipes (inlet/ outlet)	60
Number of main fan	1
Number of re-circular fans	4
Number of re-circular air heaters	12
Main fan control	Variable speed
Re-circular fans control	On/ off

6.3.5 CO_2 receiver

After the CO_2 was cooled in the air cooled condenser, the sub-cooled liquid CO_2 was fed into the CO_2 receiver. The CO_2 receiver is a horizontal receiver specially manufactured by Stanref Standard product type DIR97/23/EC for the test, as shown in Fig. 6.4. It has a volume of 20 litres, a test pressure of 90 bar and operates at minimum temperatures of -9 ^oC at 34bar and -50 ^oC at 27bar. The receiver is fitted with two sight glasses, a pressure relief valve and a pressure gauge.

The CO_2 receiver in the T-CO_2 system has three main purposes. Firstly, it can provide adequate storage capacity for the working fluid during servicing period when the system has to be shutdown to change the test conditions. Secondly, a deep tube installed in the receiver will ensure only liquid CO_2 is present in the receiver and not the vapour. This can also be visually monitored through the sight glasses of the receiver. The final purpose would be to provide a connection point for charging and cooling side.

Before charging CO_2 in the system, the system was fully pressure tested. The system was charged during standstill condition only. The CO_2 can be charged in the system using two methods. Firstly method would be by opening valve 1 of the receiver (as shown in Fig.6.4) when the system is still in vacuum condition. The system can only be charged until the pressure of the whole system is same as the pressure of the CO_2 cylinder. When both the pressures are equal, the system cannot continually be charged. During the process, valve 2 and valve 3 of the receiver have to be left open and valve 4 closed to allow the whole T-CO_2 system to be pressurised.

The second method involves charging the liquid CO_2 into the receiver when the two valves, valve 2 and valve 3, of the receiver are closed. During this process, valve 4 has to be opened and valve 1 closed to remove the gas CO_2 from the receiver. Valve 4 has to remain closed until the pressure gauge of the receiver reads 7bar. This will reduce the pressure and temperature of the receiver. Once all the criteria have been met, liquid CO_2 can be continually charged in the receiver until the receiver is full. The level of liquid CO_2 in the liquid receiver can be visually monitored from the sight glasses.

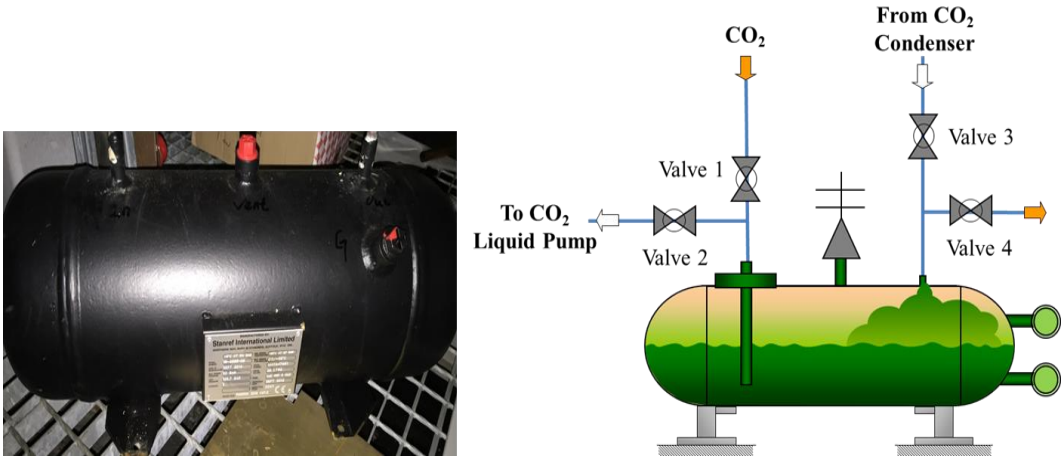

Figure 6.4 Photographs of CO_2 receiver

6.3.6 CO_2 liquid pump

From the CO_2 liquid receiver, the liquid CO_2 was then pumped back to the CO_2 gas generator/ recuperator cold side to continue another operation cycle. The high pressure CO_2 liquid pump flexi coupled with an 11 kW motor suitable for frequency inverter was used in the R245fa liquid pump as well. In addition, any leakages of CO_2 (at high and low pressure) from the CO_2 cooling channels of the liquid pump were connected back to the system. All the water cooling channels of the liquid pump used cold water provided by the condensing unit. This process was followed to prevent the building-up of any CO_2 gas in the liquid pump.

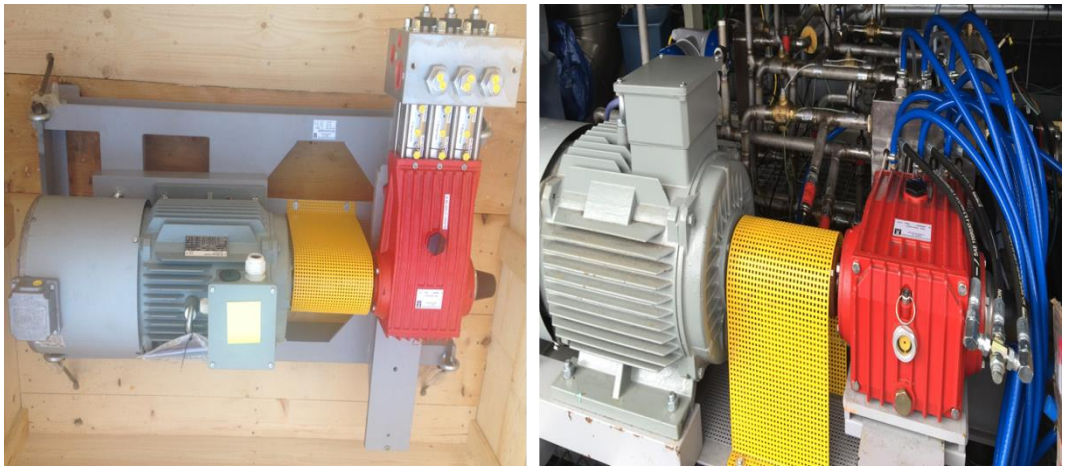

Figure 6.5 Photographs of CO_2 liquid pump

6.3.7 Working fluid flow control devices

Three main working fluid flow control devices were installed into the T-CO_2 system as shown in Fig. 6.6. The high pressure ball valves (Fig. 6.6(a)) were equipped on long lengths of stainless steel pipe to isolate the system in case of any leaks and changes in working fluid flow through components such as: recuperator, and liquid receiver. The maximum working pressure of the ball valve is 120bar.

A high pressure relief valve and a low pressure relief valve were installed at the outlet of the liquid pump and the top of liquid receiver respectively, as shown in Fig. 6.6(b). The pressure relief valves were set at the same pressure as the system maximum operating pressure, giving a burst pressure of 120bar at high pressure relief and 80bar at low pressure relief valve. At this set pressure, the minimum discharge capacities were determined to be 842.34kg/h for high pressure relief valve and 2511.6 kg/h for the low pressure relief valve.

The bypass subsystem consists of a high pressure and high temperature needle valve (Fig.6.6 (c)) installed in parallel to the CO_2 turboexpander. The maximum working temperature of the needle valve is 260 ^oC and pressure is 275.8bar. There are two reasons for installing the needle valve to the system. Firstly, it is used to simulate the expansion machine to reduce the working fluid pressure by changing the pressure ratio. Secondly, it is used to bypass a fraction of CO_2 to prevent it entering the CO_2 turboexpander during the starting and closing process, thus, can prevent the low pressure or temperature working fluid damaging the blades of CO_2 turboexpander.

(a)Ball valve (b)Pressure relief valves (c) Needle valve

Figure 6.6 Working fluid flow control devices

6.3.8 Auxiliary components

The main auxiliary components associated with the mechanical side of the T-CO_2 system have been described in previous sections. Other auxiliary components include the sight glasses on receiver, CO_2 charging sit and CP grade CO_2 cylinder, as illustrated in Fig. 6.7.

Two sight glasses are equipped in the CO_2 receiver (Fig. 6.7(a)). The purpose of the sight glasses is to be able to visually monitor the fluid in the receiver, especially when monitoring the fluid level during changing process and when ensuring the right amount of liquid flow by the working fluid pump during operational phase.

There are two charging sits equipped into the T-CO_2 system. One is in the discharge line of the CO_2 receiver just before the connection to the liquid pump and the other is in the suction line of the gas generator. The component enables the system to be charged in gas or liquid phase. Fig. 6.7(b) shows one of the charging sets which include charging valve, charging flow adjust valve, charging connection and flexible charging pipe. The charging valve is used to isolate the T-CO_2 system when the charging process is finished. The charging flow adjust valve is used to adjust the flow rate of CO_2 flow from the cylinder to the system. And the flexible charging pipe is used to connect the CO_2 cylinder with charging sit.

After the fabrication of the T-CO_2 system, the system was pressurised with nitrogen gas to check any leakages in the system. After that, the vacuum pump was then connected in one of the charging sit. Once the system was fully vacuumed, the CO_2 was charged from the cylinder (Fig.6.7 (c)) to the system. The detailed charging process has been described in Section 6.3.5.

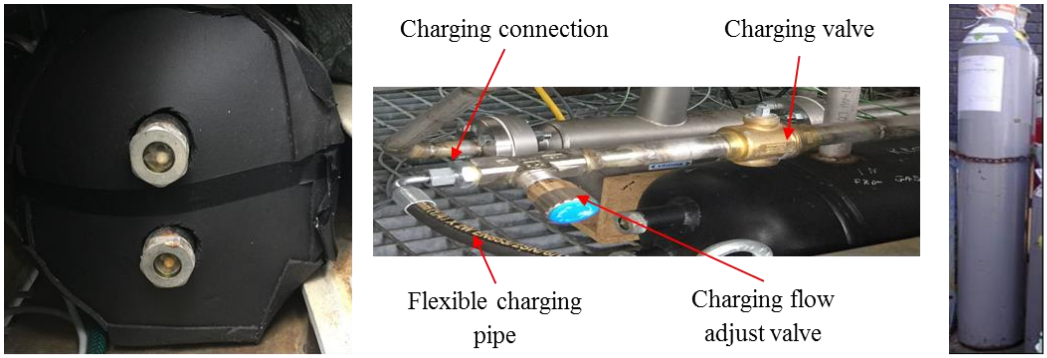

(a)Sight glass on receiver **(b) Charging Sit** **(c) CP grade CO_2**

Figure 6.7 The auxiliary components

6.4 Control System

As mentioned previously, the same heat source system (CHP unit) is used in both the R245fa ORC system and T-CO_2 system, and both the condensers are installed in the same unit. Hence, the heat source controller and heat sink control system of the T-CO_2 system are same as the ones for R245fa ORC system (please refer Section 3.4 for description on R245fa ORC system).

The T-CO_2 system controller is used for controlling the parameters of CO_2 mass flow rate and pump outlet pressure. The parameters are controlled by varying the frequency of inverter attached on the CO_2 liquid pump, as shown previously in Fig. 3.13. The same inverter can be attached on the ORC liquid pump or CO_2 liquid pump by adjusting the controller's switch.

The pressure control switch is a controller which has been specially developed to control the pressure conditions that exist in a T-CO_2 system and is installed at the outlet of the CO_2 gas generator. The pressure control switch is connected to the T-CO_2 main control system, which provides a signal from the gas generator pressure which is fitted in the outlet immediately after the gas generator. The controller at the pressure control switch opening will continue to maintain the maximum system operating pressure (120bar). When the system pressure higher than 120bar, the pressure control switch will provide signal to the main control panel to stop the CO_2 liquid pump. This design enables the safety of the components of T-CO_2 system. The maximum working pressure

range of the pressure control switch is between 16 and 160bar. The pressure control switch and its installation in the T-CO_2 system are illustrated in Fig. 6.8.

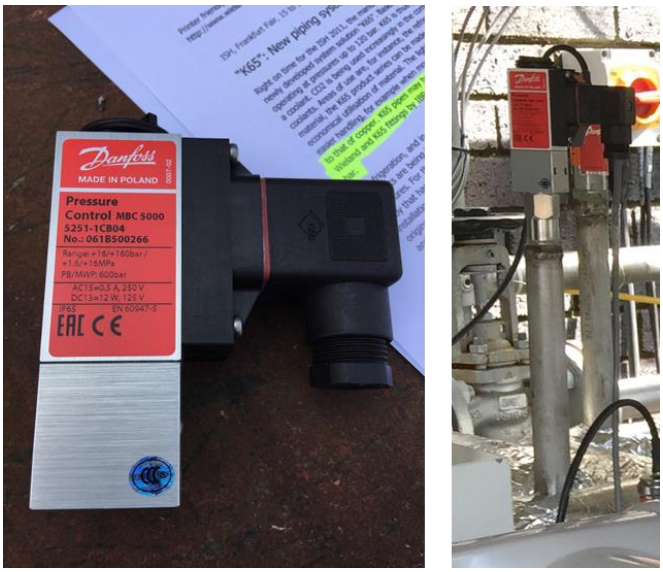

Figure 6.8 Photographs of pressure control switch

6.5 Instrumentation and Data Logging System

Different instruments were used in T-CO_2 system for taking measurement of both the control panel system and performance monitoring system. For control panel system, the instrumentation is mainly used for providing signal inputs (high and low pressure, ambient temperature and turboexpander internal temperature) to the control panel to alert of any safety and control strategy issues. For the performance monitoring system, the instrumentation is used for monitoring different parameters of the CO_2 such as the pressure, temperature and flow rate in the system. The instrumentation is also used to monitor the temperatures of thermal oil and ambient air and the power generation of the turboexpander.

The main instruments used in T-CO_2 system were temperature and pressure sensors, a working fluid flow meter, power meter and airflow meter. The methods followed to take measurements using these devices are provided in next two sections. The turboexpander power meter and ambient airflow meter used into the T-CO_2 system are same as the one used into the R245fa ORC system, as shown in Section 3.5.1.3 and Section 3.5.1.4.

All instrumentation output signals of the experimental data were transmitted to computer by a National Instruments data logging system, and displayed and recorded automatically by LabView software for further analysis. The same data logging system used into T-CO_2 system has been used for R245fa ORC system, thus, the detailed description on the system is shown in Section 3.5.2.

6.5.1 Temperature and pressure measurements

To measure the temperature of the system and its main components, a K-type PTFE thermocouple was installed at the inlet and outlet of each component in the T-CO_2 system, heat source system and heat sink systems. The temperature measurement range of the K-type thermocouple was between -10 ^{o}C to 1100 ^{o}C with specific error (specified by manufacturer) of ±0.5 ^{o}C. Similar to the R245fa ORC system, the thermocouples were calibrated by a calibration bath and a precision thermometer with accuracy of ±0.04 ^{o}C. The temperature range of calibration was between 10 ^{o}C to 90 ^{o}C. It was found that all thermocouples had calibration error within the specifications.

Positions of all the thermocouples on the T-CO_2 test rig are indicated in Fig. C-6 (Appendix C). The number and calibration equations of the thermocouples including their calibration errors are given in Table C.4 (Appendix C).

Nine high pressure transducers (Danfoss products) were installed on the T-CO_2 test rig. The pressure transducers on the T-CO_2 test rig were used for measurements in the control system. The measured pressure range of the pressure transduces was between 0-160bar (MBS33). The pressure transducers have input voltage of 24V d.c. and output current of 4mA to 20 mA with response time of 0.4s the data logging system. The deadweight pressure gauge calibrator was used to calibrate each pressure transducer of the T-CO_2 test rig. The current outputs were recorded for a series of known pressures. The pressure range of calibration was set between 0 and 150bar.

Based on the results, the graphs of the current against the pressure were plotted and the best-fit linear equations obtained and used in the data logging system to enable automatic recording of the measured pressure in the T-CO_2 system. The overall coefficient of correlations of the high pressure transducers was about 99.9% with manufacturer uncertainty of ± 0.3%. The calibration equations of the pressure transducers of the T-CO_2 system can be found in Table C.5 (Appendix C).

6.5.2 Flow meter

In the T-CO_2 test rig, a fully welded maintenance free sensor with twin V-shaped measuring tube mass flowmeter was used to measure the liquid mass flow of CO_2 exiting the liquid pump. The flowmeter Optimass 6000-H10 (Fig. 6.9) was used in the system to measure the mass flow in the range of 0~1800kg/h with an accuracy of ±0.1%. The flowmeter has high pressure capability up to 200 bar and temperature range of -200 ^{o}C to 400 ^{o}C.

A current signal output 4-20 mA has provided by the flow meter. The signal output is directly connected to the current module of the data logging system. In order to convert the parameter of current to parameter of flow rate, a calibration was carried out by the manufacturer. Best-fit linear equation from calibration of the mass flowmeter was used in the data logging software to enable recording and displaying of the mass flow rate directly.

Figure 6.9 Flow meter OPTIMASS 6400c

6.6 Summary

The chapter covered a detailed outline on the design and construction of T-CO_2 test rig. The chapter also covers a brief overview on the mechanical, electrical, and control devices of the test rig along with the instrumentation and data logging system used during the test. The test rig consists of a number of essential components including a CO_2 turboexpander with high speed generator, finned-tube air cooled condenser, liquid receiver, CO_2 liquid pump and CO_2 gas generator.

The heat source and sink systems used for the T-CO_2 system were same as the ones used for ORC system, hence, the information in relation to the system can be found in Chapter 3. Similarly, a thorough description of the components of control and data logging system can be found in previous section as well (the components used for control and data logging for both the system are same). The test rig has been fully commissioned, instrumented, controlled and is ready to operate experiment as required.

The following chapter, Chapter 7, will present the experimental results from the T-CO_2 system with CO_2 turboexpander and CO_2 plate-type gas generator. Subsequently, at constant heat sink (ambient) and heat source (thermal oil) temperatures, a series of experiments have been carried out to examine the effects of various important parameters on the T-CO_2 system performance. The chapter will discuss and highlight the effect of heat source parameters and CO_2 liquid pump speeds on the performances of system and components.

Chapter 7 – EXPERIMENTAL RESULTS AND DISCUSSION USING CO_2 TRANSCRITICAL POWER CYCLES WITH TURBOEXPANDER

This chapter provides a brief overview of the as-built test rig and discusses the experiments conducted to test the performance of small scale T-CO_2 system with turboexpander and plate-type gas generator. For this particular set of experiments, the recuperator has not been used. In addition, the chapter also analyses the effects of different heat source and CO_2 liquid pump parameters on the performances of system.

7.1 Overview of the As-built Test Facility and Test Conditions

In this study, an experimental research was conducted to investigate the performance of the T-CO_2 system utilising low grade heat sources to generate electric power at different operating conditions. A schematic diagram of a small-scale T-CO_2 test rig is presented in Fig. 7.1. The overall system consists of two sections: heat source system and T-CO_2 system. An overview of the T-CO_2 experimental set-up and individual test rig components can be found in Chapter 6. The heat source system is the same system used in the R245fa ORC system mentioned in Chapter 3 and consists similar components as the ones used for T-CO_2 system. The components include a turboexpander with high speed generator, finned-tube condenser, CO_2 liquid pump, recuperator and plate-type gas generator. CO_2 (R744) was selected as the working fluid of the system due to its low greenhouse gas effects, Global Warming Potential (GWP) of 1, and its thermophysical properties. In addition, four two-way valves, each installed in the entry and exit point of the recuperator (position 9, 10, 11 and 12 in schematic diagram), allows the system performance to be measured with and without recuperator. For this particular set of tests, the recuperator has not been used.

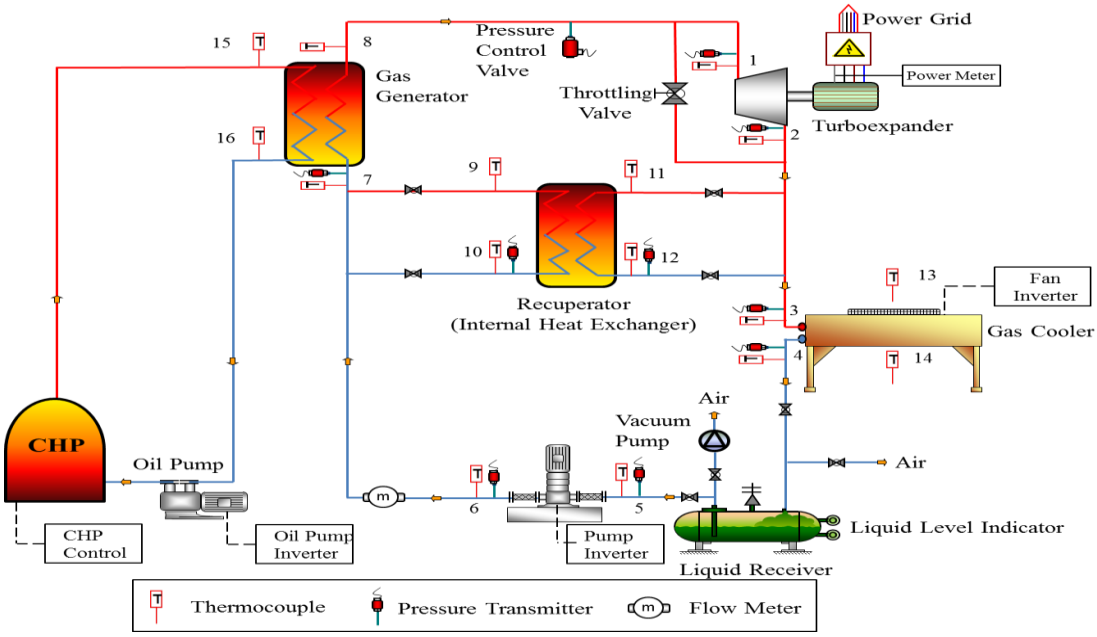

Figure 7.1 Schematic representation of a T-CO_2 test rig with turboexpander

As listed in Table 7.1, a series of measurements were carried out on the test rig using different heat source and sink parameters. For the heat source parameters, the temperature was varied between 142.4 ^{o}C and 144.4 ^{o}C by controlling the thermal oil flow rate from 0.25kg/s to 0.5kg/s. As for the heat sink parameters, the temperature was varied from 22.5 ^{o}C to 23.5 ^{o}C but the flow rate was kept constant. In addition, the CO_2 mass flow rate was controlled by changing the CO_2 liquid pump motor frequencies between the range of 0.2 kg/s and 0.3 kg/s. These settings were designed to ensure the inlet temperatures and pressures of CO_2 turboexpander were within their maximum limitations during the tests. The temperature was set as 110 ^{o}C (120 ^{o}C for a short period) and pressure at 110 bar respectively by the turboexpander manufacturer. The test results can be used to further investigate the system and improvements.

Table 7.1 Variation of operating parameters for the system test

Thermal oil inlet temperature (^{o}C)	Thermal oil flow rate (kg/s)	Condenser inlet air flow temperature (^{o}C)	Condenser inlet air flow rate (m^3/s)	CO_2 mass flow rate (kg/s)
142.4~144.4	0.25~0.5	22.5~23.5	4.267	0.2~0.3

7.2 Experimental Data Collection and Processing

Temperatures, pressures, mass flow rate and other auxiliary data of CO_2 and thermal oil were measured and recorded by the data logging system for each steady state test. Each test was conducted for at least 20 minutes, with sample recorded at every 1 second. Please refer Section 6 (Chapter 6) for description on the instrumentations and data logging system for T-CO_2 system. All relevant thermophysical properties of the fluid, such as enthalpy and entropy, were calculated using REFPROP 8.0 software (Lemmon et al., 2007) based on the average measured temperature and pressure at each point in T-CO_2 system.

7.2.1 Power generation of CO_2 turboexpander

Two kinds of CO_2 turboexpander power generation have been used in the data collection and processing. The first one (W_{T,CO_2}) is from the generator turboexpander directly measured, and another one (W'_{T,CO_2}) is actual cycle power generations calculated individually from the product of measured CO_2 mass flow rate and the enthalpy difference between the turboexpander inlet and outlet, as shown in Equation 4.1. The variable subscript numbers in these equations are corresponding to the ones indicated in Fig. 7.1.

$$W'_{T,CO_2} = \dot{m}_{f,CO_2}(h_1 - h_2) \tag{7.1}$$

Where $\dot{m}_{f,CO_2}$ is the T-CO_2 working fluid mass flow rate (kg/s) measured by the T-CO_2 flow meter, as described in Section 6.5.2.

7.2.2 Heat capacity of gas generator

The heat capacity of gas generator in T-CO_2 system is the key impact factor of the system's performance. Thus, the heat capacity of gas generator can be calculated in Equation 7.2.

$$Q_{gg} = \dot{m}_{f,CO_2}(h_8 - h_7) \tag{7.2}$$

7.2.3 Isentropic and overall efficiencies of CO_2 turboexpander

As shown in Fig. 7.1, the T-CO_2 system is a closed loop system, the first law of thermodynamics and mass conservation of working fluid can be applied to the T-CO_2 system to analyse the performance of the CO_2 turboexpander. The isentropic ($\eta_{T,co_2,is}$) and overall ($\eta_{T,co_2,all}$) efficiencies of the CO_2 turboexpander are calculated using Equations (7.3) and (7.4) respectively based on the measurements. The calculation method for working out the CO_2 turboexpander overall efficiency is same as the one for R245fa turboexpander, as described in Section 4.2.2.2.

$$\eta_{T,co_2,is} = \frac{(h_1 - h_2)}{(h_1 - h_{2,is})} \tag{7.3}$$

$$\eta_{T,co_2,all} = \eta_{T,CO_2,is}\,\eta_{T,CO_2m}\,\eta_{T,CO_2,e} = \frac{W_{T,CO_2}}{\dot{m}_{f,CO_2}(h_1 - h_{2,is})} \tag{7.4}$$

7.2.4 Uncertainty in calculation

Considering the uncertainty of the measured variables, which include CO_2 temperatures, CO_2 pressure, CO_2 mass flow rates, and CO_2 turbine power generation, an error margin was found for each variable. Thus, the uncertainly in the calculation of CO_2 turbine power generation, heat capacity of gas generator, CO_2 turbine isentropic efficiency and CO_2 turbine overall efficiency were found to be ±15%, ±1.08%, ±15.2% and ±1.54% respectively. Detailed explanation of the uncertainty analysis is given in Append D.

7.3 Test Results

As demonstrated in Table 7.1, for all heat source parameters, thermal oil temperatures do not vary significantly. At the heat sink side, both condenser inlet air temperatures and flow rates remain approximately at constant. Therefore, from the test results, only the effects of thermal oil flow rate and CO_2 mass flow rate on system performance have been selected and presented in this section.

Fig. 7.2 shows the variations of CO_2 mass flow rate with different CO_2 liquid pump speeds and heat source flow rates. At a fixed heat source flow rate, the CO_2 mass flow

rate increases with higher CO_2 liquid pump speed. Simultaneously, at a constant CO_2 pump speed, the thermal oil flow rate dominates over the oil pump speed and hence eventually on the CO_2 mass flow rate. The lower thermal oil flow rate can produce increased CO_2 mass flow rate. The test results illustrate that CO_2 mass flow rates in the T-CO_2 power cycle can be effectively controlled by modulating the CO_2 liquid pump speeds. Subsequently, the effect of the CO_2 liquid pump speed on system performance can be represented by the CO_2 mass flow rate.

Quantitatively, when CO_2 pump speed was increased from 25Hz to 35Hz, the CO_2 mass flow rate increased by 27.8% for the thermal oil flow rate at 0.364kg/s and by 25.7% for 0.463kg/s respectively. In addition, when thermal oil flow rate was increased from 0.364kg/s to 0.463kg/s, the CO_2 mass flow rate increased by 2.2% for the CO_2 pump speed at 30Hz and 1.4% for 35Hz respectively.

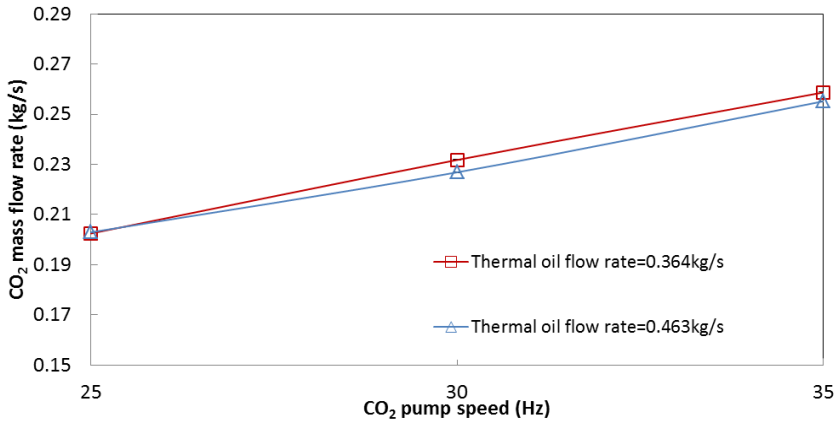

Figure 7.2 Variations of CO_2 mass flow rate with different CO_2 pump speeds and heat source flow rates

The effect of varying CO_2 turbine inlet and outlet pressures with different CO_2 mass flow rate and thermal oil flow rate were measured and plotted, as illustrated in Fig. 7.3. The results show that the higher thermal oil mass flow rate will result in higher CO_2 pressure at turbine inlet and outlet. Similarly, the greater CO_2 mass flow rate will increase both CO_2 pressures at turbine inlet and outlet especially when the CO_2 mass flow rate is more than 0.23kg/s.

Similarly, Fig. 7.4 presents the effect of CO_2 mass flow rate and the thermal oil mass flow rate on the CO_2 pressures at pump inlet and outlet. In percentage, when CO_2 mass flow rate was increased from 0.2kg/s to 0.26kg/s, the turbine inlet pressure increased by

11.6% and 14.2%, the turbine outlet pressure by 6.8% and 8.1%, the CO_2 pump inlet pressure by 6.4% and 7.6%, and the CO_2 pump outlet pressure by 11.5% and 14.2% for the thermal oil flow rate at 0.364kg/s and 0.463kg/s respectively. When the thermal oil flow rate increased from 0.364kg/s to 0.463kg/s, the turbine inlet pressure increased by 0.24% and 2.0%, the turbine outlet pressure by 0.1% and 0.6%, the CO_2 pump inlet pressure by 0.2% and 0.7%, and the CO_2 pump outlet pressure by 0.1% and 1.9% for the CO_2 mass flow rate at the range of 0.22kg/s to 0.23kg/s, and 0.25kg/s to 0.26kg/s respectively.

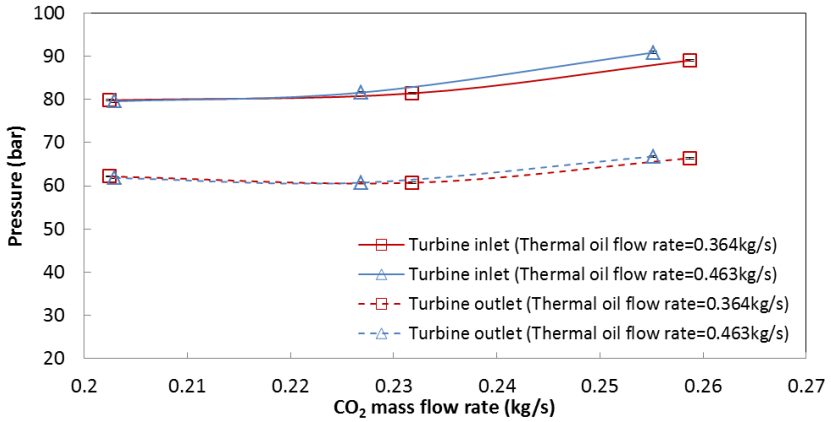

Figure 7.3 Variation of CO_2 turbine pressures with different CO_2 mass flow rates and thermal oil flow rates

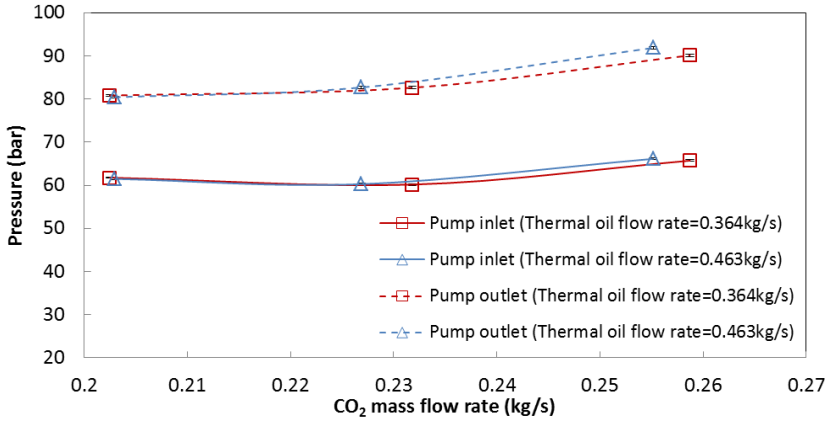

Figure 7.4 Variation of CO_2 pump pressures with different CO_2 mass flow rates and thermal oil flow rates

On the other hand, the effects of the CO_2 mass flow rate and thermal oil flow rate on the CO_2 temperatures at the primary components inlets and outlets have also been measured and presented in Fig. 7.5-7.8. Fig. 7.5 shows that the higher CO_2 mass flow rate will result in lower CO_2 temperature at either the turbine inlet or outlet due to the heat transfer behaviours in the gas generator and the specified power generation for the turbine. The increased CO_2 mass flow rate in the system resulted in higher heat transfer rate from the heat exchangers (gas generator or condenser). The increased heat capacity of the heat exchangers along with increasing pump speed resulted in decreased thermal oil outlet temperature. Similarly, the temperature of CO_2 turbine inlet (gas generator outlet) decreased with increasing CO_2 mass flow rate due to fixed heat source parameters. Simultaneously, the higher thermal oil mass flow rate can increase the turbine inlet and outlet temperatures.

Similar effects have been observed for the CO_2 mass flow rate and thermal oil flow rate on the condenser CO_2 inlet temperature and the CO_2 gas generator outlet temperature, as presented in Fig. 7.6 and Fig. 7.7. However, their effects on the CO_2 gas generator inlet temperatures and condenser CO_2 outlet temperatures are not as significant. The variation of thermal oil temperatures at the gas generator inlet and outlet with CO_2 mass flow rate and thermal oil flow rate has also been measured and presented in Fig. 7.8. It can be seen that the thermal oil temperatures are not affected much by the CO_2 mass flow rate. However, the higher thermal oil mass flow rate does increase the oil temperature of gas generator outlet. The thermal oil inlet temperature is not affected much by the thermal oil mass flow rate.

Generally, when CO_2 mass flow rate was increased from 0.2kg/s to 0.26kg/s, the turbine inlet temperature decreased by 21.1% and 7.1%, turbine outlet temperature by 29.1% and 12.0%, condenser CO_2 inlet temperature by 28.7% and 12%, and gas generator CO_2 outlet temperature by 21.0% and 7.3% for the thermal oil flow rate at 0.364kg/s and 0.463kg/s respectively. When the thermal oil flow rate was increased from 0.364kg/s to 0.463kg/s, the turbine inlet temperature increased by 7.3% and 12.4%, turbine outlet temperature by 8.8% and 14.6%, condenser CO_2 inlet temperature by 8.7% and 14.6%, gas generator CO_2 outlet temperature by 7.0% and 12.2%, and the thermal oil temperature of gas generator outlet by 5.4% and 9.8% for the CO_2 mass flow rate at range of 0.22kg/s to 0.23kg/s, and 0.25kg/s to 0.26kg/s respectively.

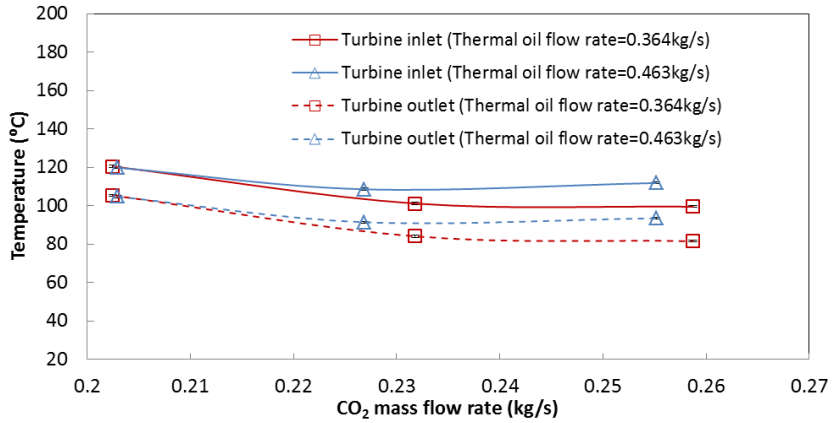

Figure 7.5 Variation of CO_2 turbine temperatures with different CO_2 mass flow rates and thermal oil flow rates

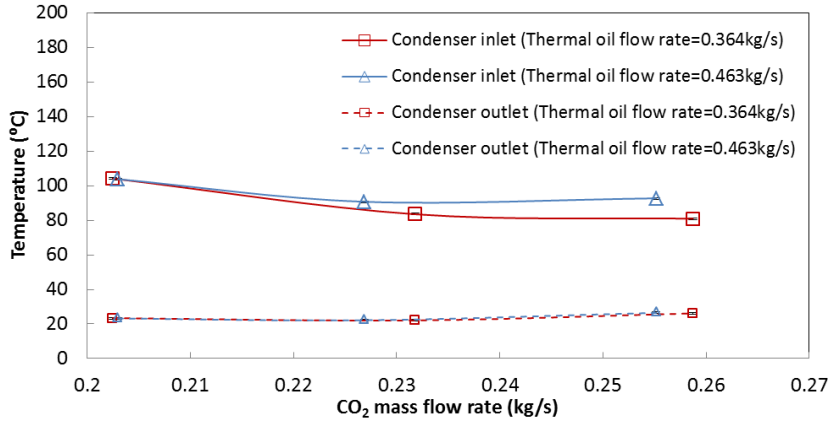

Figure 7.6 Variation of condenser CO_2 temperatures with different CO_2 mass flow rates and thermal oil flow rates

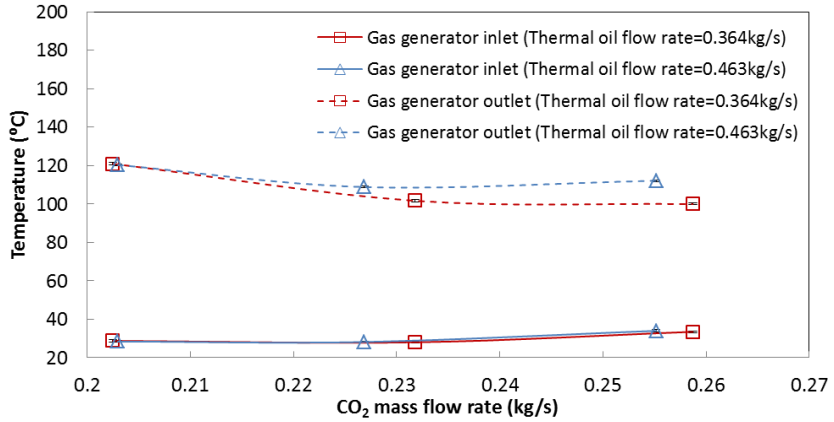

Figure 7.7 Variation of CO_2 gas generator temperatures with different CO_2 mass flow rates and thermal oil flow rates

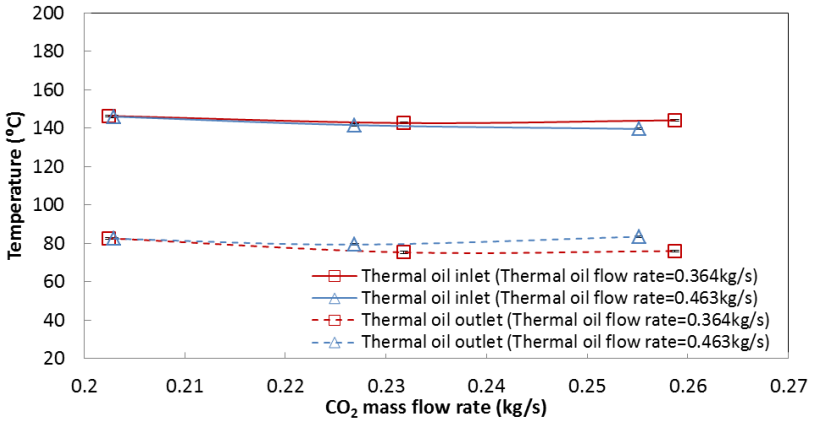

Figure 7.8 Variation of thermal oil temperatures with different CO_2 mass flow rates and thermal oil flow rates

In addition, the effect of CO_2 mass flow rate on the parameters of power generations, CO_2 turboexpander efficiencies and gas generator heat capacity were also measured, as presented in Fig. 7.9-7.11 respectively.

The effect of the mass flow rate and thermal oil flow rate on the power generation of CO_2 turboexpander is illustrated in Fig.7.9. There are two groups of results in the Figure, the solid lines represent the turboexpander generator measurements and the dotted lines represent the actual cycle power generations calculated individually from the product of measured CO_2 mass flow rate and the enthalpy difference between the turbine inlet and outlet. The enthalpy at either turboexpander inlet or outlet is calculated from corresponding measurements of temperature and pressure, as shown in Equation 4.1. The ratio of turboexpander power generation to actual cycle power generation is a product of turboexpander mechanical efficiency and electrical efficiency, both of which need to be significantly improved. For the measured values of the turbine power output, the mechanical and electric efficiencies of the CO_2 turbine are too low. As observed from the measurements, the power generation for both the groups increased with higher CO_2 mass flow rates and higher thermal oil flow rates, further increasing the overall power generation.

Accordingly, the turboexpander isentropic efficiency and overall efficiency are calculated at different CO_2 and thermal oil mass flow rates, as depicted in Fig. 7.10. The results show that higher CO_2 mass flow rates further increases the overall turboexpander efficiency but does not benefit isentropic efficiency, which in turn should be

significantly affected by turboexpander pressure ratio and speed. In addition, higher thermal oil flow rates can reinforce a bit both turboexpander isentropic and overall efficiencies. The effects of different CO_2 and thermal oil mass flow rates on the gas generator heat capacity are presented in Fig. 7.11. The higher CO_2 mass flow rate can cause increased gas generator heat capacity. In the meantime, the greater thermal oil flow rate can also increase the gas generator heat capacity although the effect is more significant when the CO_2 mass flow rate is higher than 0.2kg/s.

It should be noted that the power generation is much less than the designed value of 5kW. This can be achieved by further increasing CO_2 mass flow rate through the CO_2 liquid pump speed, thermal oil mass flow rate by the thermal oil pump speed and pressure difference at turbine inlet and outlet. Nevertheless, there is an increase limitation for the power generation due to the limited pressure and temperature at the turbine inlet. Further design improvement for the CO_2 turbine needs to be considered in the near future.

Quantitatively, when CO_2 mass flow rate increased from 0.2kg/s to 0.26kg/s, the percentage increase rates of measured turboexpander power generation were 116.9% and 92.1%, the calculated turboexpander power generation, 5.0% and 18.8%, turboexpander overall efficiency, 66.7% and 35.4% for the thermal oil flow rate at 0.364kg/s and 0.463kg/s respectively. On the other hand, the percentage decrease rates of turboexpander isentropic efficiency were 23.9% and 19.4%, and the percentage increase rates of gas generator heat capacity were 5.0% and 10.0%.

When the thermal oil flow rate increased from 0.364kg/s to 0.463kg/s, the percentage increase rates of measured turboexpander power generation were 1.7% and 14.8%, the calculated turboexpander power generation, 7.7% and 10.8%, turboexpander isentropic efficiency, 5.2% and 0.6%, and gas generator heat capacity, 1.3% and 5.2% for the CO_2 mass flow rate at range of 0.22kg/s to 0.23kg/s, and 0.25kg/s to 0.26kg/s respectively.

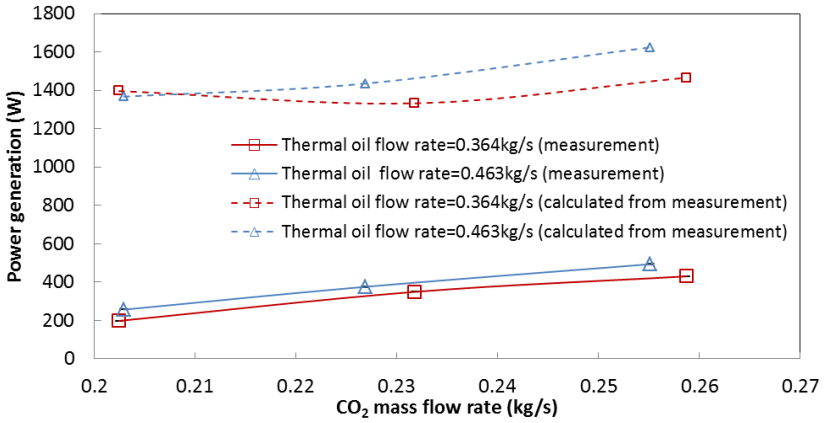

Figure 7.9 Variation of turbine power generations with different CO_2 mass flow rates and heat source flow rates

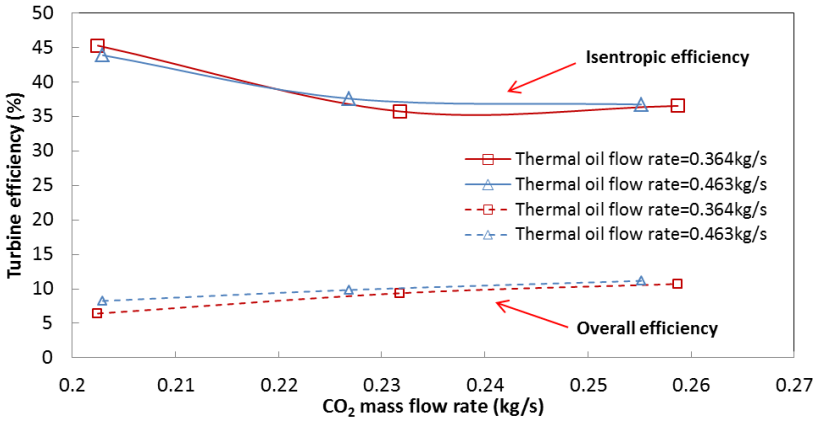

Figure 7.10 Variation of turbine efficiencies with different CO_2 mass flow rates and heat source flow rates

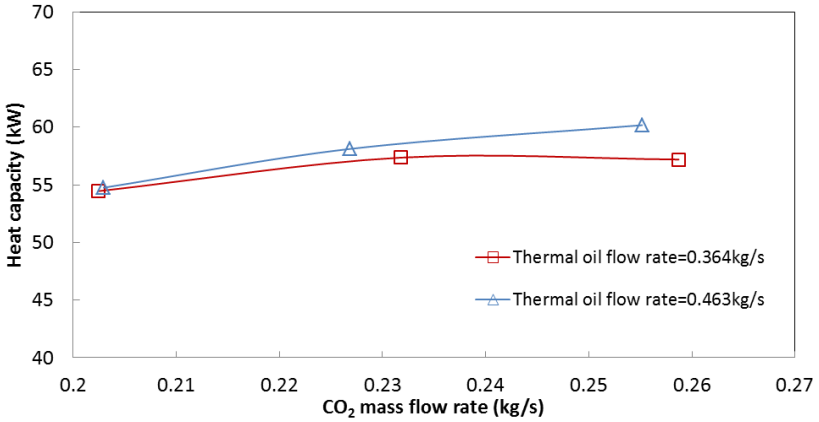

Figure 7.11 Variation of gas generator heat capacity with different CO_2 mass flow rates and heat source flow rates

7.4 Performance of oil-heated CO_2 gas generator

The temperature vs. heat transfer (TQ) diagrams of CO_2 gas generator with different thermal oil flow rate and CO_2 flow rate are presented in Fig. 7.12. There are two lines of results in the Figure; the red lines represent the thermal oil inlet and outlet temperatures, via gas generator heat capacities, while, the blue lines represent the gas generator inlet and outlet temperatures of CO_2 side via gas generator heat capacities. The temperature difference of the gas generator is calculated from the difference between the thermal oil inlet temperature and the gas generator CO_2 outlet temperature.

Example of TQ diagram of T-CO_2 system gas generator is presented for thermal oil flow rate with 0.364kg/s and CO_2 flow rate with 0.257kg/s in Fig. 7.12 (a). As seen from the Figure, the temperature difference of gas generator is 44.13 ^{o}C.

When the thermal oil flow rate is kept constant (0.364kg/s) and the CO_2 flow rate is reduced from 0.257kg/s to 0.203kg/s, the temperature difference of gas generator is decreased to 25.41 ^{o}C, as shown in Fig. 7.12 (b). However, when the CO_2 flow rate is kept constant at 0.257kg/s (compare with Fig. 7.12 (a)) and the thermal oil flow rate is increased from 0.364kg/s to 0.463kg/s, the temperature difference of gas generator is decreased from 44.13 ^{o}C to 27.43 ^{o}C, as shown in Fig 7.12 (c). In addition, the main differences between Fig. 7.12 (a), (b) and (c) are thermal oil mass flow rate and CO_2 mass flow rate, the inlet temperatures of heat source (thermal oil) and heat sink (air flow) are kept almost constant for those three situations above. The demonstrations from the measurements can also reveal that the higher CO_2 mass flow rate will effectively increase the heat changer capacity and decrease CO_2 turbine inlet temperature. Meanwhile, the higher thermal oil flow rate will increase both the heat exchanger capacity and CO_2 turbine inlet temperature. These will further help to understand the controls of CO_2 parameters at the turbine inlet.

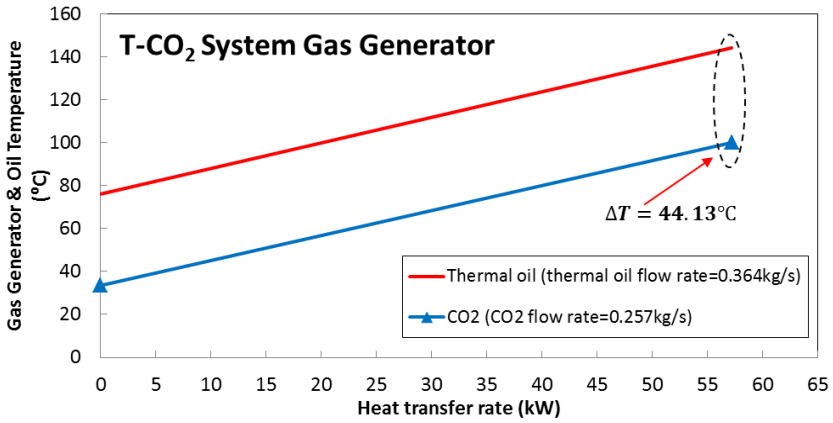

(a)

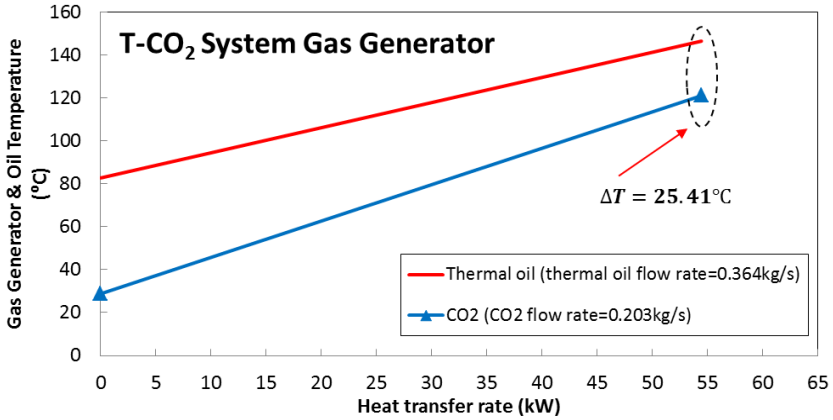

(b)

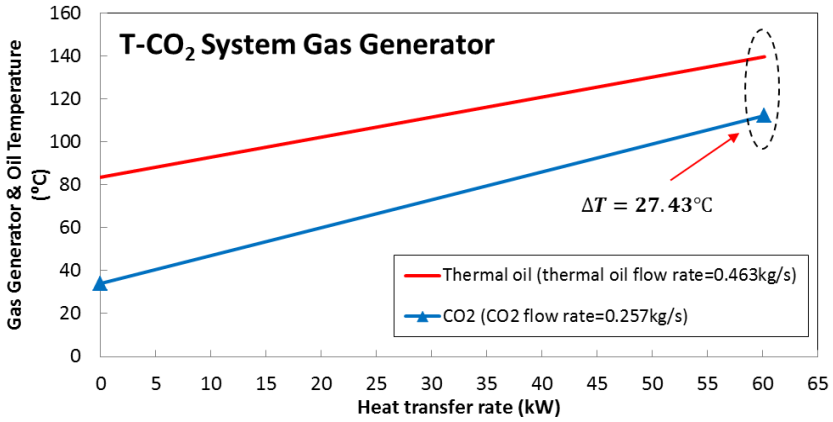

(c)

Figure 7.12 Temperature vs. heat transfer rate diagrams of (a) lower thermal oil flow rate and higher CO_2 flow rate, (b) lower thermal oil flow rate and lower CO_2 flow rate and (c) higher thermal oil flow rate and higher CO_2 flow rate.

7.5 Control Strategies

The turboexpander inlet temperature and pressure are two important parameters to be controlled in a T-CO_2 system considering their significant impacts on the system power generation and performances. These two control parameters will also ensure that the CO_2 turboexpander temperature and pressure are always within their maximum limitations.

As explained in Section 7.3, the CO_2 turboexpander inlet temperature is affected by the thermal oil flow rates and CO_2 mass flow rates in the system. For the transcritical power generation system, there is no evaporating process in the gas generator. So, the turbine inlet temperature becomes the only control temperature for the turbine, which is difference as R245fa ORC system using superheat at turbine inlet to control, as shown in Section 3.4 (Chapter 3). The relations between thermal oil flow rate or CO_2 mass flow rate, and CO_2 temperatures at turboexpander inlet are presented in Fig. 7.13 and Fig. 7.14 respectively. It is seen that the thermal oil flow rate should increase and the CO_2 mass flow rate should decrease almost linearly with higher CO_2 temperature at turboexpander inlet, which can be correlated as below:

$$\dot{m}_{f,oil} = 0.0041 T_{CO_2,T,in} - 0.0426 \tag{7.5}$$

$$\dot{m}_{f,CO_2} = -0.0022 T_{CO_2,T,in} + 0.4661 \tag{7.6}$$

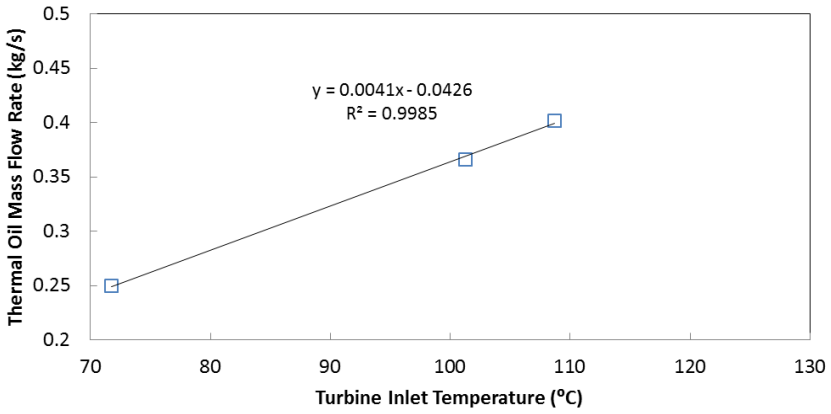

Figure 7.13 Relations between thermal oil mass flow rates and CO_2 turbine inlet temperatures

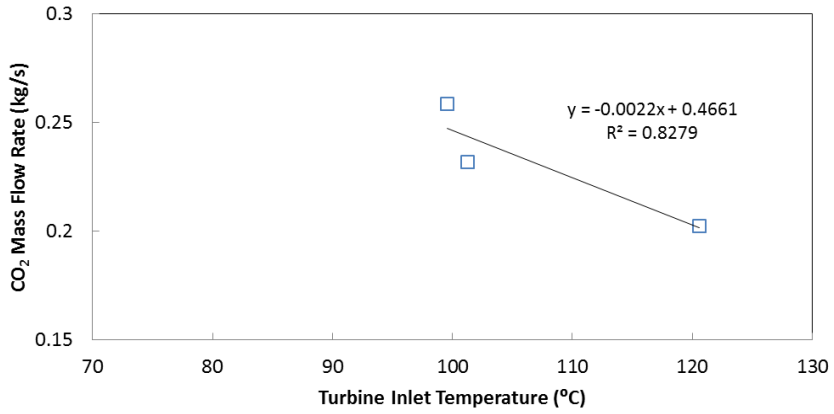

Figure 7.14 Relations between CO_2 mass flow rates and CO_2 turbine inlet temperatures

As mentioned in Section 7.3, the CO_2 pressure at turboexpander inlet is strongly affected by the CO_2 mass flow rate and thermal oil flow rate such that the control function between these parameters can be constructed. As depicted in Fig.7.15 and 7.16, the thermal oil flow rate and CO_2 mass flow rate should increase near linearly if higher CO_2 pressure at turboexpander inlet is required which can be correlated using the following equations:

$$\dot{m}_{f,oil} = 0.0324 P_{CO_2,T,in} - 2.4953 \tag{7.7}$$

$$\dot{m}_{f,CO_2} = 0.0041 T_{CO_2,T,in} - 0.1202 \tag{7.8}$$

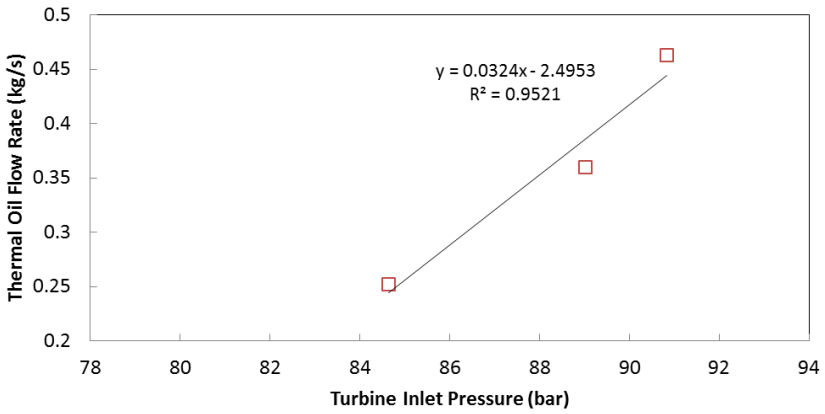

Figure 7.15 Relations between thermal oil mass flow rates and CO_2 turbine inlet pressures

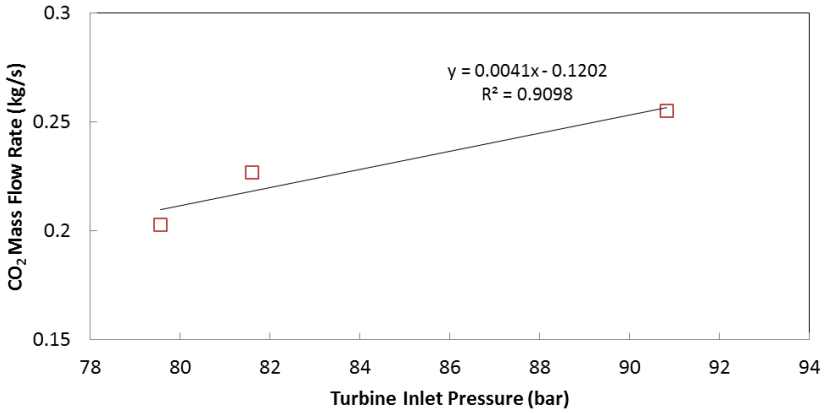

Figure 7.16 Relations between CO_2 mass flow rates and CO_2 turbine inlet pressures

In practice, these four functions listed in Equation 7.5 to 7.8 can be used to control the CO_2 temperature and pressure at turboexpander inlet respectively. For controlling the thermal oil flow rate, two sensing parameters of CO_2 temperature and pressure at the turboexpander inlet are increased with higher thermal oil flow rate. Meanwhile, only one sensing parameter of CO_2 pressure at turboexpander inlet is increased with higher CO_2 mass flow rate and the other sensing parameter of CO_2 temperature at turboexpander is decreased.

7.6 Summary

This chapter overviewed the test facility of the T-CO_2 system with CO_2 turboexpander and plate-type gas generator. In addition, the section presents the preliminary test results on the performances of test rig and components at different heat source temperature and CO_2 mass flow rate. The measured and calculated turbine power generations and overall turbine efficiency all decreased with higher CO_2 mass flow rate. The tested overall efficiency proved to be small than its isentropic efficiency, indicating that the turbine mechanical and electrical efficiencies need to be further improved. At higher thermal oil mass flow rate, the measured and calculated power generations, turbine isentropic and overall efficiencies and gas generator heat capacity were all increased. The T-CO_2 fluid gas temperature and pressure at the CO_2 turboexpander inlet were found to be two important parameters which can be respectively controlled with heat source parameters and T-CO_2 liquid pump speed respectively.

Chapter 8 will present the thermodynamic analysis and comparison between R245fa ORC system and T-CO_2 system using low-grade thermal energy to produce useful shaft or electrical power. The cycle thermal and exergy efficiencies for both systems at different operating conditions will be calculated and compared.

Chapter 8 – THERMODYNAMIC ANALYSIS AND COMPARISON BETWEEN R245fa ORGANIC RANKINE CYCLES AND CO_2 TRANSCRITICAL POWER CYCLES

8.1 Introduction

In this chapter, a theoretical study is conducted to investigate and compare the performance of CO_2 transcritical power cycles (T-CO_2) and R245fa organic Rankine cycles (ORCs) using low-grade thermal energy to produce useful shaft or electrical power. Each power cycle consists of typical Rankine cycle components, such as a working fluid pump, gas generator or evaporator, turbine with electricity generator, air cooled condenser and recuperator (internal heat exchanger). The thermodynamic models of both cycles have been developed and are applied to calculate and compare the cycle thermal and exergy efficiencies at different operating conditions and control strategies. The predictions and analyses will contribute towards justifying the feasibility of applying T-CO_2 into low-grade power generation and further development in this area.

8.2 Systems Description

The system schematic diagrams to be analysed in this chapter are shown in Fig. 8.1. The only difference between Fig. 8.1 (a) and (b) is the presence or not of a recuperator in the system, which is used as an international heat exchanger to improve the performance of the system. The system components shown in Fig. 8.1 (a) include a liquid pump, gas generator/ evaporator, turbine/ expander with electricity generator and condenser. Operationally, the liquid working fluid from the condenser outlet is drawn into the pump (point 4) and thus pressurised to point 5. It then flows into the gas generator, where it absorbs heat from the heat source to be vaporised and superheated. The vapour working fluid with high pressure and high temperature then expands in the expander (point 1) to generate electric power through the electricity generator. After expansion (point 2), the low-temperature vapour enters the condenser where it is condensed into its liquid state (point 4). Finally, the working fluid flows back to the pump (point 4) and the cycle repeats. As shown in Fig. 8.1 (b), a recuperator can also be installed just after

the expander so as to desuperheat the fluid from the expander outlet and in the meantime preheat the liquid after the pump. The installation of a recuperator in the system in expected to reduce the heating and cooling demands from the heat source and sink respectively when the system power generation is specified.

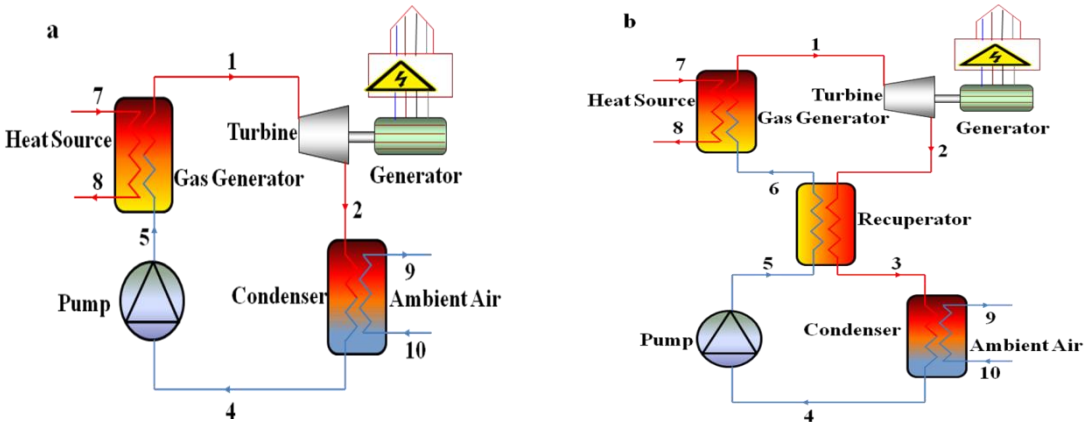

(a) Schematic diagram of T-CO_2/ R245fa ORC without recuperator

(b) Schematic diagram of T-CO_2/ R245fa ORC with recuperator

Figure 8.1 (a) Schematic diagram of T-CO_2/ R245fa ORC without recuperator. (b) Schematic diagram of T-CO_2/ R245fa ORC with recuperator.

Corresponding to Fig. 8.1 (b), sample T-S diagrams for the T-CO_2 and R245fa ORC systems are depicted in Fig. 8.2 (a) and (b) respectively. It should be noted that the T-S diagram for the T-CO_2 is based on the specifications of 12MPa and 5.729MPa for the supercritical gas generator and condenser pressures respectively. While for the T-S diagram of the R245fa ORC, the evaporator and condenser pressures are specified as 1.35MPa and 0.1224MPa each. Based on their operational pressure ranges, turboexpanders (turbines) can be used in T-CO_2 cycles while both turboexpanders (turbines) and scroll expanders are applicable for R245fa ORCs. In addition, for both systems, the heat source and sink temperatures are assigned as 160 ^{o}C and 10 ^{o}C individually. All state points in the diagrams are calculated by EES® (Engineering Equation Solver) (Klein, 2014).

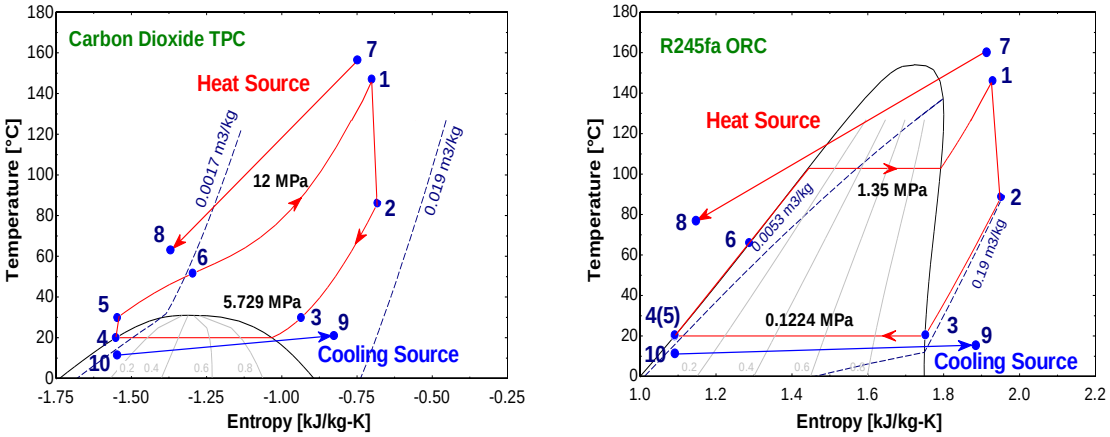

(a) T-S diagram of T-CO_2 (B) T-S diagram of R245fa ORC

Figure 8.2 (a) T-S diagram of T-CO_2. (b) T-S diagram of R245fa ORC

As depicted in Fig. 8.2, the working fluid temperature profiles in heat addition process of T-CO_2 matches well with the sensible heat source flow compared to the corresponding temperature profiles of R245fa ORC which has an obvious pinch point. It can be expected that at the same pinch point temperature difference and expander inlet temperature of heat addition processes, higher heat source temperature will be required for a R245fa ORC system.

8.3 Thermodynamic Models

8.3.1 Working fluid properties

Different working fluids can be used in low-grade power generation systems. However, the appropriate working fluids should reveal good thermophysical properties, none safety issues and less environmental impacts. Accordingly, in this chapter, the CO_2 and R245fa are selected and analysed in the transcritical and subcritical ORC power cycles respectively. Some relevant thermophysical safety and environmental data of CO_2 and R245fa are listed in Table 8.1 (Calm et al., 2011) based on ASHRAE 34 and REFPROP 9.0 such that the data accuracies are acceptable.

Table 8.1 Thermophysical safety and environmental data for CO_2 (R744) and R245fa.

Substance	Thermophysical data					
	Molecular mass	T_b	T_c	P_c	Vapor C_p	Latent heat L
	(g/mol)	(^oC)	(^oC)	(Mpa)	(J/kg K)	(kJ/kg)
CO_2 (R744)	44.01	-78.4	31.1	7.38	3643.72	167.53
R245fa	134.05	15.1	154	3.65	980.90	177.08
Substance	Safety data			Environmental data		
	OEL	LEL	ASHRAE safety group	ODP	GWP	Atmospheric
	(PPMv)	(%)	-	-	-	(yr)
CO_2 (R744)	5000	None	A1	0	1	>50
R245fa	300	None	B1	0	1030	7.6

8.3.2 Assumptions for the thermodynamic analysis

The following assumptions have been made for the analysis of each system and corresponding cycle:

(1) The system operates under steady state.

(2) The heat and friction losses, the kinetic and potential energy, as well as pressure drops of the working fluid through the system are neglected.

(3) The hot thermal oil is used as the heat source and the temperature difference between heat source and expander inlet is 20K; the thermal oil flow rate is 1.2kg/s.

(4) The ambient air is used as heat sink and the working fluid state at condenser outlet is saturated liquid which has a temperature of 10K higher than the incoming air flow; the air mass flow rate is 5kg/s.

(5) The isentropic efficiencies of the pump and the turbine are both set to 85% based on previous research outcomes (Kim, et al., 2012; Cayer, et al., 2009) while the effectiveness of recuperator is 0.8. It should be noted that the turbine isentropic efficiency is assumed based on T-CO_2. For an R245fa ORC when a scroll expander is applied, the isentropic efficiency could be lower (Quoilin, 2010). To fairly compare the system performances of T-CO_2 and R245fa ORC, the same isentropic efficiency is assumed in this chapter.

(6) The dead state pressure and temperature are 1bar (atmospheric pressure) and ambient air respectively for exergy analysis.

(7) The design power generation from expander is 5kW.

8.3.3 Energy calculations

The purpose of energy analysis is to evaluate system performance based on the first law of thermodynamics in term of thermal efficiency which can be calculated as Eq. 8.1.

$$\eta_{th} = \frac{\dot{W}_{net}}{\dot{Q}_{gg}} \tag{8.1}$$

where the $\dot{W}_{net}$ and $\dot{Q}_{gg}$ are system net power output and heat input to gas generator or evaporator respectively. To obtain these two performance parameters, energy balance calculation for each system component is necessary.

(i) Gas generator or evaporator

The heat capacity:

$$\dot{Q}_{gg} = \dot{m}_f(h_1 - h_5) = \dot{m}_{oil}(T_7 - T_8), \quad \text{for system without recuperator} \tag{8.2}$$

$$\dot{Q}_{gg} = \dot{m}_f(h_1 - h_6) = \dot{m}_{oil}(T_7 - T_8), \quad \text{for system with recuperator} \tag{8.3}$$

(ii) Expander

The power output:

$$\dot{W}_{exp} = \dot{m}_f(h_1 - h_2) \tag{8.4}$$

The isentropic efficiency:

$$\eta_{exp} = \frac{h_1 - h_2}{h_1 - h_{2,is}} \tag{8.5}$$

(iii) Recuperator

The effectiveness:

$$\varepsilon_{rec} = \frac{h_2 - h_3}{q_{rec,max}} = \frac{h_2 - h_3}{h_2 - h_{3,min}} \tag{8.6}$$

where $h_{3,min}$ is calculated based on the temperature at point 5 and pressure at point 3.

The heat capacity:

$$\dot{Q}_{rec} = \dot{m}_f(h_2 - h_3) = \dot{m}_f(h_6 - h_5) \tag{8.7}$$

(iv) Condenser

The heat capacity:

$$\dot{Q}_{cd} = \dot{m}_f(h_2 - h_4) = \dot{m}_a(T_9 - T_{10}),$$
for system without recuperator (8.8)

$$\dot{Q}_{cd} = \dot{m}_f(h_3 - h_4) = \dot{m}_a(T_9 - T_{10}),$$
for system with recuperator (8.9)

(v) Pump

The power input:

$$\dot{W}_{pump} = \dot{m}_f(h_5 - h_4) \tag{8.10}$$

The isentropic efficiency:

$$\eta_{pump} = \frac{h_{5,is} - h_4}{h_5 - h_4} \tag{8.11}$$

(vi) The net power output

$$W_{net} = \dot{W}_{exp} - \dot{W}_{pump} \tag{8.12}$$

8.3.4 Exergy calculations

The thermal efficiency alone however is not enough to evaluated and characterize the quality of system components such as heat exchangers. To achieve these, exergetic analysis based on the second law of thermodynamic is required (Dai et al., 2009; Wang et al., 2013; Baral et al., 2015). The exegetic analysis is necessary to understand the extent of irreversibility in each component process, identify where the most irreversibility is and therefore the potential of improvements. The component exergy destructions of both T-CO_2 and R245fa ORC systems are calculated as below:

(i) Gas generator or evaporator

$$I_{gg} = \dot{m}_f T_0 \left(s_1 - s_5 - \frac{q_{gg}}{\bar{T}_{source}}\right) = \dot{m}_f T_0 \left(s_1 - s_5 - \frac{h_1 - h_5}{\bar{T}_{source}}\right), \quad (8.13)$$

for system without recuperator

$$I_{gg} = \dot{m}_f T_0 \left(s_1 - s_6 - \frac{q_{gg}}{\bar{T}_{source}}\right) = \dot{m}_f T_0 \left(s_1 - s_6 - \frac{h_1 - h_6}{\bar{T}_{source}}\right), \quad (8.14)$$

for system with recuperator

(ii) Expander:

$$I_{exp} = \dot{m}_f T_0 (s_2 - s_1) \quad (8.15)$$

(iii) Recuperator

$$I_{rec} = \dot{m}_f T_0 (s_6 + s_3 - s_5 - s_2) \quad (8.16)$$

(iv) Condenser

$$I_{cd} = \dot{m}_f T_0 \left(s_4 - s_2 + \frac{q_{cd}}{\bar{T}_{sink}}\right) = \dot{m}_f T_0 \left(s_4 - s_2 + \frac{h_2 - h_4}{\bar{T}_{sink}}\right), \quad (8.17)$$

for system without recuperator

$$I_{cd} = \dot{m}_f T_0 \left(s_4 - s_3 + \frac{q_{cd}}{\bar{T}_{sink}}\right) = \dot{m}_f T_0 \left(s_4 - s_3 + \frac{h_3 - h_4}{\bar{T}_{sink}}\right), \quad \text{for system with recuperator} \tag{8.18}$$

(v) Pump

$$I_{pump} = \dot{m}_f T_0 (s_5 - s_4) \tag{8.19}$$

The total exergy destruction:

$$\Sigma I_{tot} = I_{gg} + I_{exp} + I_{cd} + I_{pump}, \quad \text{for system without recuperator} \tag{8.20}$$

$$\Sigma I_{tot} = I_{gg} + I_{exp} + I_{rec} + I_{cd} + I_{pump}, \quad \text{for system with recuperator} \tag{8.21}$$

The system exergy input:

$$E_{in} = \Sigma I_{tot} + \dot{W}_{net} \tag{8.22}$$

The system exergy efficiency:

$$\eta_{exg} = \frac{\dot{W}_{net}}{E_{in}} \tag{8.23}$$

8.4 Performance Evaluation, Comparison and Analysis

In order to conduct performance comparison between the T-CO_2 and R245fa ORC, the developed thermodynamic models are simulated at specific operating conditions and control strategies. These include different heat source and sink temperatures varying in a range of 120-260 ^{o}C and 0-20 ^{o}C, respectively. These specifications are reasonable since the heat source temperatures are applicable for most of low grade heat sources (Tchanche et al., 2011) and the ambient air is used as heat sink for these power cycles to be analysed. For the working fluid pressures in heat addition process of gas generators

or evaporators, they vary in a range of 80-300bar and 8-22bar for T-CO_2 and R245fa ORC systems respectively. These pressure ranges can represent the applicable operating conditions for both power cycles. In addition, to facilitate the system applications, a recuperator is an option to be applied into each power cycle for the model simulation and comparison.

8.4.1 Thermal efficiency analysis

At constant CO_2 expander inlet pressure (120bar), the variations of system thermal efficiencies with heat source and sink temperatures for the T-CO_2 with and without recuperator are shown in Fig. 8.3. The simulation results show that at a constant heat source temperature, the thermal efficiency increases with lower heat sink temperature for both systems with and without recuperator. This can be explained that the lower heat sink temperature causes increased expander pressure ratio and thus power output or less required working fluid mass flow rate when the power output is fixed. The smaller working fluid mass flow rate indicates that the less heat source heat input is required and therefore higher thermal efficiency can be achieved. Simultaneously, at a constant heat sink temperature, the thermal efficiency rises with higher heat source temperature. However, the effect of heat source temperature on the thermal efficiency is more sensitive for the system with recuperator. When comparing the system performance with and without recuperator, at the same operating condition, the thermal efficiency is always higher for the system with recuperator.

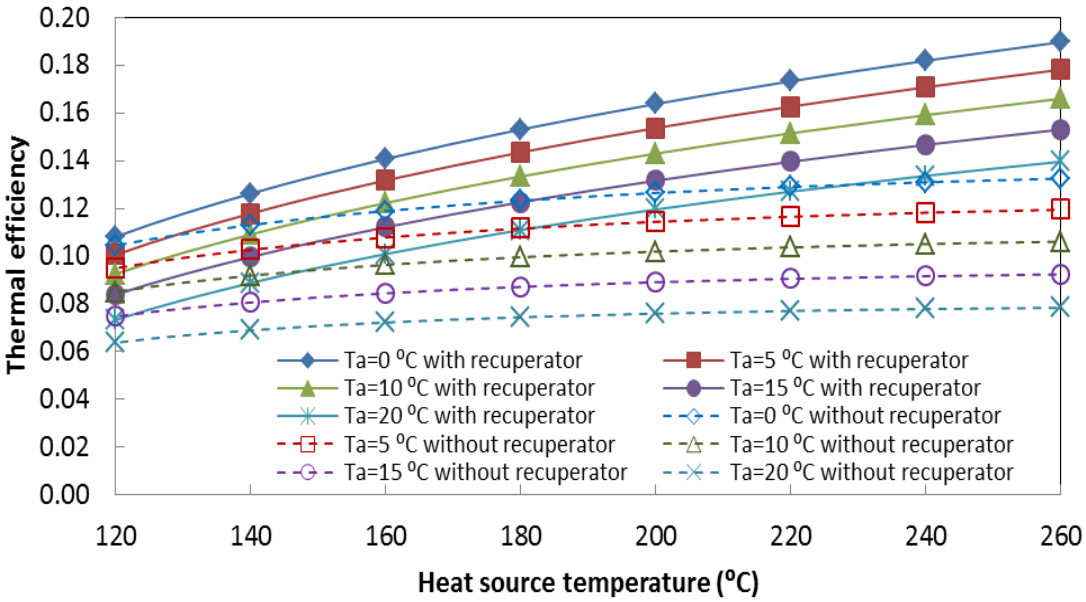

Figure 8.3 Variations of thermal efficiencies with heat source and sink temperatures for T-CO_2.

At a constant evaporator pressure (14bar), the variation of thermal efficiencies with heat source and sink temperatures for the R245fa ORC systems with and without recuperator are also simulated and depicted in Fig. 8.4. Similar to the T-CO_2 cycles, at a constant heat source temperature the thermal efficiency increases with lower heat sink temperature for the cycles with and without recuperator considering of its effect on expander pressure ratio. On the other hand, at a fixed heat sink temperature, the thermal efficiency increases with higher heat source temperature for the system with recuperator but decreases with increased heat source temperature for the cycle without recuperator. This demonstrates that an installation of recuperator in an R245fa ORC can benefit the system performance in term of thermal efficiency with higher heat source temperature.

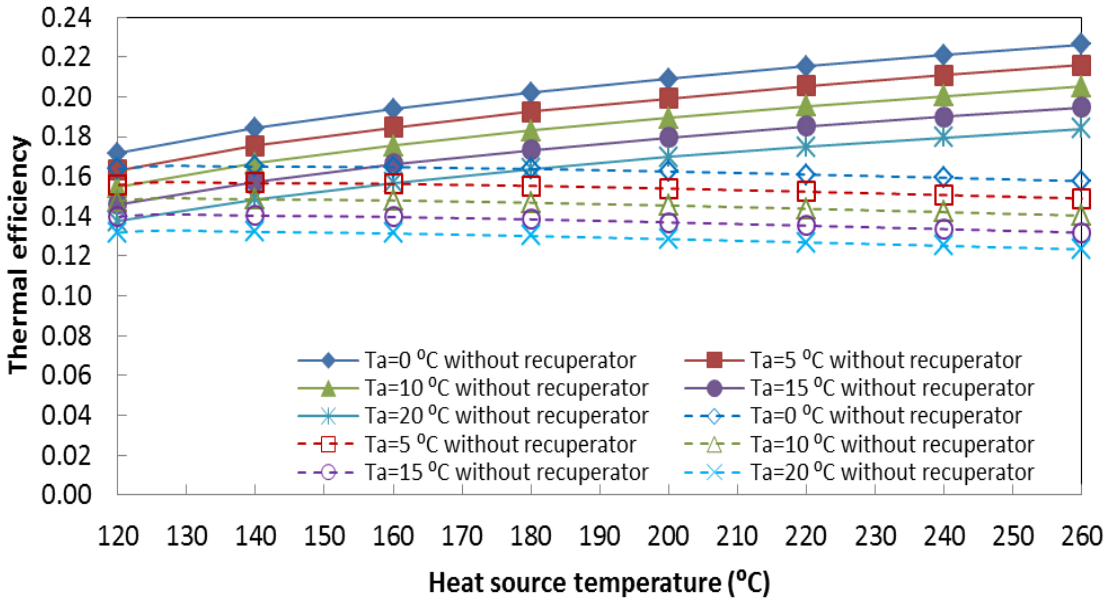

Figure 8.4 Variations of thermal efficiencies with heat source and sink temperatures for R245fa ORC.

To compare the performance of both T-CO_2 and R245fa ORC systems, at the same operating conditions of heat source and sink, the thermal efficiency of R245fa ORC is generally higher than that of T-CO_2. This is also based on the assumptions made in Section 8.3.2 for these two power cycles.

At constant heat sink temperature (10 ^{o}C), the variations of thermal efficiencies with heat source temperatures and CO_2 pressures at expander inlet are predicted and shown in Fig. 8.5 for the T-CO_2 systems with and without recuperator. It is seen that at a constant CO_2 pressure, the thermal efficiency increase with higher heat source temperature no matter if a recuperator is installed. On the other hand, at a constant heat source temperature, when the CO_2 pressure increases the thermal efficiency of both cycles (with and without recuperator) increases first, reaches to its peak value and then drops. This demonstrates that there is an optimum operating CO_2 pressure at expander inlet for the T-CO_2 cycles at fixed heat source and sink temperatures. For the effect of recuperator installation, the thermal efficiency of the cycle with recuperator is not always higher than that without recuperator at different CO_2 pressures which depends also on the heat source temperature. When the heat source temperature is less than about 180 ^{o}C, the thermal efficiency for the cycle with recuperator is even lower than that without recuperator when the CO_2 pressure increases further.

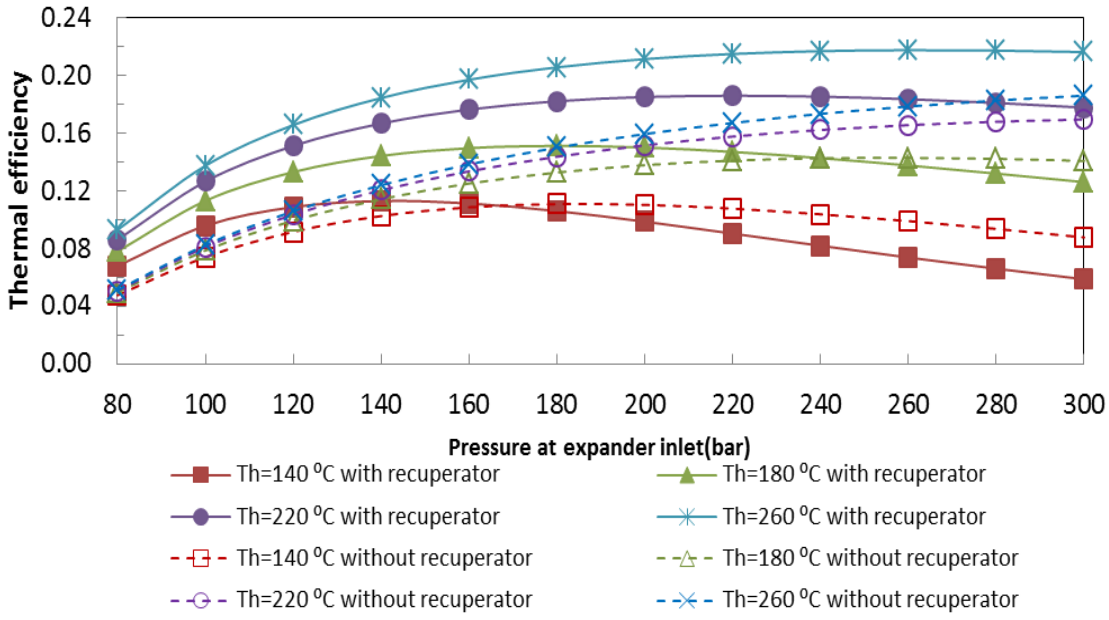

Figure 8.5 Variations of thermal efficiencies with heat source temperatures and working fluid pressures at expander inlet for T-CO_2.

For the effect of R245fa pressure at expander inlet as shown in Fig. 8.6, again at a constant R245fa pressure, the thermal efficiency increases with higher heat source temperature for the system with recuperator but mostly decreases with increased heat source temperature if a recuperator is not installed. Even so, the effect of heat source temperature on the thermal efficiency for the cycle without recuperator is not as significant as that with recuperator. Furthermore, different from the T-CO_2 systems, at a specified operating state, the thermal efficiency for the R245fa ORC system with recuperator is always higher than that without recuperator.

Due to the comparative study of the CO_2 based transcritical Rankine cycle and R245fa based subcritical Rankine cycle with the model previously described and the different thermodynamic parameters between CO_2 and R245fa, there is an optimum pressure at expander inlet for the thermal efficiency of T-CO_2 system and not for R245fa system at low heat source temperature.

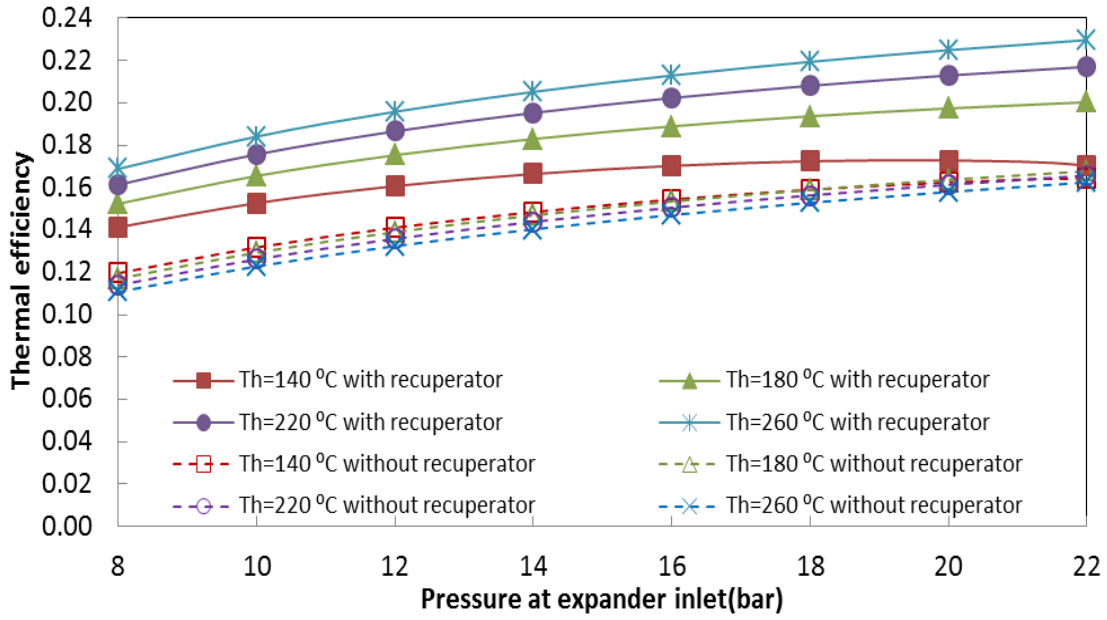

Figure 8.6 Variations of thermal efficiencies with heat source temperatures and working fluid pressures at expander inlet for R245fa ORC.

8.4.2 Exergy efficiency analysis

At a constant CO_2 expander inlet pressure (120bar), the variations of exergy efficiencies with heat source and sink temperatures for the T-CO_2 system with and without recuperator are also calculated and depicted in Fig. 8.7. Similar to the thermal efficiencies, at a constant heat source temperature, the exergy efficiency increases with lower heat sink temperature for both cycles with and without recuperator. On the other hand, at a constant heat sink temperature, the effect of heat source temperature on the exergy efficiency is insignificant for the system with recuperator. Alternatively, when a recuperator is not installed, the system exergy efficiency decreases with higher heat source temperature. Therefore, considering of its effect on the thermal efficiency, the higher heat source temperature is more preferable for the T-CO_2 system with recuperator than the one without recuperator.

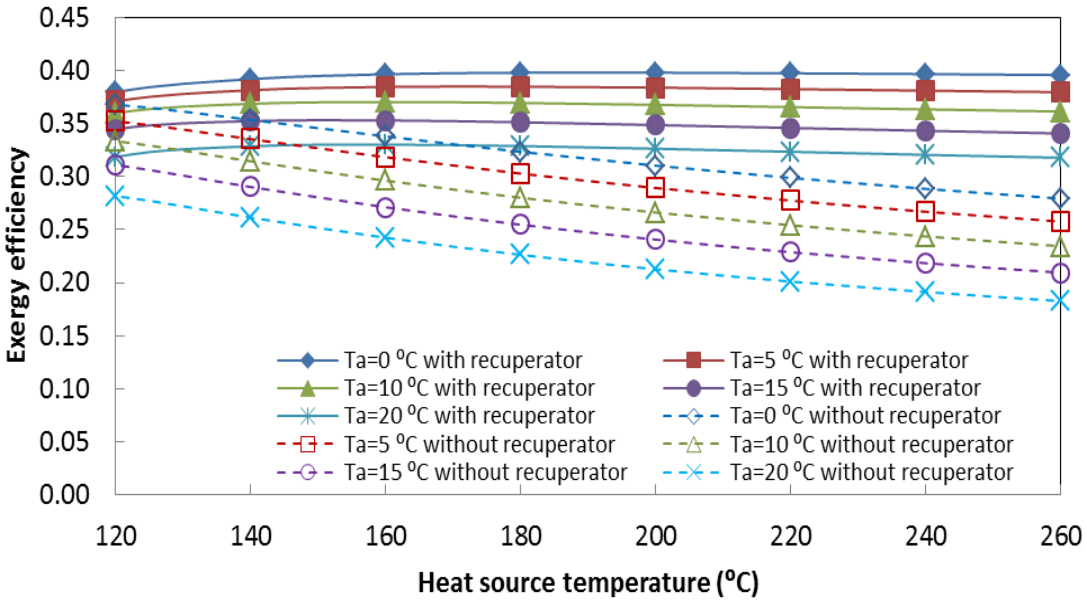

Figure 8.7 Variations of exergy efficiencies with heat source and sink temperatures for T-CO_2.

For the R245fa ORC as shown in Fig. 8.8, at a constant evaporator pressure (14bar), at a constant heat source temperature the exergy efficiency increases with lower heat sink temperature no matter if a recuperator is installed in the system. However, at a fixed heat sink temperature, the exergy efficiency decreases with higher heat source temperature irrespective of the recuperator installation. Therefore, it is understood that there is a compromise for the utilisation of high heat source temperature in a R245fa ORC system with recuperator. Alternatively, both thermal and exergy efficiencies cannot be improved with higher heat source temperature for the system without recuperator.

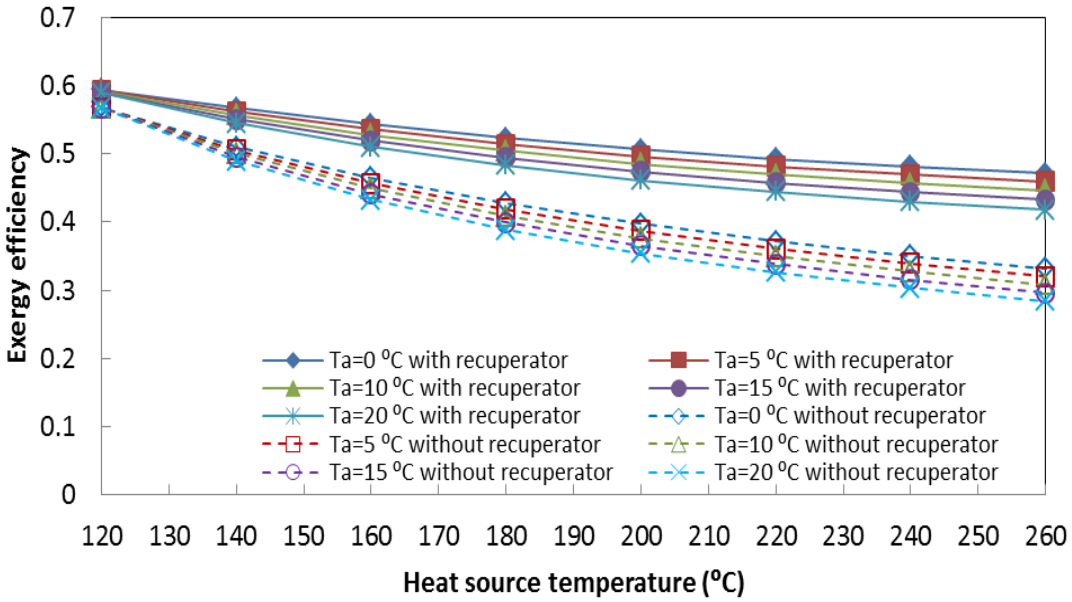

Figure 8.8 Variations of exergy efficiencies with heat source and sink temperatures for R245fa ORC.

At a constant heat sink temperature (10 °C), the variations of exergy efficiencies with heat source temperatures and CO_2 expander inlet pressures for the cycles with and without recuperator are predicted and shown in Fig. 8.9. For both cycles with and without recuperator, at a constant heat source temperature, the exergy efficiency increases firstly with higher CO_2 expander inlet pressure and then decreases. This indicates that there is an optimal CO_2 high side pressure where the exergy efficiency can be maximised for both cycles when heat source and sink conditions are fixed. However, at the same conditions, the optimal pressure for the cycle with recuperator is much less than that without recuperator. On the other hand, at a constant CO_2 high side pressure, the exergy efficiency decreases with higher heat source temperature if the CO_2 pressure is less than a specific value for each cycle (about 120 bar for the cycle with recuperator, much higher for the system without recuperator), otherwise will increase with higher heat source temperature. In addition, the exergy efficiencies for both cycles are higher for the system with recuperator if the CO_2 pressure is not too high.

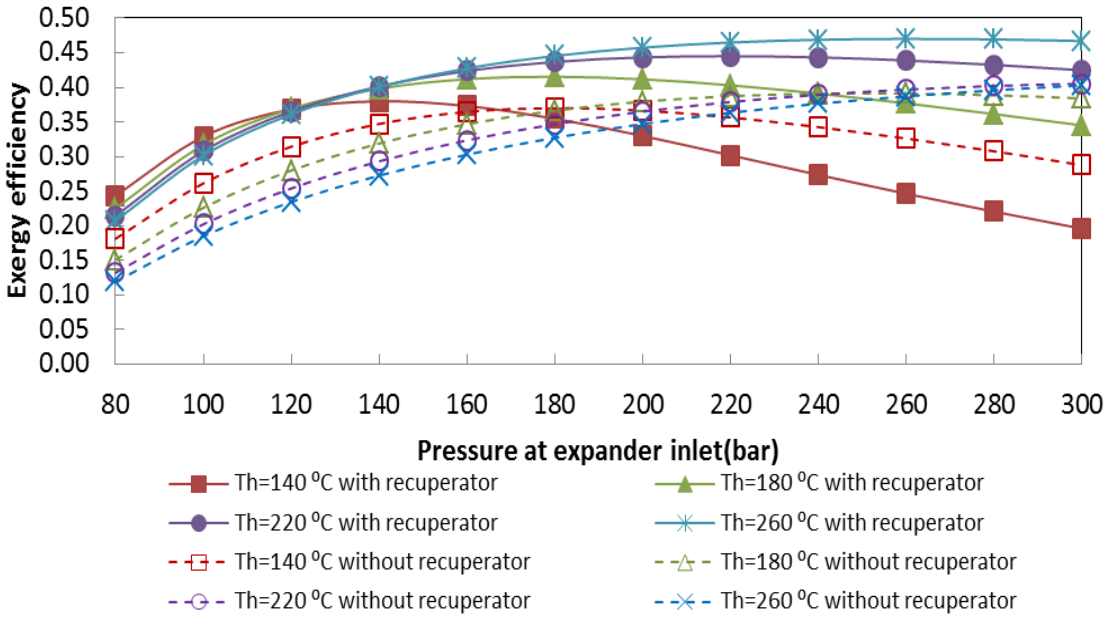

Figure 8.9 Variations of exergy efficiencies with heat source temperatures and working fluid pressures at expander inlet for T-CO_2.

The effect of expander inlet pressure on the exergy efficiency of R245fa ORC is a bit different, as shown in Fig. 8.10. At a constant heat sink temperature (10 ^{o}C), when the heat source temperature is fixed, the exergy efficiency for both cycles with and without recuperator increases mostly with higher R245fa pressure at expander inlet. Within the operating high side pressure range, the optimal pressure is only detected when the heat source temperature is not too high (140 ^{o}C) for the cycle with recuperator. In addition, at a fixed R245fa expander inlet pressure, the exergy efficiency decreases with higher heat source temperature. In general, at the same operating condition, the exergy efficiency of the cycle with recuperator is higher than that without recuperator.

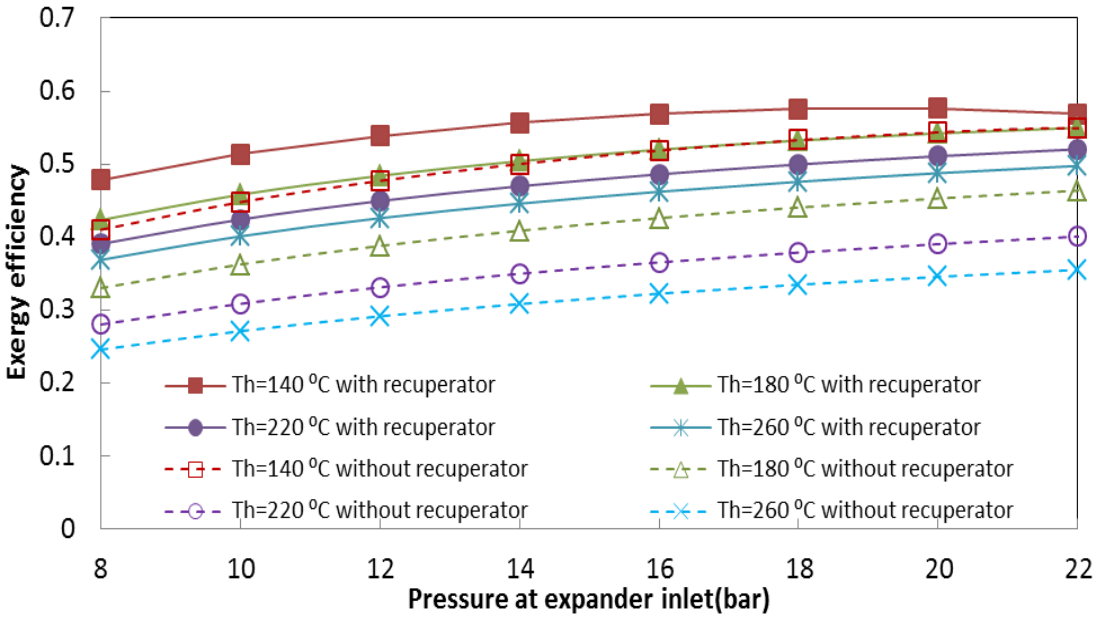

Figure 8.10 Variations of exergy efficiencies with heat source temperatures and working fluid pressures at expander inlet for R245fa ORC.

The exergy destruction rate is defined as the exergy destruction of each component over the total system exergy destruction, which is helpful to evaluated and identify the system components with significant exergy destruction rates. At constant het sink temperature (10 ^{o}C), constant expander inlet pressure (120 bar for T-CO_2 and 14bar for R245fa ORC) and varied heat source temperature, these exergy destruction rates are therefore calculated and depicted in Fig. 8.11 and 8.12 respectively for T-CO_2 and R245fa ORC. For the T-CO_2, the exergy destructions of most components decrease with higher heat source temperature except for the recuperator for the cycle with recuperator and the condenser for the system without recuperator. In addition, at a specified operating state, for both T-CO_2 systems, the gas generator has the most exergy destruction rate while the liquid pump has the least exergy destruction rate. As shown in Fig. 8.12, although the magnitudes of component exergy destruction rates for the R245fa ORC are different from those in T-CO_2 cycles, the trends are quite similar. The component of evaporator has the maximum exergy destruction rate while the liquid pump has the least exergy destruction rate. Subsequently, more efforts are necessary to optimise the design of heat source heat exchangers for the power generation systems and cycles to maximise the component and system performance.

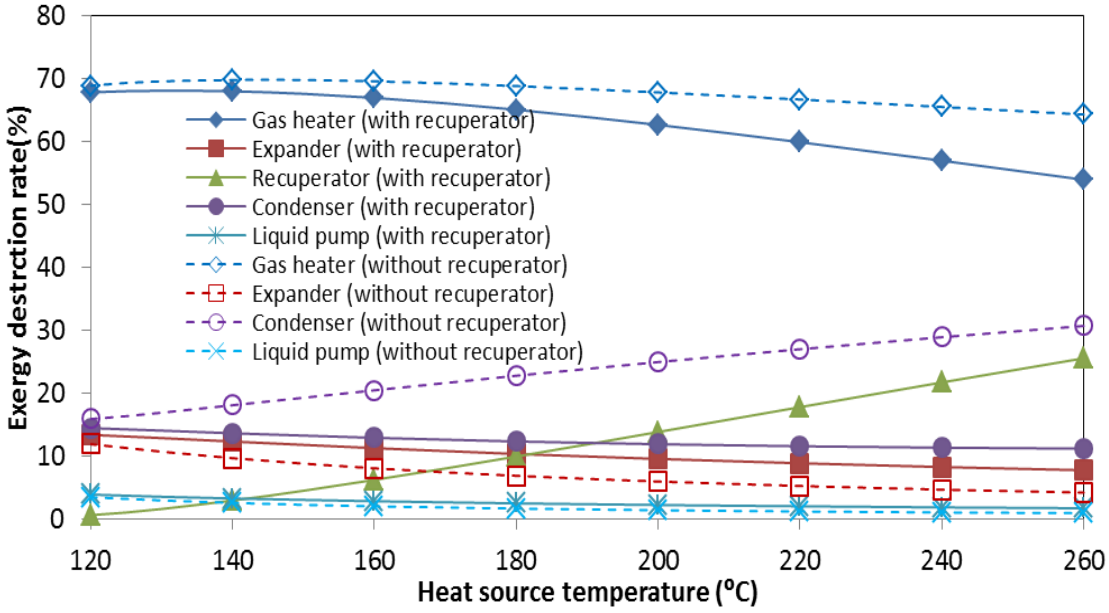

Figure 8.11 Variations of component exergy destruction rates with heat source temperature for T-CO_2.

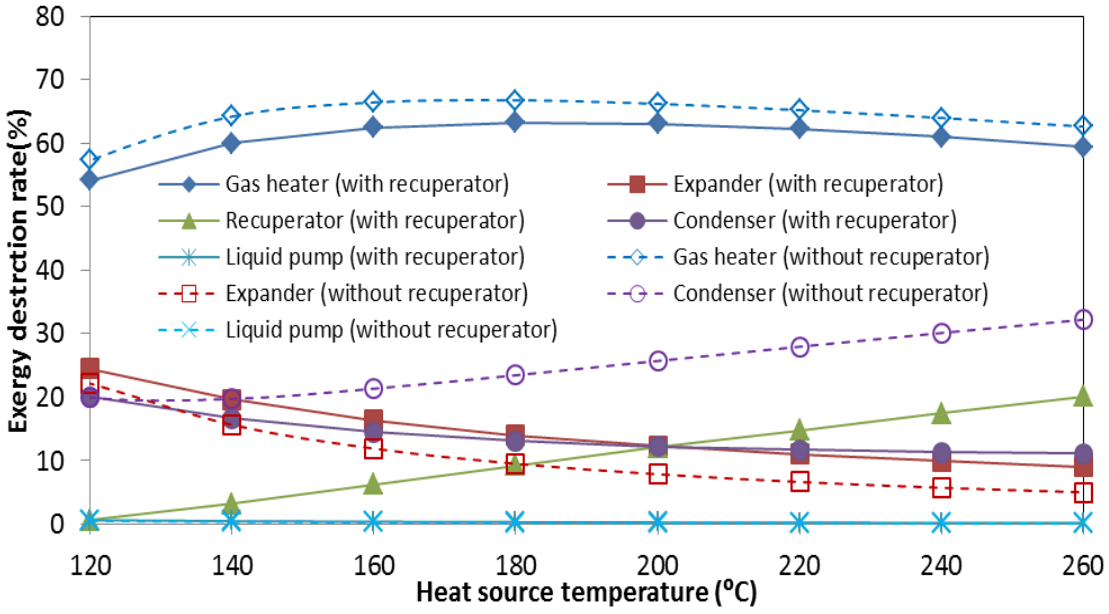

Figure 8.12 Variations of component exergy destruction rates with heat source temperatures for R245fa ORC.

8.5 Summary

The simulation results of this chapter show that the system performances for both cycles vary with different operating conditions. When the heat source (waste heat) temperature increases from 120 °C to 260 °C and heat sink (cooling air) temperature is reduced from

20 ^{o}C to 0^{o}C, both thermal efficiencies of R245fa ORC and T-CO_2 with recuperator can significantly increase. On the other hand, R245fa ORC and T-CO_2 exergy efficiencies increase with lower heat sink temperatures and generally decrease with higher heat source temperatures. In addition, with the same operating conditions and heat transfer assumptions, the thermal and exergy efficiencies of R245fa ORCs are both slightly higher than those of T-CO_2. However, the efficiencies of both cycles can be enhanced by installing a recuperator in each system at specified operating conditions. Ultimately, optimal operating states can be predicted, with particular focus on the working fluid expander inlet pressure for both cycles.

Chapter 9 will summarise the results and contributions of the investigations in this study and will provide some recommendations for future work.

Chapter 9 – CONCLUSIONS AND RECOMMENDATIONS FOR FUTURE WORK

With the growing demand for more sustainable power generation sources, small-scale ORC systems can greatly benefit the low-grade industry waste heat recovery applications. In addition, a transcritical CO_2 power cycle (T-CO_2) is a prospective option for low temperature heat source power generation, considering its natural working fluid properties and low environmental impacts compared to the conventional ORC systems currently in use. However, further investigations are required to assess the operations, controls and optimisations of both the systems.

In this thesis, the experimental and theoretical investigation of a small-scale ORC system and T-CO_2 system for low-grade heat to power energy conversion were carried out. The findings from the above research project and recommendations for the future work are shown below.

9.1 Basic R245fa ORC system with turbine

The thesis presents experimental results on the effects of two important operating parameters, heat source temperature and ORC liquid pump speed, on the performance of a small-scale low-grade R245fa ORC system. Several useful research outcomes have been obtained. These include:

- At higher heat source temperatures, the temperature of the heat source outlet, turbine inlet and outlet and condenser inlet all increased differently but the temperatures of the condenser outlet or pump inlet and pump outlet did not change much. In addition, all the cycle point pressures and the pressure ratio of turbine inlet and outlet increased at higher heat source temperatures.
- At higher heat source temperatures, the turbine power output, ORC pump power input, evaporator heat input, condenser heat output, turbine isentropic and overall efficiencies and system thermal efficiency all increased.

- At higher ORC pump speeds, the temperatures of thermal oil outlet, turbine inlet, turbine outlet and condenser inlet all decreased but the ORC mass flow rate, ORC temperatures at condenser outlet and pump outlet were all increased. In addition, all cycle point pressures were increased but the pressure ratio of turbine inlet and outlet was decreased.
- At higher ORC pump speeds, the turbine power output, ORC pump power input, evaporator heat input, condenser heat output and turbine overall efficiency all increased but the turbine isentropic efficiency decreased. There was an optimal ORC pump speed to obtain a maximum system thermal efficiency.

Furthermore, the ORC fluid superheat and pressure at the turbine inlet were found to be two important parameters, which could be respectively controlled with heat source temperature and ORC pump speed.

9.2 R245fa ORC system with recuperator and turbine

In addition, in this thesis, the utilisation of industry waste heat by means of the small scale R245fa ORC system with recuperator was experimentally studied. The effects of three important operating parameters, heat source temperature, ORC pump speed and ambient air velocity of air-cooled condenser, on the performance of the system were assessed and evaluated. Also, the comparisons of experimental results on the effect of heat source temperature and ORC pump speed between the recuperative ORC system and basic ORC system were investigated. In light of the experimental data analysis, the following conclusions are drawn:

- For system with recuperator, the temperatures of heat source outlet, turbine inlet and outlet and evaporator inlet experienced an increase along with higher heat source temperature. However, the temperatures of condenser inlet and outlet, pump outlet did not change much. For system without recuperator, the changes in temperature of evaporator and condenser inlets were exactly opposite. In addition, the cycle point pressures and the pressure ratios of turbine inlet and outlet on both systems increased with higher heat source temperatures. The pressure ratios of the turbine in the system with recuperator were much lower than in the system without.

- For system with recuperator, the turbine power outlet, ORC pump power input, evaporator heat input, condenser heat output, turbine isentropic and overall efficiencies and system thermal and overall efficiencies of both the systems increased along with higher heat source temperature. However, compared to the system without recuperator, the system with recuperator need much higher heat source temperatures.
- At higher ORC pump speeds for system with recuperator, the temperatures of thermal oil outlet, turbine inlet and outlet, and evaporator inlet all experienced a decrease, but the temperatures at condenser inlet and outlet, and pump outlet experienced an increase. In contrast, the changes in temperatures of evaporator and condenser inlets on system without recuperator were exactly opposite. In addition, the ORC mass flow rate and cycle point pressures all increased with higher ORC pump speeds, but the pressure ratios of turbine inlet and outlet were decreased in both systems.
- At higher ORC pump speeds for system with recuperator, the ORC pump power input, condenser heat output, evaporator heat input and turbine overall efficiency experienced an increase, but the turbine power output, turbine isentropic efficiency and system thermal and overall efficiencies experienced a decrease. Majority of the parameters were lower than the system without recuperator. Due to a larger pressure drop and a higher pressure in low-pressure category in the system with recuperator, the pressure ratio was much lower compared to the system without recuperator.
- At higher ambient air velocity in system with recuperator, the ORC temperatures of condenser inlet and outlet, and pump outlet experienced a decrease while the temperatures of turbine inlet and outlet, and evaporator inlet experienced an increase. In addition, all the cycle point pressures decreased with higher ambient air velocity, however, the pressure ratio of turbine inlet and outlet increased.
- With higher ambient air velocity in system with recuperator, the turbine power output, turbine isentropic and overall efficiencies and system thermal and overall efficiencies increased alongside.

Furthermore, the ORC working fluid superheat temperature and pressure at the turbine inlet were found to be important system parameters that could be controlled by heat

source temperature and ORC pump speed respectively in system with recuperator. In addition, the turbine outlet pressure was a primary parameter in determining the tendencies of pressure ratio of turbine inlet and outlet, which could be adjusted by the ambient air velocity of the recuperative ORC system.

9.3 R245fa ORC system with scroll expander, and plate-type evaporator or shell and tube evaporator

The thesis also discusses the experimental investigation of the scroll expander and various evaporators integrated into an R245fa ORC system with or without recuperator. Several useful research outcomes have been obtained from the experimental study.

- The system could operate at a large range of expander pressure ratios contributed by different evaporators used in which the system with shell and tube evaporator operated at lower range of pressure ratio while the system with plate evaporator could work at larger range of pressure ratio.
- It is seen from the measurements that the expander power generation increases polynomially with higher pressure ratio while the expander overall efficiency increases with higher pressure ratio if it is not too high and decreases if the pressure ratio growths further. This indicates that there is an optimal pressure ratio to maximise the expander overall efficiency.
- In addition, the system overall efficiency also increase polynomially with higher pressure ratio and it can be greatly improved when a recuperator is employed irrespectively of the type of evaporator employed. The benefit of system performance from the recuperator integration is due to its contribution to the reduction of required evaporator heat capacity.
- On the other hand, for a fixed system structure and component composition, both expander power generation and system overall efficiencies increase with higher evaporator heat capacity. But if the heat capacity is not quite high, the power generation and system overall efficiency are both higher when a plate evaporator and recuperator are employed compared to those with a shell and tube evaporator and recuperator.

- The temperature difference of the evaporators increased with higher heat source temperature. The temperature difference of shell and tube evaporator was much higher than the temperature difference of plate-type evaporator. Thus, the temperature transfer efficiency of plate-type evaporator is higher than the shell and tube evaporator.
- The pinch point temperatures of both evaporators in the system without recuperator were higher than the system with. In addition, the pinch point temperatures of the shell and tube evaporator were much higher than the plate-type evaporator in the system with and without recuperator.

9.4 Basic T-CO_2 system with turbine

A small-scale test rig of the T-CO_2 system was developed and tested to investigate the effects of two important operating parameters including heat source mass flow rate and CO_2 mass flow rate on system performance.

- Preliminary test results showed that the CO_2 mass flow rate could be directly controlled by variable CO_2 liquid pump speeds. The CO_2 pressures at the turbine inlet and outlet, and pump inlet and outlet all increased with higher CO_2 mass flow rate. On the other hand, the CO_2 temperatures at the turbine inlet and outlet, CO_2 gas generator outlet and condenser inlet all decreased with higher CO_2 mass flow rate.
- At higher CO_2 mass flow rate, the measured and calculated turbine power generations and overall turbine efficiency all increased. In addition, the tested turbine overall efficiency proved to be smaller than its isentropic efficiency, indicating that the turbine's mechanical and electrical efficiencies need to be further improved.
- For higher thermal oil mass flow rate, the CO_2 pressures of turbine inlet and outlet, and pump inlet and outlet were all increased. At higher thermal oil mass flow rate, the CO_2 temperatures of turbine inlet and outlet, condenser inlet, gas generator outlet all increased differently but the temperatures of the gas generator inlet, condenser outlet did not changed much.

- At higher thermal oil mass flow rate, the measured and calculated power generations, turbine isentropic and overall efficiencies and gas generator heat capacity were all increased.

Furthermore, the CO_2 temperature and pressure at the turbine inlet are two important parameters which can be efficiently controlled by both thermal oil flow rate and CO_2 mass flow rate based on measurements.

9.5 Thermodynamic analysis and comparison between R245fa ORCs and T-CO_2 systems

CO_2 and R245fa have both been acknowledged as applicable working fluids in low temperature (120 – 260 ^oC) power generation systems in terms of their thermophysical properties and safety data. However, use of CO_2 as the working fluid is more promising due to its negligible global warming potential regardless of its high operating pressure. In regards to their application in low temperature power generation, CO_2 will inevitably work in supercritical power cycles such as T-CO_2 considering its low critical temperature. Meanwhile, R245fa will most likely be effective in an organic Rankine cycle (ORC) due to its relatively high critical temperature. There are essential components required for both T-CO_2 and R245fa ORC systems and the installation of a recuperator is an option for each cycle. This study has comprehensively evaluated, compared and analysed the performances of these two power cycles with the following outcomes:

- For the T-CO_2 system, installing a recuperator is preferable and there is an optimal CO_2 expander inlet pressure for constant heat source and sink parameters where either the thermal or the exergy efficiency is maximised. Ideally, the system with recuperator can operate at a higher expander inlet pressure (>120bar), higher heat source temperature and low heat sink temperature.
- For the R245fa ORC system, installing a recuperator can also be beneficial. There is an optimal R245fa expander inlet pressure for constant heat source and sink parameters where either the thermal or the exergy efficiency is maximised but this is only available for lower heat source temperatures. The system with

recuperator can preferably operate at a higher expander inlet pressure and lower heat sink temperature. There is a compromised selection for the heat source temperature considering its contrary effect on thermal and exergy efficiencies.

- From exergetic analysis for both T-CO_2 and R245fa ORC systems, the heat source heat exchanger have the most exergy destruction, closely followed by condenser, expander and recuperator; this requires greater attention when optimising component designs and controls.
- Based on the assumptions in this chapter, the thermal and exergy efficiencies of the T-CO_2 system are generally lower than those of the R245fa ORC. Further detailed heat transfer analysis and experimental investigation on the heat source and sink heat exchangers are necessary in future to explore the potential of both the system scenarios. In addition, future work may include the utilisation of a mixture working fluid of CO_2 and HFC in a low-grade power generation system to enhance the system performance and minimise the environmental impact.

9.6 Recommendations for future work

The experimental and theoretical investigations for R245fa ORC system and T-CO_2 system mainly focused on the impact factors of the system performances. The detailed optimisation of the individual components (e.g. turbine and scroll expander) and the control system enabled development of the proposed test rigs.

As the key component of the ORC and T-CO_2 systems, expansion machines are still working at lower efficiencies in both systems. The mechanical and electrical efficiencies of R245fa turbine and CO_2 turbine need to be optimised. In addition, the air cooled condensers were used into both systems. The comparison between the air cooled condenser and water cooled condenser need to be carried out as well.

Regarding the thermodynamic analysis of this study, although providing validated results from the simulation, there are further improvements possible for the detailed module for each component. The component modules can be validated using the test results obtained from this project. Such models can be developed in software such as MATLAB or TRNSYS in the next step.

T-CO_2 system and its components are still in early stages of development and further research and optimisation are still required at the moment. The design and simulations for both systems and components will play a key role in the optimisation of Rankine technologies in near further.

REFERENCES

ASHRAE Standard 15, 2007, “Safety standard for refrigeration system”. ASHRAE, Inc., Atlanta, 36 pgs.

Badr, O., Probert, S.D. & O'Callaghan, P.W. 1985, “Selecting a working fluid for a Rankine-cycle engine”, *Applied Energy*, vol. 21, no. 1, pp. 1-42.

Bao, J. & Zhao, L. 2013, “A review of working fluid and expander selections for organic Rankine cycle”, *Renewable and Sustainable Energy Reviews*, vol. 24, pp. 325-342.

Baral, S., Kim, D., Yun, E. & Kim, K. 2015, “Energy, Exergy and Performance Analysis of Small-Scale Organic Rankine Cycle Systems for Electrical Power Generation Applicable in Rural Areas of Developing Countries”, *ENERGIES*, vol. 8, no. 2, pp. 684-713.

Barigozzi, G., Perdichizzi, A. & Ravelli, S. 2011, "Wet and dry cooling systems optimization applied to a modern waste-to-energy cogeneration heat and power plant", *Applied Energy*, vol. 88, no. 4, pp. 1366-1376.

Berrada, N., Marvillet, C., Bontemps, A. & Daoudi, S. 1996, "Heat transfer in-tube condensation of a zeotropic mixture of HFC23/HFC 134a in a horizontal smooth tube", *INTERNATIONAL JOURNAL OF REFRIGERATION-REVUE INTERNATIONALE DU FROID*, vol. 19, no. 7, pp. 463-472.

Calm, J.M. and Hourahan G.C. 2011, “Physical, safety, and environmental data for current and alternative refrigerants”, in: *Proceddings of the 23rd International Congress of Refrigeration*, Prague, Czech Republic, ICR 2011.

Cayer, E., Galanis, N., Desilets, M., Nesreddine, H. & Roy, P. 2009, “Analysis of a carbon dioxide transcritical power cycle using a low temperature source”, *Applied Energy*, vol. 86, no. 7, pp. 1055-1063.

Chen, Y., Halm, N.P., Braun, J.E. & Groll, E.A. 2002, "Mathematical modeling of scroll compressors — part II: overall scroll compressor modeling", *International Journal of Refrigeration*, vol. 25, no. 6, pp. 751-764.

Chen, Y., Lundqvist, P., Johansson, A., Platell, P., Tillämpad termodynamik och kylteknik, KTH, Energiteknik & Skolan för industriell teknik och management (ITM) 2006, "A comparative study of the carbon dioxide transcritical power cycle compared with an organic rankine cycle with R123 as working fluid in waste heat recovery", *Applied Thermal Engineering*, vol. 26, no. 17, pp. 2142-2147.

Chen, Y. 2006, "Novel cycles using carbon dioxide as working fluid (Ph.D. thesis)", Stockholm: Division of Applied Thermodynamics and Refrigeration, Energy Department, KTH University.

Chen, H., Goswami, D.Y. & Stefanakos, E.K. 2010, "A review of thermodynamic cycles and working fluids for the conversion of low-grade heat", *Renewable and Sustainable Energy Reviews*, vol. 14, no. 9, pp. 3059-3067.

Chen, H., Yogi Goswami, D., Rahman, M.M. & Stefanakos, E.K. 2011, "Energetic and exergetic analysis of CO2- and R32-based transcritical Rankine cycles for low-grade heat conversion", *Applied Energy*, vol. 88, no. 8, pp. 2802-2808.

Colonna, P., Casati, E., Trapp, C., Mathijssen, T., Larjola, J., Turunen-Saaresti, T. & Uusitalo, A. 2015, "Organic Rankine Cycle Power Systems: From the Concept to Current Technology, Applications, and an Outlook to the Future", *Journal of Engineering for Gas Turbines and Power*, vol. 137, no. 10, pp. 100801-100801-19.

Dai, Y., Wang, J. & Gao, L. 2009, "Parametric optimization and comparative study of organic Rankine cycle (ORC) for low grade waste heat recovery", *Energy Conversion and Management*, vol. 50, no. 3, pp. 576-582.

Dai, B., Li, M. & Ma, Y. 2014, "Thermodynamic analysis of carbon dioxide blends with low GWP (global warming potential) working fluids-based transcritical Rankine cycles for low-grade heat energy recovery", *ENERGY*, vol. 64, pp. 942-952.

DECC. 2016, "Digest of United Kingdom Energy Statistics (DUKES) 2016". Department for Business, Energy & Industrial Strategy, London.

Gabbrielli, R. 2012, "A novel design approach for small scale low enthalpy binary geothermal power plants", *Energy Conversion and Management*, vol. 64, pp. 263-272.

Gao, P., Jiang, L., Wang, R.Z., Wang, L.W. & Song, F.P. 2015;2014;, "Simulation and experiments on an ORC system with different scroll expanders based on energy and exergy analysis", *Applied Thermal Engineering*, vol. 75, pp. 880-888.

Ge, Y.T., Tassou, S.A., Chaer, I. & Suguartha, N. 2009, "Performance evaluation of a tri-generation system with simulation and experiment", *Applied Energy*, vol. 86, no. 11, pp. 2317-2326.

Ge, Y. & Tassou, S. 2011, "Performance evaluation and optimal design of supermarket refrigeration systems with supermarket model "SuperSim", Part I: Model description and validation", *International journal of refrigeration*, vol.34, pp.527-539.

Ge, Y.T. & Tassou, S.A. 2011, "Thermodynamic analysis of transcritical CO2 booster refrigeration systems in supermarket", *Energy Conversion and Management*, vol. 52, no. 4, pp. 1868-1875.

Ghasemi, H., Paci, M., Tizzanini, A. & Mitsos, A. 2013, "Modeling and optimization of a binary geothermal power plant", *Energy*, vol. 50, no. 1, pp. 412-428.

Hammond, G. & Norman, J. 2014, "Heat recovery opportunities in UK industry", *APPLIED ENERGY*, vol. 116, pp. 387-397.

Hajabdollahi, Z., Hajabdollahi, F., Tehrani, M. & Hajabdollahi, H. 2013, "Thermo-economic environmental optimization of Organic Rankine Cycle for diesel waste heat recovery", *ENERGY*, vol. 63, pp. 142-151.

Heberle, F. & Brüggemann, D. 2010, "Exergy based fluid selection for a geothermal Organic Rankine Cycle for combined heat and power generation", *Applied Thermal Engineering*, vol. 30, no. 11, pp. 1326-1332.

HM Government, 2008, Climate Change Act 2008 (Chapter 27).

Hung, T.C., Shai, T.Y. & Wang, S.K. 1997, "A review of organic rankine cycles (ORCs) for the recovery of low-grade waste heat", *Energy*, vol. 22, no. 7, pp. 661-667.

Jiang, Y., Ma, Y., Li, M. & Fu, L. 2013, "An experimental study of trans-critical CO2 water-water heat pump using compact tube-in-tube heat exchangers", *Energy Conversion and Management*, vol. 76, pp. 92-100.

Kang, S.H. 2012, “Design and experimental study of ORC (organic Rankine cycle) and radial turbine using R245fa working fluid”, *Energy*, vol. 41, no. 1, pp. 514-524.

Karellas, S., Schuster, A. & Leontaritis, A. 2012, "Influence of supercritical ORC parameters on plate heat exchanger design", *Applied Thermal Engineering*, vol. 33-34, no. 1, pp. 70-76.

Kim, Y., Kim, C. & Favrat, D. 2012, “Transcritical or supercritical CO2 cycles using both low- and high-temperature heat sources”, *ENERGY*, vol. 43, no. 1, pp. 402-415.

Klein S.A., 2014. Engineering Equation Solver (EES) for Microsoft Windows Operating Systems, Professional V9.711-3D, F-Chart software, Madison USA, WI, <http://www.fChart.com/ > (accessed 31.01.14).

Landelle, A., Tauveron, N., Revellin, R., Haberschill, P., Colasson, S. & Roussel, V. 2017, "Performance investigation of reciprocating pump running with organic fluid for organic Rankine cycle", *APPLIED THERMAL ENGINEERING*, vol. 113, pp. 962-969.

Laohalertdecha, S. & Wongwises, S. 2010, "The effects of corrugation pitch on the condensation heat transfer coefficient and pressure drop of R-134a inside horizontal corrugated tube", *International Journal of Heat and Mass Transfer*, vol. 53, no. 13, pp. 2924-2931.

Le, V., Kheiri, A., Feidt, M. & Pelloux-Prayer, S. 2014, “Thermodynamic and economic optimizations of a waste heat to power plant driven by a subcritical ORC (Organic Rankine Cycle) using pure or zeotropic working fluid”, *ENERGY*, vol. 78, pp. 622-638.

Lecompte, S., Huisseune, H., van den Broek, M., Vanslambrouck, B. & De Paepe, M. 2015, “Review of organic Rankine cycle (ORC) architectures for waste heat recovery”, *Renewable and Sustainable Energy Reviews*, vol. 47, pp. 448-461.

Lemmon, E., Huber M. & McLinden M., 2007. NIST REFPROP standard reference database 23, Version 8.0, User’s guide, NIST.

Li, Y., Du, M., Wu, C., Wu, S. & Liu, C. 2014, “Potential of organic Rankine cycle using zeotropic mixtures as working fluids for waste heat recovery”, *ENERGY*, vol. 77, pp. 509-519.

Liang, K., Stone, R., Hancock, W., Dadd, M. & Bailey, P. 2014, "Comparison between a crank-drive reciprocating compressor and a novel oil-free linear compressor", *INTERNATIONAL JOURNAL OF REFRIGERATION-REVUE INTERNATIONALE DU FROID,* vol. 45, pp. 25-34.

Liu, B., Chien, K. & Wang, C. 2004, "Effect of working fluids on organic Rankine cycle for waste heat recovery", *Energy,* vol. 29, no. 8, pp. 1207-1217.

Luo, X., Yi, Z., Chen, Z., Chen, Y. & Mo, S. 2016, "Performance comparison of the liquid-vapor separation, parallel flow, and serpentine condensers in the organic Rankine cycle", *APPLIED THERMAL ENGINEERING,* vol. 94, pp. 435-448.

Madhawa Hettiarachchi, H.D., Golubovic, M., Worek, W.M. & Ikegami, Y. 2007, "Optimum design criteria for an Organic Rankine cycle using low-temperature geothermal heat sources", *Energy,* vol. 32, no. 9, pp. 1698-1706.

Mago, P.J., Chamra, L.M., Srinivasan, K. & Somayaji, C. 2008, "An examination of regenerative organic Rankine cycles using dry fluids", *Applied Thermal Engineering,* vol. 28, no. 8, pp. 998-1007.

Manolakos, D., Papadakis, G., Kyritsis, S. & Bouzianas, K. 2007, "Experimental evaluation of an autonomous low-temperature solar Rankine cycle system for reverse osmosis desalination", *Desalination,* vol. 203, no. 1, pp. 366-374.

Meinel, D., Wieland, C. & Spliethoff, H. 2014, "Effect and comparison of different working fluids on a two-stage organic rankine cycle (ORC) concept", *APPLIED THERMAL ENGINEERING,* vol. 63, no. 1, pp. 246-253.

Pan, L., Wang, H. & Shi, W. 2012, "Performance analysis in near-critical conditions of organic Rankine cycle", *Energy,* vol. 37, no. 1, pp. 281-286.

Papadopoulos, A.I., Stijepovic, M. & Linke, P. 2010, "On the systematic design and selection of optimal working fluids for Organic Rankine Cycles", *Applied Thermal Engineering,* vol. 30, no. 6, pp. 760-769.

Pei, G., Li, J., Li, Y., Wang, D. & Ji, J. 2011, "Construction and dynamic test of a small-scale organic rankine cycle", *Energy,* vol. 36, no. 5, pp. 3215-3223.

Pierobon, L., Nguyen, T., Larsen, U., Haglind, F., Elmegaard, B. 2013, "Multi-objective optimization of organic Rankine cycles for waste heat recovery: Application in an offshore platform", *Energy,* vol. 58, pp. 538-549.

Pu, W., Yue, C., Han, D., He, W., Liu, X., Zhang, Q. & Chen, Y. 2016, "Experimental study on Organic Rankine cycle for low grade thermal energy recovery", *APPLIED THERMAL ENGINEERING*, vol. 94, pp. 221-227.

Qiu, G., Shao, Y., Li, J., Liu, H. & Riffat, S.B. 2012, "Experimental investigation of a biomass-fired ORC-based micro-CHP for domestic applications", *Fuel*, vol. 96, no. 1, pp. 374-382.

Qiu, G. 2012, "Selection of working fluids for micro-CHP systems with ORC", *Renewable Energy*, vol. 48, pp. 565-570.

Quoilin, S., Lemort, V. & Lebrun, J. 2010, "Experimental study and modeling of an Organic Rankine Cycle using scroll expander", *Applied Energy*, vol. 87, no. 4, pp. 1260-1268.

Quoilin, S., Declaye, S., Tchanche, B.F. & Lemort, V. 2011, "Thermo-economic optimization of waste heat recovery Organic Rankine Cycles", *Applied Thermal Engineering*, vol. 31, no. 14, pp. 2885-2893.

Quoilin, S., Broek, M.V.D., Declaye, S., Dewallef, P. & Lemort, V. 2013, "Techno-economic survey of organic rankine cycle (ORC) systems", *Renewable and Sustainable Energy Reviews*, vol. 22, pp. 168-186.

Saleh, B., Koglbauer, G., Wendland, M. & Fischer, J. 2007, "Working fluids for low-temperature organic Rankine cycles", *Energy*, vol. 32, no. 7, pp. 1210-1221.

Tchanche, B.F., Papadakis, G., Lambrinos, G. & Frangoudakis, A. 2009, "Fluid selection for a low-temperature solar organic Rankine cycle", *Applied Thermal Engineering*, vol. 29, no. 11, pp. 2468-2476.

Tchanche, B.F., Lambrinos, G., Frangoudakis, A. & Papadakis, G. 2011, "Low-grade heat conversion into power using organic Rankine cycles - A review of various applications", *Renewable and Sustainable Energy Reviews*, vol. 15, no. 8, pp. 3963-3979.

Uris, M., Linares, J. & Arenas, E. 2014, “Techno-economic feasibility assessment of a biomass cogeneration plant based on an Organic Rankine Cycle”, *RENEWABLE ENERGY,* vol. 66, pp. 707-713.

Vélez, F., Chejne, F., Antolin, G. & Quijano, A. 2012, “Theoretical analysis of a transcritical power cycle for power generation from waste energy at low temperature heat source”, *Energy Conversion and Management,* vol. 60, pp. 188-195.

Walraven, D., Laenen, B. & D'haeseleer, W. 2015, "Minimizing the levelized cost of electricity production from low-temperature geothermal heat sources with ORCs: Water or air cooled?", *APPLIED ENERGY,* vol. 142, pp. 144-153.

Wang, J.L., Wang, X.D. & Zhao, L. 2012, “An experimental study on the recuperative low temperature solar Rankine cycle using R245fa”, *Applied Energy,* vol. 94, pp. 34-40.

Wang, J., Yan, Z., Wang, M., Li, M. & Dai, Y. 2013, “Multi-objective optimization of an organic Rankine cycle (ORC) for low grade waste heat recovery using evolutionary algorithm”, *Energy Conversion and Management,* vol. 71, pp. 146-158.

Wang, Z.Q., Zhou, N.J., Guo, J. & Wang, X.Y. 2012, “Fluid selection and parametric optimization of organic Rankine cycle using low temperature waste heat”, *Energy,* vol. 40, no. 1, pp. 107-115.

Wongwises, S. & Polsongkram, M. 2006, "Condensation heat transfer and pressure drop of HFC-134a in a helically coiled concentric tube-in-tube heat exchanger", *International Journal of Heat and Mass Transfer,* vol. 49, no. 23, pp. 4386-4398.

Xia, G., Zhang, Y., Wu, Y., Ma, C., Ji, W., Liu, S. & Guo, H. 2015, "Experimental study on the performance of single-screw expander with different inlet vapor dryness", *Applied Thermal Engineering,* vol. 87, pp. 34-40.

Yamamoto, T., Furuhata, T., Arai, N. & Mori, K. 2001, “Design and testing of the Organic Rankine Cycle”, *Energy,* vol. 26, no. 3, pp. 239-251.

Yang, X., Xu, J., Miao, Z., Zou, J. & Yu, C. 2015, "Operation of an organic Rankine cycle dependent on pumping flow rates and expander torques", *Energy,* vol. 90, pp. 864-878.

Zhang, X.R., Yamaguchi, H., Uneno, D., Fujima, K., Enomoto, M. & Sawada, N. 2006, "Analysis of a novel solar energy-powered Rankine cycle for combined power and heat generation using supercritical carbon dioxide", *Renewable Energy,* vol. 31, no. 12, pp. 1839-1854.

Zhang, X.R., Yamaguchi, H., Fujima, K., Enomoto, M. & Sawada, N. 2007, "Theoretical analysis of a thermodynamic cycle for power and heat production using supercritical carbon dioxide", *Energy*, vol. 32, no. 4, pp. 591-599.

Appendix A: R245fas ORC test rig and T-CO_2 test rig with heat source system

This appendix presents the schematic of the R245fa ORC test rig and T-CO_2 test rig with heat source system. The system employs thermal oil as heat transfer medium to transfer the recovered heat from the CHP unit to both power generation systems as described in Chapter 1.

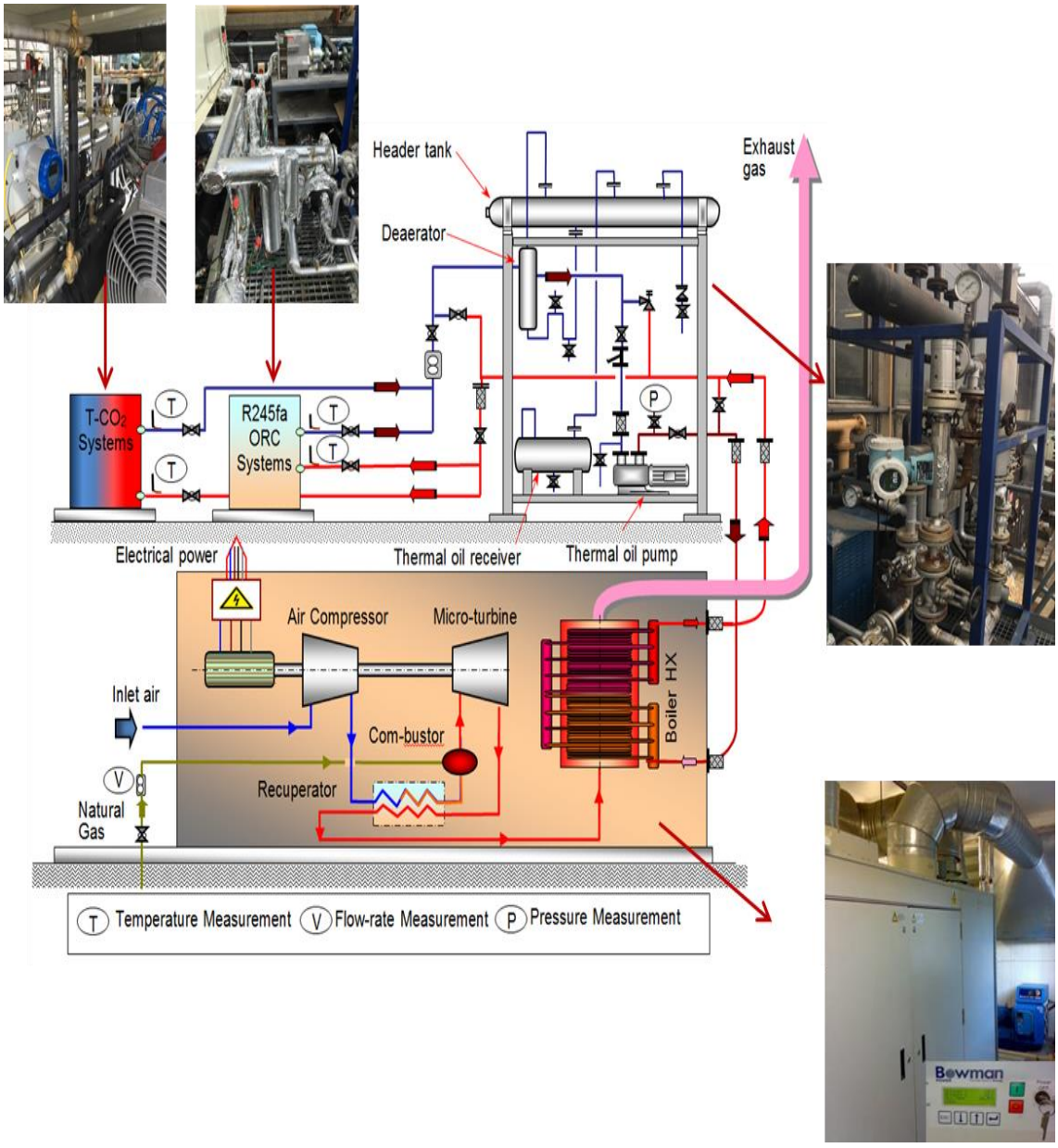

Figure A.1 R245fa ORC test rig and T-CO_2 test rig with heat source system

Appendix B: Heat transfer fluid (Thermal Oil) data

Product name: GLOBALTHERM™ M Heat transfer fluid

Manufacturer: Global Oil Company (Europe) Ltd.

Table B.1 The performance data of the heat transfer fluid (thermal oil)

Temperature		Density	Specific heat	Thermal conductivity	Kinematic Viscosity	Dynamic Viscosity
(T)	(T)	(ρ)	(C_p)	(k)	(ν)	(μ)
℃	°F	kg/m^3	KJ/Kg.K	W/m.K	mm^2/s	Pa.s
0	32	876	1.809	0.136	310	0.27156
20	68	863	1.882	0.134	85	0.07336
40	104	850	1.954	0.133	29.8	0.02533
100	212	811	2.173	0.128	4.5	0.00365
150	302	778	2.355	0.125	2.225	0.00173
200	392	746	2.538	0.121	1.25	0.00093
250	482	713	2.720	0.118	0.84	0.00060
300	572	681	2.902	0.114	0.62	0.00042
340	644	655	3.048	0.111	0.52	0.00034

Best fit equation (temperature in℃)

1. Density (kg/m^3) at temperature range 0-340 ℃:

$$\rho = -0.650356062 * T + 875.9442763 \quad \text{(B.1)}$$

Coefficient of Multiple Determination $R^2 = 1.0000$

2. Specific heat transfer coefficient (KJ/Kg.K) at the temperature range 0-340 ℃:

$$C_P = 0.003644676874 * T + 1.808716931 \quad \text{(B.2)}$$

Coefficient of Multiple Determination $R^2 = 1.0000$

3. Thermal conductivity (W/m.K) at the temperature range 0-340 ℃:

$$k = -7.236069076 * 10^{-5} * T + 0.1357005519 \quad \text{(B.3)}$$

Coefficient of Multiple Determination $R^2 = 0.9990$

4. Kinematic Viscosity (mm^2/s) at the temperature range 20-340 ℃:

$$\nu = 18138.82456 * T^{-1.802195909} \quad \text{(B.4)}$$

Coefficient of Multiple Determination $R^2 = 0.9995$

5. Dynamic Viscosity (Pa.s) at the temperature range 20-340 ℃:

$$\mu = 27.26994617 * T^{-1.935882922} \quad \text{(B.5)}$$

Coefficient of Multiple Determination $R^2 = 0.9994$

Temperature is in ℃.

Appendix C: Instrumentation and data logging system

This appendix provides the positions of the measurement points in the R245fa ORC test rig and T-CO_2 test rig, identification of the measurement points and calibration equations of the measurement devices.

The positions of the measurement points and required instrumentations in R245fa ORC test rig and heat source system are shown in Fig. C.1.

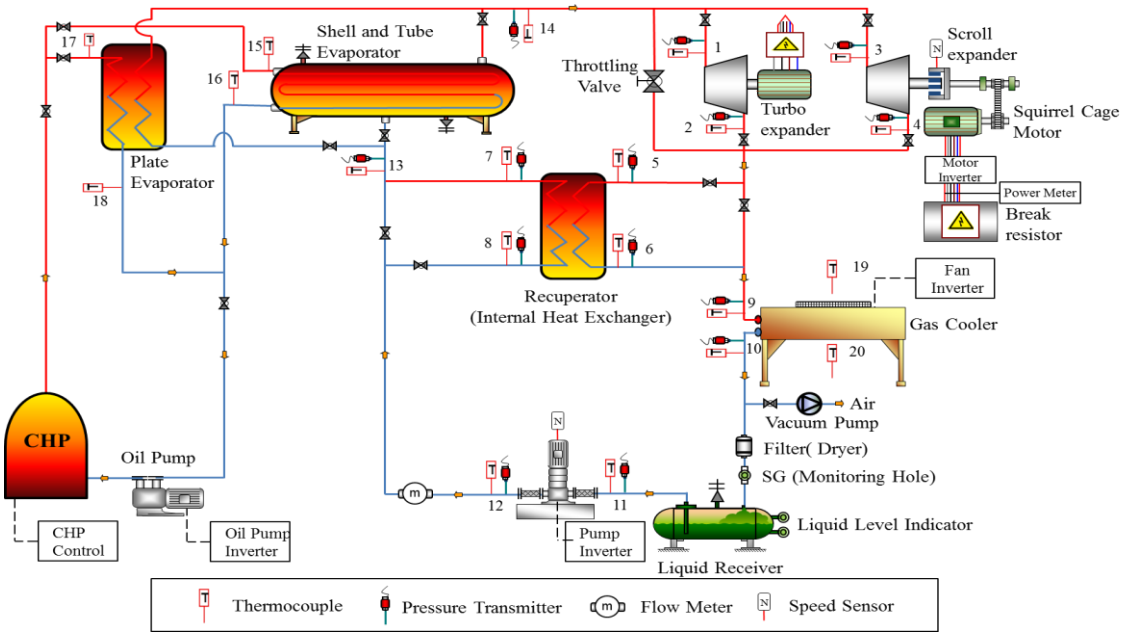

Figure C.1 The positions of the measurement points and instrumentations in R245fa ORC test rig with heat source system

The calibration equations of the thermocouples for R245fa ORC system test rig with heat source system are presented in Table C.1 and the calibration equations of the pressure transducers are shown in Table C.2.

Table C.1 Calibration equations of the thermocouples for R245fa ORC test rig with heat source system

General Equation of thermocouples:

Y=mX + b

Legend:

Y=estimated actual value of temperature ^{o}C
X=measured temperature by thermocouple
SE-m= standard error of m
SE-b= standard error of b
m=slope of Y and X correlation (linear regression)
b= constant or Y intercept
R^2=coefficient of correlation
SE-Y= standard error of estimated Y

Thermocouples	m	b	R^2	SE-m	SE-b	SE-Y
LT1	1.021576	-1.042348	0.999850	0.004731	0.262890	0.355550
LT2	1.020091	-0.807752	0.999940	0.002998	0.166205	0.225627
LT3	1.022177	-0.879117	0.999880	0.003961	0.219410	0.297514
LT4	1.017010	-0.445232	0.999906	0.003720	0.205706	0.280851
LT5	1.011350	-0.054240	0.999960	0.002405	0.132890	0.182568
LT6	1.019654	-0.652477	0.999941	0.002956	0.163550	0.222568
LT7	1.016106	-0.648008	0.999938	0.003034	0.168447	0.229248
LT8	1.020059	-0.862869	0.999910	0.003661	0.203179	0.275577
LT9	1.021321	-0.903763	0.999909	0.003682	0.204200	0.276784
LT10	1.013824	-0.581265	0.999945	0.002839	0.157835	0.215033
LT11	1.017456	0.504539	0.999964	0.002162	0.119584	0.163120
LT12	1.020544	0.366365	0.999984	0.001674	0.092112	0.117651
LT13	1.011880	0.024288	0.999993	0.000976	0.053838	0.074058
LT14	1.017311	-0.410331	0.999971	0.002087	0.115293	0.157502
LT15	0.988386	-0.223060	0.999868	0.004288	0.243086	0.332831
LT16	0.996873	-0.621229	0.999953	0.002577	0.145767	0.198334
LT17	0.995452	-0.422415	0.999798	0.005343	0.301669	0.411727
LT18	1.001248	-0.444646	0.999853	0.004584	0.257410	0.351204
LT19	0.996021	-0.410104	0.999919	0.003395	0.191554	0.261502
LT20	0.990048	-0.118789	0.999816	0.005072	0.286545	0.392978

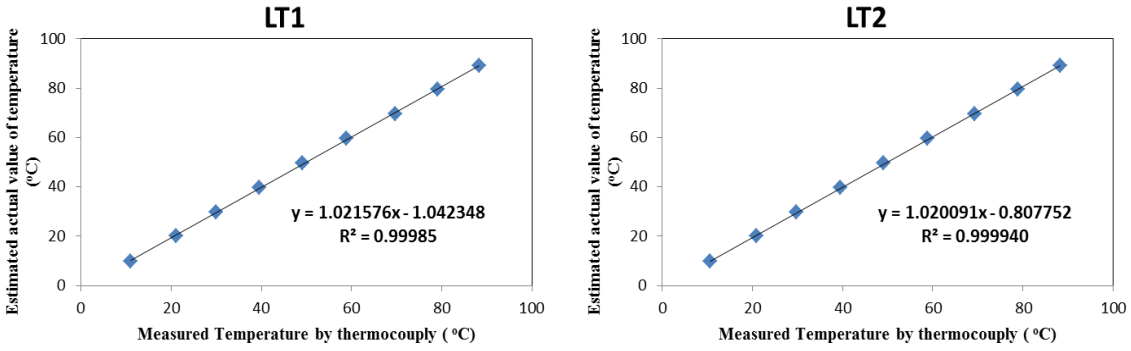

Figure C.2 Example calibration graph and equation of the thermocouples

Table C.2 Calibration equations of the pressure transducers for R245fa ORC test rig with heat source system

General Equation of pressure transducers

Y=mX + b

Legend:

Y=the measured pressure (bar)	m=slope of Y and X correlation (linear regression)
X=the output voltage (V)	b= constant or Y intercept
R^2=coefficient of correlation	SE-m= standard error of m
SE-b= standard error of b	SE-Y= standard error of estimated Y

Pressure Transmitter	a	b	R2	SE-a	SE-b	SE-Y
LP1	2.507785	-0.973348	0.999984	0.004121	0.025050	0.036710
LP2	2.509421	-0.980439	0.999973	2.509421	-0.980439	0.047412
LP3	2.505634	-0.983928	0.999969	0.005650	0.034395	0.050375
LP4	2.512083	-0.973243	0.999915	0.009461	0.057415	0.084139
LP5	2.509853	-1.031003	0.999972	0.005419	0.033020	0.048234
LP6	1.583055	-7.286529	0.999983	0.002680	0.035391	0.037827
LP7	1.601916	-7.488466	0.999849	0.008048	0.105956	0.112240
LP8	1.584127	-7.342400	0.999960	0.004115	0.054435	0.058038
LP9	1.567518	-7.233453	0.999947	0.004663	0.062037	0.066463
LP10	1.558595	-7.132858	0.999796	0.009080	0.120948	0.130149
LP11	1.582257	-7.372106	0.999905	0.006297	0.083501	0.088910
LP12	1.576031	-7.281733	0.999925	0.005589	0.074110	0.079227
LP13	1.574013	-7.304275	0.999935	0.005183	0.068877	0.073559
LP14	1.563420	-7.204503	0.999892	0.006626	0.088265	0.094682

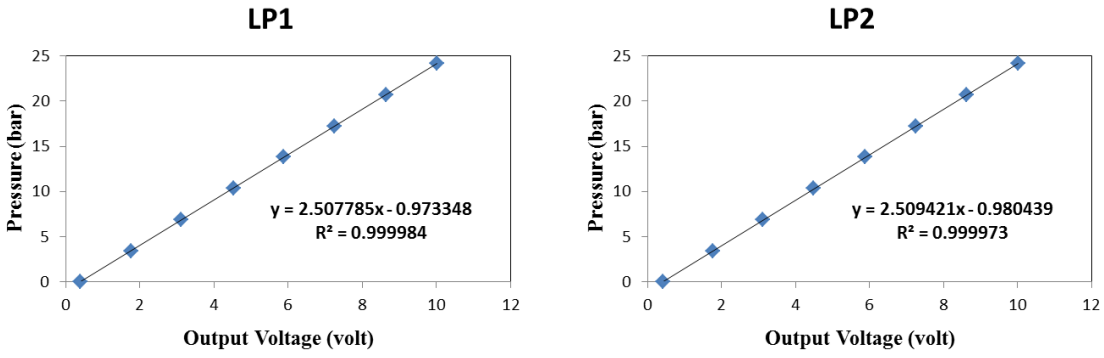

Figure C.3 Example calibration graph and equation of the pressure transducers

The drawing of the air-cooled condenser with different test points and dimensions is shown in Fig. C.4. Twelve test points were taken for each main fan speed from 0% to 100% at 20% intervals in a single quadrant of the condenser. The other quadrants were assumed same as the test quadrant.

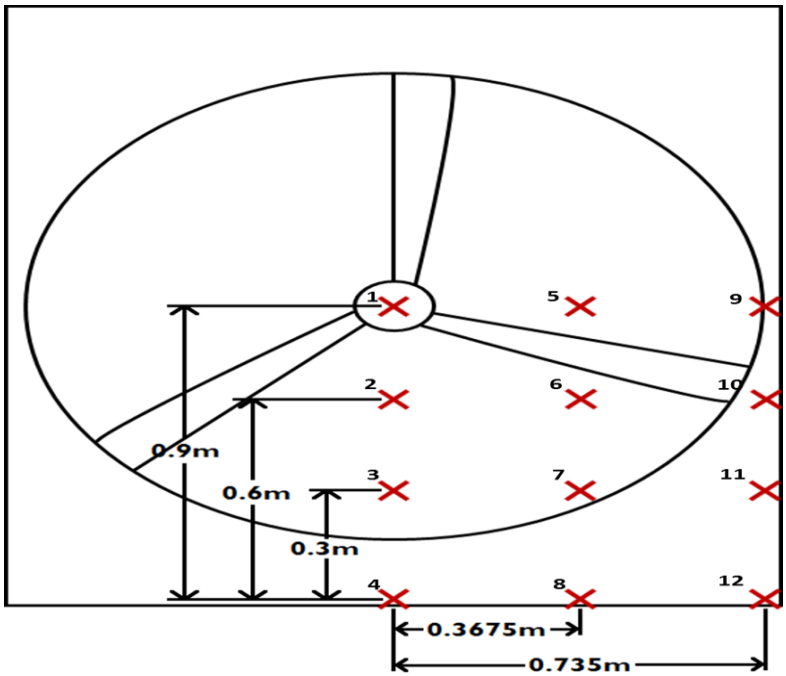

Figure C.4 The drawing of air-cooled condenser with different test points and dimensions

The main fan speed (percentage) with detail measured and averaged air velocities are presented in Table C.3 and the graph and equation is provided in Fig. C.5.

Table C.3 The main fan speed with detailed measured and averaged air velocities

Main Fan Speed (%)	Detail measured air velocity (m/s)					Averaged air Velocity (m/s)
100%	5.12	4.97	3.81	4.97	5.12	3.671
	5.84	3.38	2.57	3.38	5.84	
	2.54	2.41	2.21	2.41	2.54	
	3.57	2.56	2.02	2.56	3.57	
	2.54	2.41	2.21	2.41	2.54	
	5.84	3.38	2.57	3.38	5.84	
	5.12	4.97	3.81	4.97	5.12	
80%	4.81	4.56	4.17	4.56	4.81	3.166
	3.49	2.85	2.48	2.85	3.49	
	2.61	2.26	2.01	2.26	2.61	
	2.38	2.25	1.93	2.25	2.38	
	2.61	2.26	2.01	2.26	2.61	
	3.49	2.85	2.48	2.85	3.49	
	4.81	4.56	4.17	4.56	4.81	
60%	3.53	3.22	3.02	3.22	3.53	2.546
	3.43	2.21	2.11	2.21	3.43	
	2.46	1.66	1.62	1.66	2.46	
	2.39	1.6	1.59	1.6	2.39	
	2.46	1.66	1.62	1.66	2.46	
	3.43	2.21	2.11	2.21	3.43	
	3.53	3.22	3.02	3.22	3.53	
40%	2.24	1.98	1.93	1.98	2.24	1.580
	1.96	1.31	1.66	1.31	1.96	
	1.46	1.19	1.1	1.19	1.46	
	1.2	1.08	0.79	1.08	1.2	
	1.46	1.19	1.1	1.19	1.46	
	1.96	1.31	1.66	1.31	1.96	
	2.24	1.98	1.93	1.98	2.24	
20%	1.05	0.86	0.77	0.86	1.05	0.669
	0.94	0.52	0.32	0.52	0.94	
	0.53	0.58	0.5	0.58	0.53	
	0.7	0.28	0.36	0.28	0.7	
	0.53	0.58	0.5	0.58	0.53	
	0.94	0.52	0.32	0.52	0.94	
	1.05	0.86	0.77	0.86	1.05	

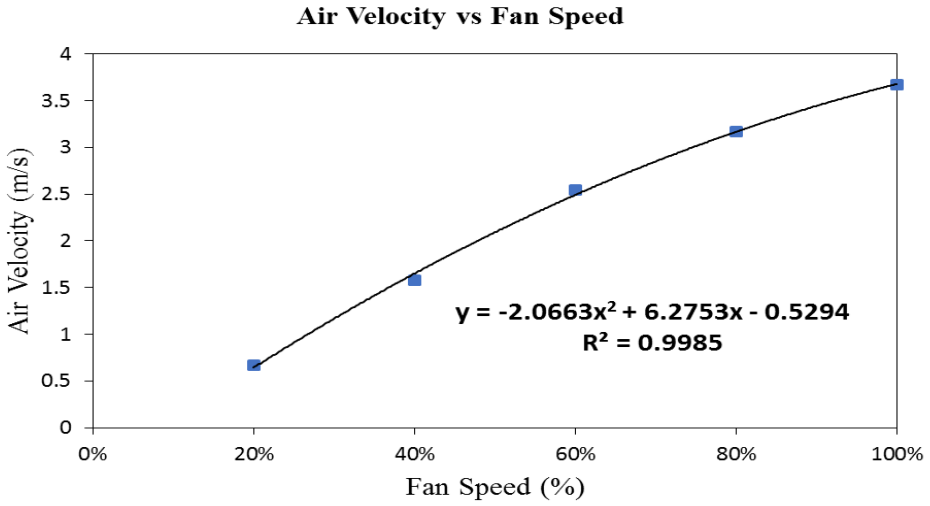

Figure C.5 The graph and equation of air velocity vs. fan speed

The positions of the measurement points and required instrumentations in T-CO_2 test rig and heat source system are shown in Fig. C.1.

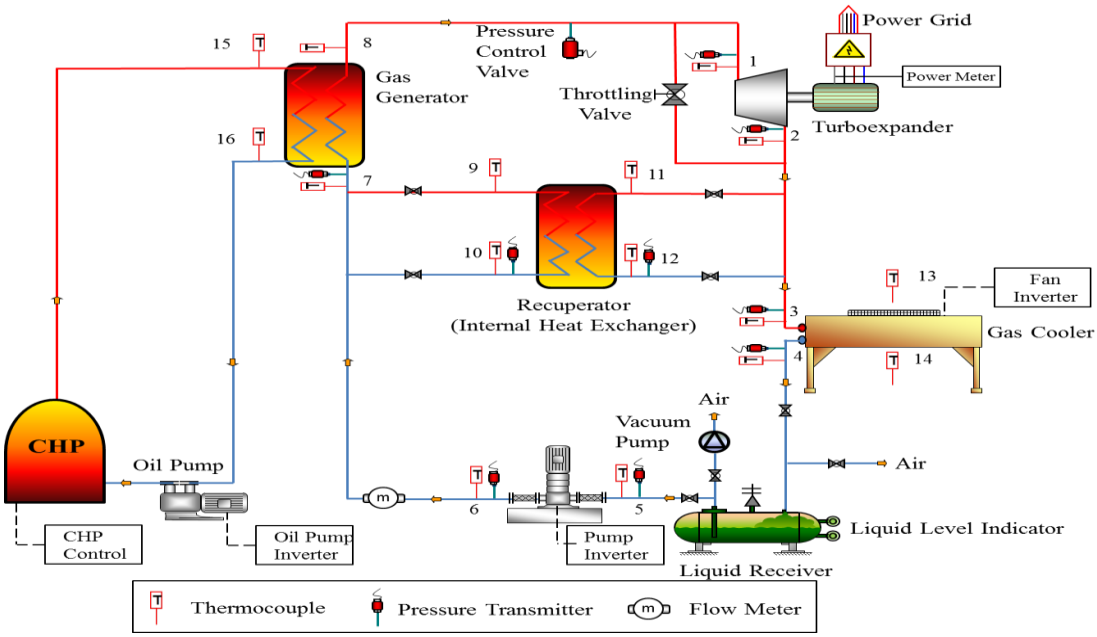

Figure C.6 The positions of the measurement points and instrumentations in T-CO_2 test rig and heat source system

The calibration equations of the thermocouples for T-CO_2 test rig with heat source system are presented in Table C.4 and the calibration equations of the high pressure transducers are shown in Table C.5.

Table C.4 Calibration equations of the thermocouples for T-CO_2 test rig with heat source system

General Equation of thermocouples:

Y=mX + b

Legend:

Y=estimated actual value of temperature ^oC
X=measured temperature by thermocouple
SE-m= standard error of m
SE-b= standard error of b
m=slope of Y and X correlation (linear regression)
b= constant or Y intercept
R^2=coefficient of correlation
SE-Y= standard error of estimated Y

Thermocouples	m	b	R^2	SE-m	SE-b	SE-Y
HT1	0.996865	-0.556615	0.999858	0.004495	0.253985	0.345919
HT2	1.004351	-0.934630	0.999874	0.004262	0.240438	0.325522
HT3	1.000738	-0.696019	0.999881	0.004133	0.233141	0.316834
HT4	0.996104	-0.647796	0.999955	0.002530	0.143272	0.194858
HT5	0.991585	-0.278408	0.999940	0.002906	0.164371	0.224864
HT6	1.000998	-0.851423	0.999951	0.002637	0.149058	0.202076
HT7	1.007247	-0.866662	0.999972	0.002026	0.113858	0.154320
HT8	1.001758	-0.552519	0.999910	0.003599	0.202377	0.275653
HT9	1.000866	-0.796976	0.999932	0.003129	0.176748	0.239819
HT10	0.998033	-0.551098	0.999859	0.004484	0.253040	0.344661
HT11	0.989763	-0.404704	0.999934	0.003036	0.172381	0.235349
HT12	1.002693	-0.879013	0.999905	0.003692	0.208492	0.282522
HT13	1.000206	-0.765943	0.999892	0.003938	0.222495	0.302034
HT14	0.997310	-0.730812	0.999793	0.005426	0.307324	0.417403
HT15	1.000626	-0.720374	0.999787	0.005521	0.311579	0.423251
HT16	0.993594	-0.452647	0.999852	0.004568	0.258539	0.352700

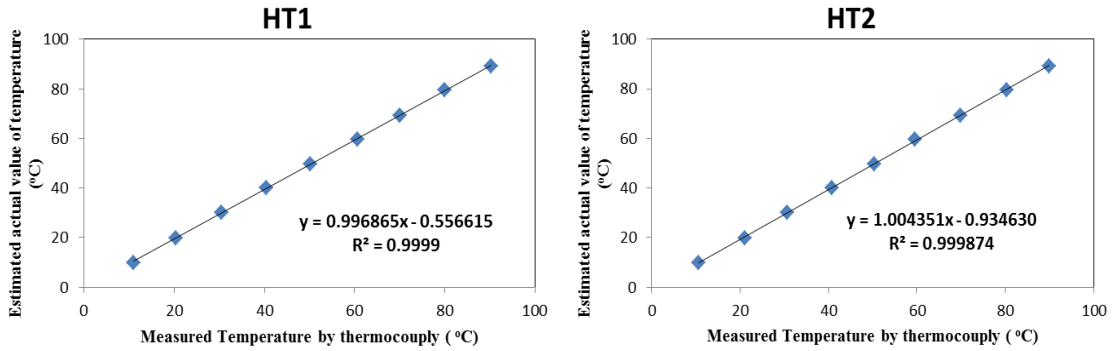

Figure C.7 Example calibration graph and equation of the thermocouples

Table C.5 Calibration equations of the pressure transducers for T-CO_2 test rig with heat source system

General Equation of pressure transducers

Y=mX + b

Legend:

Y=the measured pressure (bar)	m=slope of Y and X correlation (linear regression)
X=the output current (mA)	b= constant or Y intercept
R^2=coefficient of correlation	SE-m= standard error of m
SE-b= standard error of b	SE-Y= standard error of estimated Y

Pressure Transmitter	a	b	R2	SE-a	SE-b	SE-Y
HP1	10.025734	-39.671471	0.999988	0.010768	0.134187	0.177105
HP2	10.032704	-40.194884	0.999997	0.005700	0.071254	0.093682
HP3	10.015839	-39.799510	0.999992	0.008982	0.112142	0.147869
HP4	10.024440	-39.831982	0.999986	0.011678	0.145715	0.192092
HP5	10.012010	-39.663517	0.999990	0.009808	0.122382	0.161534
HP6	10.027082	-40.196709	0.999996	0.006521	0.081564	0.107234
HP7	10.032719	-39.827189	0.999998	0.004193	0.052279	0.068921
HP8	10.056510	-39.808169	0.999998	0.004328	0.053819	0.070961
HP9	10.070373	-40.286489	0.999998	0.004751	0.059209	0.077792

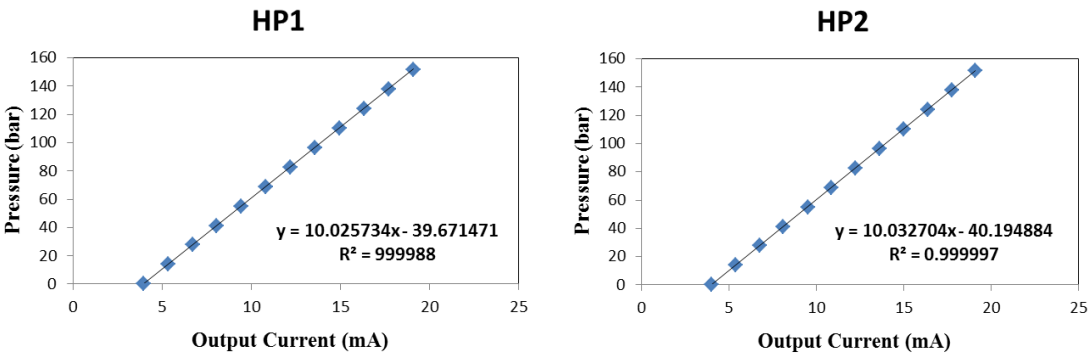

Figure C.8 Example calibration graph and equation of the pressure transducers

Appendix D: Uncertainty analysis

In the analysis of test results, key parameters such as: evaporator heat capacity, condenser heat capacity, turbine efficiencies and system efficiencies etc. are not directly measured. They are calculated as the functions of one or more variables which are directly measured. Each measured variable (from instrumentation) has a random variability which is called as "uncertainty" for each device. The calculations of uncertainty from measured variables into the calculated parameters for both R245fa ORC system and T-CO_2 system are described in this appendix.

The calculated parameters in T-CO_2 system include:

The uncertainty propagation was determined using the EES software. In general, the following equation has been used in software to calculate the uncertainty of calculated parameters:

$$U_Y = \sqrt{\Sigma(\frac{\partial Y}{\partial X_i})^2 U_{X_i}^2} \quad \text{(D.1)}$$

Where:

Y= calculated parameter; X_i =measured variables; U_Y =uncertainty of calculated parameter; U_{X_i}=uncertainty of measured variables

The calculated parameters in R245fa ORC system include: evaporator heat capacity, condenser heat capacity, turbine isentropic efficiency, turbine overall efficiency, system thermal efficiency, system overall efficiency and temperature transfer efficiency of the evaporator.

D.1 Uncertainty of the calculation of the heat capacity of condenser and evaporator in R245fa ORC system

The condenser heat capacity and evaporator heat capacity are functions of:

$$Q_{cond} = f(m, T_3, T_4, P_3, P_4) \quad \text{(D.2)}$$

$$Q_{evap} = f(m, T_7, T_8, P_7, P_8) \quad \text{(D.3)}$$

Where: m=R245fa mass flow rate (kg/s); T_3 =condenser inlet temperature (°C); T_4=condenser outlet temperature (°C); P_3 =condenser inlet pressure (bar); P_4=condenser outlet pressure; T_7=evaporator inlet temperature (°C); T_8=evaporator outlet temperature (°C); P_7 =evaporator inlet pressure (bar); P_8 =evaporator outlet pressure (bar);

Results of the uncertainty analysis for the condenser heat capacity and evaporator heat capacity obtained from EES:

Unit Settings: SI C bar kJ mass deg

Variable±Uncertainty	Partial derivative	% of uncertainty
Q_{cond} = 66.2±0.2299 [kW]		
m = 0.249±0.0003735 [kg/s]	$\partial Q_{cond}/\partial m$ = 265.8	18.66 %
P_3 = 3.13±0.00939 [bar]	$\partial Q_{cond}/\partial P_3$ = -0.4048	0.03 %
P_4 = 2.14±0.00642 [bar]	$\partial Q_{cond}/\partial P_4$ = -0.007925	0.00 %
P_7 = 10.92±0.03276 [bar]	$\partial Q_{cond}/\partial P_7$ = 0	0.00 %
P_8 = 10.68±0.03204 [bar]	$\partial Q_{cond}/\partial P_8$ = 0	0.00 %
T_3 = 94.88±0.5 [C]	$\partial Q_{cond}/\partial T_3$ = 0.2573	31.33 %
T_4 = 17.09±0.5 [C]	$\partial Q_{cond}/\partial T_4$ = -0.325	49.98 %
T_7 = 17.19±0.5 [C]	$\partial Q_{cond}/\partial T_7$ = 0	0.00 %
T_8 = 113.9±0.5 [C]	$\partial Q_{cond}/\partial T_8$ = 0	0.00 %
Q_{evap} = 68.12±0.243 [kW]		
m = 0.249±0.0003735 [kg/s]	$\partial Q_{evap}/\partial m$ = 273.6	17.68 %
P_3 = 3.13±0.00939 [bar]	$\partial Q_{evap}/\partial P_3$ = 0	0.00 %
P_4 = 2.14±0.00642 [bar]	$\partial Q_{evap}/\partial P_4$ = 0	0.00 %
P_7 = 10.92±0.03276 [bar]	$\partial Q_{evap}/\partial P_7$ = -0.008037	0.00 %
P_8 = 10.68±0.03204 [bar]	$\partial Q_{evap}/\partial P_8$ = -0.4527	0.36 %
T_3 = 94.88±0.5 [C]	$\partial Q_{evap}/\partial T_3$ = 0	0.00 %
T_4 = 17.09±0.5 [C]	$\partial Q_{evap}/\partial T_4$ = 0	0.00 %
T_7 = 17.19±0.5 [C]	$\partial Q_{evap}/\partial T_7$ = -0.3244	44.56 %
T_8 = 113.9±0.5 [C]	$\partial Q_{evap}/\partial T_8$ = 0.2972	37.40 %

Uncertainty of the condenser heat capacity was determined to be

- Absolute uncertainty:±0.2299
- Relative uncertainty:±0.35%

Uncertainty of the evaporator heat capacity was determined to be

- Absolute uncertainty:±0.243
- Relative uncertainty:±0.36%

D.2 Uncertainty of the calculation of the isentropic and overall efficiencies of turboexpander in R245fa ORC system

The turboexpander isentropic and overall efficiencies are functions of:

$$\eta_{T,is} = f(T_1, T_2, P_1, P_2) \tag{D.4}$$

$$\eta_{T,all} = f(W_T, m, T_1, T_2, P_1, P_2) \tag{D.5}$$

Refers to equations (4.1) and (4.3) in Chapter 4.

Results of the uncertainty analysis for the turbine isentropic and overall efficiencies obtained from EES:

Unit Settings: SI C bar kJ mass deg

Variable±Uncertainty	Partial derivative	% of uncertainty
$\eta_{turbine,isentropic}$ = 34.45±4.047		
m = 0.249±0.0003735 [kg/s]	$\partial\eta_{turbine,isentropic}/\partial m$ = 0	0.00 %
P_1 = 10.14±0.03042 [bar]	$\partial\eta_{turbine,isentropic}/\partial P_1$ = -12.38	0.87 %
P_2 = 3.933±0.0118 [bar]	$\partial\eta_{turbine,isentropic}/\partial P_2$ = 17.78	0.27 %
T_1 = 112.4±0.5 [C]	$\partial\eta_{turbine,isentropic}/\partial T_1$ = 5.951	54.04 %
T_2 = 96.84±0.5 [C]	$\partial\eta_{turbine,isentropic}/\partial T_2$ = -5.42	44.83 %
$W_{turbine}$ = 0.7443±0.005954 [kW]	$\partial\eta_{turbine,isentropic}/\partial W_{turbine}$ = 0	0.00 %
$\eta_{turbine,overall}$ = 15.43±0.1451 [%]		
m = 0.249±0.0003735 [kg/s]	$\partial\eta_{turbine,overall}/\partial m$ = -61.98	2.55 %
P_1 = 10.14±0.03042 [bar]	$\partial\eta_{turbine,overall}/\partial P_1$ = -1.366	8.20 %
P_2 = 3.933±0.0118 [bar]	$\partial\eta_{turbine,overall}/\partial P_2$ = 4.155	11.42 %
T_1 = 112.4±0.5 [C]	$\partial\eta_{turbine,overall}/\partial T_1$ = -0.06768	5.44 %
T_2 = 96.84±0.5 [C]	$\partial\eta_{turbine,overall}/\partial T_2$ = 0	0.00 %
$W_{turbine}$ = 0.7443±0.005954 [kW]	$\partial\eta_{turbine,overall}/\partial W_{turbine}$ = 20.73	72.39 %

Uncertainty of turbine isentropic efficiency was determined to be

- Absolute uncertainty: ±4.047
- Relative uncertainty:±11.74%

Uncertainty of turbine overall efficiency was determined to be

- Absolute uncertainty: ±0.1451
- Relative uncertainty:±0.94%

D.3 Uncertainty of the calculation of the thermal and overall efficiencies of the R245fa ORC system

The R245fa ORC system thermal and overall efficiencies are functions of:

$$\eta_{s,th} = f(T_1, T_2, T_5, T_6, T_7, T_8, P_1, P_2, P_5 P_6, P_7, P_8) \quad \text{(D.6)}$$

$$\eta_{T,all} = f(W_T, m, T_5, T_6, T_7, T_8, P_5, P_6, P_7, P_8) \quad \text{(D.7)}$$

Refer to equations (4.5) and (4.6) in Chapter 4.

Results of the uncertainty analysis for the system thermal and overall efficiencies obtained from EES:

Unit Settings: SI C bar kJ mass deg

Variable±Uncertainty	Partial derivative	% of uncertainty
$\eta_{system,net}$ = 0.8416±0.009196		
m = 0.249±0.0003735 [kg/s]	$\partial\eta_{system,net}/\partial m$ = -4.388	3.18 %
P_1 = 10.14±0.03042 [bar]	$\partial\eta_{system,net}/\partial P_1$ = 0	0.00 %
P_2 = 3.933±0.0118 [bar]	$\partial\eta_{system,net}/\partial P_2$ = 0	0.00 %
P_5 = 1.78±0.00534 [bar]	$\partial\eta_{system,net}/\partial P_5$ = 0.02695	0.02 %
P_6 = 11.11±0.03333 [bar]	$\partial\eta_{system,net}/\partial P_6$ = -0.0269	0.95 %
P_7 = 10.92±0.03276 [bar]	$\partial\eta_{system,net}/\partial P_7$ = 0.0000993	0.00 %
P_8 = 10.68±0.03204 [bar]	$\partial\eta_{system,net}/\partial P_8$ = 0.005594	0.04 %
T_1 = 112.4±0.5 [C]	$\partial\eta_{system,net}/\partial T_1$ = 0	0.00 %
T_2 = 96.84±0.5 [C]	$\partial\eta_{system,net}/\partial T_2$ = 0	0.00 %
T_5 = 17.51±0.5 [C]	$\partial\eta_{system,net}/\partial T_5$ = -0.0004917	0.07 %
T_6 = 17.19±0.5 [C]	$\partial\eta_{system,net}/\partial T_6$ = 0	0.00 %
T_7 = 17.19±0.5 [C]	$\partial\eta_{system,net}/\partial T_7$ = 0.004008	4.75 %
T_8 = 113.9±0.2 [C]	$\partial\eta_{system,net}/\partial T_8$ = -0.003672	0.64 %
$W_{turbine}$ = 0.7443±0.005954 [kW]	$\partial\eta_{system,net}/\partial W_{turbine}$ = 1.468	90.35 %
$\eta_{system,the}$ = 2.483±0.4446		
m = 0.249±0.0003735 [kg/s]	$\partial\eta_{system,the}/\partial m$ = 0	0.00 %
P_1 = 10.14±0.03042 [bar]	$\partial\eta_{system,the}/\partial P_1$ = -0.6603	0.20 %
P_2 = 3.933±0.0118 [bar]	$\partial\eta_{system,the}/\partial P_2$ = 0.6019	0.03 %
P_5 = 1.78±0.00534 [bar]	$\partial\eta_{system,the}/\partial P_5$ = 0.01158	0.00 %
P_6 = 11.11±0.03333 [bar]	$\partial\eta_{system,the}/\partial P_6$ = -0.0118	0.00 %
P_7 = 10.92±0.03276 [bar]	$\partial\eta_{system,the}/\partial P_7$ = 0.0002929	0.00 %
P_8 = 10.68±0.03204 [bar]	$\partial\eta_{system,the}/\partial P_8$ = 0.0165	0.00 %
T_1 = 112.4±0.5 [C]	$\partial\eta_{system,the}/\partial T_1$ = 0.432	23.61 %
T_2 = 96.84±0.5 [C]	$\partial\eta_{system,the}/\partial T_2$ = -0.3837	18.62 %
T_5 = 17.51±0.5 [C]	$\partial\eta_{system,the}/\partial T_5$ = 0.4775	28.83 %
T_6 = 17.19±0.5 [C]	$\partial\eta_{system,the}/\partial T_6$ = -0.4762	28.69 %
T_7 = 17.19±0.5 [C]	$\partial\eta_{system,the}/\partial T_7$ = 0.01182	0.02 %
T_8 = 113.9±0.2 [C]	$\partial\eta_{system,the}/\partial T_8$ = -0.01083	0.00 %
$W_{turbine}$ = 0.7443±0.005954 [kW]	$\partial\eta_{system,the}/\partial W_{turbine}$ = 0	0.00 %

Uncertainty of system thermal efficiency was determined to be

- Absolute uncertainty: ±0.009196
- Relative uncertainty:±1.09%

Uncertainty of system overall efficiency was determined to be

- Absolute uncertainty: ±0.4446
- Relative uncertainty:±17.91%

D.4 Uncertainty of the calculation of the temperature transfer efficiency of the evaporator in R245fa ORC system

The temperature transfer efficiency of the evaporator is function of:

$$\mu_{evp} = f(T_7, T_8, T_{17}) \quad \text{(D.8)}$$

Refers to equation (5.8) in Chapter 5.

Results of the uncertainty analysis for the temperature transfer efficiency of the evaporator obtained from EES:

Unit Settings: SI C bar kJ mass deg

Variable±Uncertainty	Partial derivative	% of uncertainty
η_{evp} = 0.822±0.007512		
T_{17} = 174.1±0.5	$\partial\eta_{evp}/\partial T_{17}$ = -0.009452	39.58 %
T_7 = 87.12±0.5	$\partial\eta_{evp}/\partial T_7$ = -0.002047	1.86 %
T_8 = 158.6±0.5	$\partial\eta_{evp}/\partial T_8$ = 0.0115	58.57 %

Uncertainty of the temperature transfer efficiency of the evaporator was determined to be

- Absolute uncertainty: ±0.007512
- Relative uncertainty:±0.91%

The calculated parameters in T-CO_2 system include: turbine power generation, gas generator heat capacity, turbine isentropic efficiency and turbine overall efficiency.

D.5 Uncertainty of the calculation of the turbine power generation in T-CO_2 system

The turbine power generation is function of

$$W'_{T,CO_2} = f(\dot{m}_{f,CO_2}, T_1, T_2, P_1, P_2) \quad \text{(D.9)}$$

Refers to equation (7.1) in Chapter 7.

Results of the uncertainty analysis for the CO_2 turbine power generation obtained from EES:

Unit Settings: SI C bar kJ mass deg

Variable±Uncertainty	Partial derivative	% of uncertainty
$W_{T,CO2}$ = 1.625±0.2437		
m = 0.255±0.000255 [kg/s]	$\partial W_{T,CO2}/\partial m$ = 6.373	0.00 %
P_1 = 90.83±0.2725	$\partial W_{T,CO2}/\partial P_1$ = -0.1768	3.91 %
P_2 = 66.81±0.2004	$\partial W_{T,CO2}/\partial P_2$ = 0.1975	2.64 %
T_1 = 111.9±0.5	$\partial W_{T,CO2}/\partial T_1$ = 0.3443	49.91 %
T_2 = 93.58±0.5	$\partial W_{T,CO2}/\partial T_2$ = -0.3216	43.54 %

Uncertainty of CO_2 turbine power generation was determined to be

- Absolute uncertainty: ±0.2437
- Relative uncertainty:±15%

D.6 Uncertainty of the calculation of the gas generator heat capacity in T-CO_2 system

The gas generator heat capacity is function of

$$Q_{gg} = f(\dot{m}_{f,CO_2}, T_7, T_8, P_7, P_8) \quad \text{(D.10)}$$

Refers to equation (7.2) in Chapter 7.

Results of the uncertainty analysis for the CO_2 gas generator heat capacity obtained from EES:

Unit Settings: SI C bar kJ mass deg

Variable±Uncertainty	Partial derivative	% of uncertainty
Q_{evap} = 60.15±0.6493 [kW]		
m = 0.255±0.000255 [kg/s]	$\partial Q_{evap}/\partial m$ = 235.9	0.86 %
P_7 = 91.23±0.2737 [bar]	$\partial Q_{evap}/\partial P_7$ = 0.2569	1.17 %
P_8 = 90.83±0.2725 [bar]	$\partial Q_{evap}/\partial P_8$ = -0.1763	0.55 %
T_7 = 34.03±0.5 [C]	$\partial Q_{evap}/\partial T_7$ = -1.235	90.41 %
T_8 = 112.2±0.5 [C]	$\partial Q_{evap}/\partial T_8$ = 0.344	7.02 %

Uncertainty of CO_2 gas generator heat capacity was determined to be

- Absolute uncertainty: ±0.6493
- Relative uncertainty: ±1.08%

D.7 Uncertainty of the calculation of the isentropic and overall efficiencies of CO_2 turbine in T-CO_2 system

The CO_2 turbine isentropic and overall efficiencies are functions of:

$$\eta_{T,co_2,is} = f(T_1, T_2, P_1, P_2) \quad \text{(D.11)}$$

$$\eta_{T,co_2,all} = f(W_T, \dot{m}_{f,CO_2}, T_1, T_2, P_1, P_2) \quad \text{(D.12)}$$

Refer to equations (7.3) and (7.4) in Chapter 7.

Results of the uncertainty analysis for the isentropic and overall efficiencies of CO_2 turbine obtained from EES:

Unit Settings: SI C bar kJ mass deg

Variable±Uncertainty	Partial derivative	% of uncertainty
$\eta_{turbine,isentropic}$ = 36.7±5.577		
m = 0.255±0.000255 [kg/s]	$\partial\eta_{turbine,isentropic}/\partial m$ = 0	0.00 %
P_1 = 90.83±0.2725 [bar]	$\partial\eta_{turbine,isentropic}/\partial P_1$ = -5.161	6.36 %
P_2 = 66.81±0.2004 [bar]	$\partial\eta_{turbine,isentropic}/\partial P_2$ = 6.189	4.95 %
T_1 = 111.9±0.5 [C]	$\partial\eta_{turbine,isentropic}/\partial T_1$ = 7.582	46.22 %
T_2 = 93.58±0.5 [C]	$\partial\eta_{turbine,isentropic}/\partial T_2$ = -7.269	42.47 %
$W_{turbine}$ = 0.4943±0.003955 [kW]	$\partial\eta_{turbine,isentropic}/\partial W_{turbine}$ = 0	0.00 %
$\eta_{turbine,overall}$ = 11.17±0.1717 [%]		
m = 0.255±0.000255 [kg/s]	$\partial\eta_{turbine,overall}/\partial m$ = -43.81	0.42 %
P_1 = 90.83±0.2725 [bar]	$\partial\eta_{turbine,overall}/\partial P_1$ = -0.3549	31.73 %
P_2 = 66.81±0.2004 [bar]	$\partial\eta_{turbine,overall}/\partial P_2$ = 0.5254	37.62 %
T_1 = 111.9±0.5 [C]	$\partial\eta_{turbine,overall}/\partial T_1$ = -0.06079	3.13 %
T_2 = 93.58±0.5 [C]	$\partial\eta_{turbine,overall}/\partial T_2$ = 0	0.00 %
$W_{turbine}$ = 0.4943±0.003955 [kW]	$\partial\eta_{turbine,overall}/\partial W_{turbine}$ = 22.6	27.09 %

Uncertainty of CO_2 turbine isentropic efficiency was determined to be

- Absolute uncertainty: ±5.577
- Relative uncertainty: ±15.2%

Uncertainty of CO_2 turbine overall efficiency was determined to be

- Absolute uncertainty:±0.1717
- Relative uncertainty:±1.54%